Experimental and numerical analysis of delamination of layered glued plate structures with variable width

Hlača, Ivan

UNIVERSITY OF RIJEKA

FACULTY OF CIVIL ENGINEERING

Ivan Hlača

EXPERIMENTAL AND NUMERICAL ANALYSIS OF DELAMINATION OF LAYERED GLUED PLATE STRUCTURES WITH VARIABLE WIDTH

DOCTORAL THESIS

Rijeka, 2023

UNIVERSITY OF RIJEKA

FACULTY OF CIVIL ENGINEERING

Ivan Hlača

EXPERIMENTAL AND NUMERICAL ANALYSIS OF DELAMINATION OF LAYERED GLUED PLATE STRUCTURES WITH VARIABLE WIDTH

DOCTORAL THESIS

Supervisor: Assoc. Prof. Dragan Ribarić, PhD

Co-supervisor: Assoc. Prof. Leo Škec, PhD

Rijeka, 2023

Mentor rada: Izv. prof. dr. sc. Dragan Ribarić

Komentor rada: Izv. prof. dr. sc. Leo Škec

Doktorski rad obranjen je dana _____ na Građevinskom fakultetu Sveučilišta u Rijeci, pred povjerenstvom u sastavu:

1. Prof. dr. sc. Gordan Jelenić, Sveučilište u Rijeci, Građevinski fakultet, predsjednik
2. Prof. dr. sc. Domagoj Lanc, Sveučilište u Rijeci, Tehnički fakultet, vanjski član
3. doc. dr. sc. Mijo Nikolić, Sveučilište u Splitu, Fakultet građevinarstva, arhitekture i geodezije, vanjski član

Acknowledgements

The findings presented in this thesis is the result of work within the research project IP-06-2016-4775: "Assumed Strain Method in Finite Elements for Layered Plates and Shells with Application on Layer Delamination Problem", in addition to the "Young Researchers' Career Development Project – Training New Doctoral Students" grant, both financially supported by the Croatian Science Foundation.

Dedication

I dedicate my work on this thesis to the memory of Prof. Nenad Bićanić. He introduced me to the world of academia and was always an inspiration. If it weren't for him, I wouldn't be pursuing my PhD.

Abstract

This thesis investigates the influence of specimen width on the mode-I fracture toughness of adhesively bonded plate-like specimens. First, the influence of different double cantilever beam (DCB) loading arrangements on the measured fracture toughness is investigated and an accurate method for determination of the traction-separation law of the interface using the direct approach with the digital image correlation (DIC) is presented. An additional set of DCB experiments with three different specimen widths is conducted to study the influence of the width on the measured fracture toughness. A novel technique for measuring the relative displacement of the plates with full-field DIC, termed Symmetry Based Top Surface Analysis (SBTSA), is developed to measure the actual crack position and shape, as well as the crack area increments. By using this value in the finite-difference form of the definition of critical energy release rate (Area method) any dependence on the beam theory assumptions is avoided. Experimental results suggest that wider specimens have substantially higher fracture toughness. An original numerical model was developed using the Q4U3 plate elements connected by the kinematically compatible interface elements with an embedded exponential traction-separation law. A numerical study of the efficiency and robustness indicates good convergence properties of the proposed model. The aforementioned approach to compute the fracture toughness using SBTSA and the Area method was validated by means of virtual experiments. The comparison of experimental and numerical results for DCB specimens with different widths shows good agreement of the global load-displacement response, with an excellent agreement of the crack front shape and size of the damage process zone.

Keywords: adhesive joints, delamination, cohesive zone model, digital image correlation, finite element method, plate structures

Sažetak

Doktorski rad istražuje utjecaj širine uzorka na lomnu otpornost lijepljenih slojevitih plošnih nosača. Za početak se preispituje utjecaj različitih prihvata testa dvostruke konzole na izračun lomne otpornosti te se predstavlja precizna metoda određivanja konstitutivnog zakona ljepila direktnim pristupom uz tehniku korelacije digitalne slike kako bi se odredili materijalni parametri međusloja (eng. *interface*). U sljedećem setu eksperimenata s tri različite širine na testu dvostruke konzole se ispituje isključivo utjecaj širine uzorka na lomnu otpornost. Originalna tehnika mjerenja relativnih pomaka ploča duž kontinuirane 2D domene pod nazivom SBTSA (eng. *Symmetry Based Top Surface Analysis*) je razvijena kako bi se mjerila stvarna pozicija i oblik pukotine te inkrementi površine pukotine. Koristeći tako određenu vrijednost inkrementa za definiciju kritične promjene oslobođene energije u formi konačnih razlika (metoda površine) se nigdje ne usvaja pretpostavka gredne teorije. Eksperimentalni rezultati ukazuju da uzorci plošne geometrije imaju značajno veću lomnu žilavost. Originalan numerički model je razvijen koristeći Q4U3 konačne elemente ploče koji su spojeni pomoću kinematički kompatibilnog elementa međusloja s izvedenim eksponencijalnim konstitutivnim zakonom. Numerička studija efikasnosti i robusnosti ukazuje na dobra konvergencijska svojstva predloženoga modela. Ranije navedeni pristup izračuna lomne žilavosti pomoću SBTSA metode i metode površine je validiran na virtualnim eksperimentima pomoću numeričkog modela. Usporedba eksperimentalnih i numeričkih rezultata pokazuje dobro poklapanje sila-pomak krivulje uz odlično poklapanje oblika pukotine i veličine plastične zone.

Ključne riječi: lijepljeni spojevi, delaminacija, model kohezivne zone, korelacija digitalne slike, metoda konačnih elemenata, plošni nosači

Nomenclature

Abbrevations

#	number
A30	30 mm wide aluminium specimens
A60	60 mm wide aluminium specimens
A120	120 mm wide aluminium specimens
A240	240 mm wide aluminium specimens
AM	area method
BL	bilinear (law)
BSG	Bosch-Schreurs-Geers (model)
CBT	corrected beam theory
CT	compact tension (test)
CZM	cohesive zone model
DCB	double cantilever beam
DIC	digital image correlation
DPZ	damage process zone
ECM	experimental compliance method
EF	exponential fit
EPFM	elasto-plastic fracture mechanics
Err.	error
ESBT	enhanced simple beam theory
Eq.	equation
EXP	exponential law
FE	finite element
FEM	finite element method

FRP	fibre-reinforced plastic
INT8	eight-node interface element
LEFM	linear-elastic fracture mechanics
N/A	not available
NL	nonlinear(ity)
R-curve	resistance curve
ROI	region of interest
SBT	simple beam theory
SBTSA	symmetry based top surface analysis
SG	Savizky-Golay (filter)
SNB	single cantilever beam
TSA	top surface analysis
TSL	traction-separation law
S-N	strength vs number of cycles
TTM	tensile-testing machine

Math Symbols

A	area (of propagated crack)
a	crack length
a_{EQ}	equivalent crack length
B	width
D	plate bending rigidity
δ	interface separation
δ_{INIT}	interface separation at initial crack
δ_0	characteristic length
δ_C	critical interface separation
δ_I	interface separation in mode-I
Δt	pseudo-time increment
Δl	elongation
ϵ	deformation
E_T	total energy
e	Euler's number (2.718)

E	modulus of elasticity (of substrate)
E_A	modulus of elasticity of adhesive
E'_A	effective modulus of elasticity of adhesive
G	shear modulus
G_I	energy release rate in mode I
G_{IC}	critical energy release rate in mode I
h	substrate height
I	moment of inertia
J_{INT}	J integral
J_{IC}	critical value of J integral in mode I
k	shear correction coefficient
K	penalty stiffness
K_S	softening penalty stiffness
K_0	initial penalty stiffness
K_I	stress intensity factor (in mode-I)
L	substrate length
r_y	plastic zone radius (first order approximation)
L_x	FE length along the x direction
L_y	FE length along the y direction
l_{DPZ}	cohesive zone length
θ	cross-sectional rotation at load line
M	applied moment
ν	Poisson's ratio
P	force
t_A	adhesive layer thickness
σ	stress
σ_{MAX}	maximum traction
V	internal virtual work
W	work required to create new surfaces
η	natural coordinate axis
ξ	natural coordinate axis
ω	transversal plate deflection
π	the potential energy

Contents

Chapter 1

Introduction

Historically, the first written account of adhesive application is the Greek myth of Daedalus who constructed wings from feathers glued by wax. Until the 20th century, most of the structural adhesives were of natural origin, while the testing methods were limited to breaking a sample by hand. Adhesive joints are nowadays applied in a variety of engineering structures, primarily in the automotive and aerospace industries. They reduce the stress concentration since, in contrast to traditional mechanical joints (e.g. bolted joints), no weakening of structural components is required.

There are many structural adhesive types available for various purposes as an alternative to traditional mechanical fasteners. Epoxy structural adhesives have versatility such as thermal and chemical resistance, making them a common choice in automotive and aerospace applications. They can also be used solely for void-filling to enhance rigidity and reduce noise (noise and vibration sealants) in applications like turbine blade manufacture. Acrylic adhesives are applied to a variety of surfaces (substrates), including plastics and oily metals, since they do not require surface preparation. Polyurethane adhesives are typically lower-cost but also offer other advantages like high impact resistance and high humidity resistance. Although their stiffness is relatively low, this feature can be well suited for applications where flexibility is needed, e.g. bond between dissimilar materials.

The following five paragraphs are dedicated to applications of adhesives in various industries [1].

In aerospace engineering, adhesive bonding is typically used for fuselage and wings. Challenges arise due to surface treatment prior to bonding, which depends on the type of aluminium substrate. In terms of efficiency, there is still room for improvement since thin-wall panels are

designed only up to buckling load even though stiffeners prevent the occurrence of buckling. This is to prevent large out-of-plane deformations that may also cause debonding of stiffeners or delamination of composite structure. Moreover, despite the effort made to improve the predictive capabilities of modelling, additional mechanical fasteners are usually included for safety and this component is then tested, instead of modelled, before use. Testing must also account for durability requirements. Requirements in terms of joint flexibility (stiffness) are two-fold, joint strength is desirable but ductile adhesives may actually lead to better performance by spreading loads over larger areas.

In the automotive industry, adhesive joints are used to reduce weight and decrease fuel consumption. Primary load case is road accident simulation where passenger safety is paramount, making impact resistance a primary requirement. In addition, materials are exposed to varying humidity and temperature. A typical automotive application is the mounting of glass windshield. In fact, in the experiments presented in the present thesis, epoxy adhesive that is manufactured for bonding auto panels made from metals or composite materials is used. Typically, joints are exposed to shear loads. Given that the anti-corrosion coatings are applied prior to structural adhesives, surface preparation of substrate has a significant influence on the bond strength. Hybrid adhesive bonding is a combination of adhesive bonds with spot welds and mechanical fastening. This technique has recently started being used at the automotive bodyshell assembly lines.

In civil engineering applications, composites are mainly used to strengthen existing structures by bonding fibre-reinforced plastic (FRP) to the surface. In order to better match the stiffness of the joined structures, masonry or timber structures are typically repaired by lower stiffness FRP, while concrete is strengthened by higher stiffness FRP. Some attempts were made using FRP shells or profiles for new structures such as bridges.

In wind energy applications, rotor wind blades are assembled using thick layers of adhesives. Due to confidentiality issues of manufacturers, reports of failure causes are lacking but it is generally accepted that adhesive joints may be a leading contributor. Thickness of the adhesive can be up to 30 mm to compensate for manufacturing tolerances, but voids can still be found upon inspection. Composite layers can be made from glass fibre or carbon fibre fabrics that behave well in fatigue and corrosion scenarios. Fatique analysis of a wind blade is usually based on the experimental S-N data (Strength vs. No. of cycles). Advanced approaches use elasto-visco-plastic models [2] that should also account for additional mechanisms such as creep, influence of

loading rate and ageing.

In electronics [3, 4], semiconductor devices and integrated circuits are bonded to various surfaces and interfaces. Bonding with adhesives is increasingly replacing the traditional methods of joining by soldering. In some cases, such as robotics, the applications may demand reduced instead of increased adhesion, particularly the on-demand switch between the two [5]. Furthermore, the property of reduced adhesion could potentially lead to increased recycling of electronics which typically have quite a short service life. In most applications electrical conductivity is a requirement. In terms of structural loads, adhesives are exposed primarily to thermal cyclical stresses. Failures typically arise due to debonding or delamination. This often results in undesirable moisture penetration and, consequently, in damage from corrosion or even in short circuits.

One of the most severe failure modes of adhesive joints is debonding, which occurs when the connection between the joined parts is lost. The two common failure modes in adhesive debonding are cohesive failure, in which the adhesive material is broken, and interfacial failure, in which the adhesion between the adhesive layer and the substrate is lost prior to cohesive failure. In this thesis, adhesive debonding is referred to only in terms of the cohesive failure, as the contribution of interfacial failure becomes negligible in case of adequate preparation of bonding surfaces [6]. Cohesive failure of the adhesive layer is usually studied in the framework of fracture mechanics.

Fracture mechanics is a field of mechanics that deals with the propagation of cracks in materials [7]. It is divided into the discipline of linear elastic fracture mechanics (LEFM) and elasto-plastic fracture mechanics (EPFM). While the former assumes an infinite stress near the tip of a sharp crack, the latter is a more realistic approach with material near a crack yielding when the stress reaches yield strength thus forming a plastic zone. Defects in adhesive joints, such as air entrapment, are introduced through the manufacturing process [1]. Throughout service life, structural loads may cause propagation of initial crack originating from manufacturing defects in the material. Damage tolerance design philosophy [7] allows the presence of "safe" existing defects that do not propagate further, i.e. damage initiation is allowed but damage propagation is not.

Crack can propagate in three modes [7]. The opening mode (mode I) is usually the most critical load case. Therefore, adhesive joints are typically designed to carry primarily the load in mode II and mode III [1], which represent sliding and scissoring (tearing) shear, respectively,

although a combination of two or more delamination modes, called mixed-mode delamination, is very frequent. Mode I delamination may still dominantly occur during buckling or bending of curved composite structures such as polymer-coated metals. In this thesis focus will be exclusively on mode I (opening) delamination.

Testing of adhesive joint and identification of material properties is necessary prior to structural design and subsequent application in different fields of engineering since mechanical properties must be well known to properly design any structural component. Adhesive resistance to debonding, or delamination in the case of composites, essentially represents the change in the total potential energy of the system during crack propagation. The most common parameter to describe the fracture resistance of adhesives is the critical energy release rate (G_c), which is derived within the framework of LEFM [3]. By applying LEFM to adhesive joints, it is assumed that the adhesive is infinitely stiff and perfectly brittle, while the remaining part of the structure (adherends) is linear-elastic. Such assumptions lead to a stress singularity at the crack tip, which is clearly not realistic. For adhesives, which are essentially polymers, not only are stresses at the crack tip finite, but a region is developed ahead of the crack tip, where the energy is dissipated before propagating the crack. This region is called the plastic zone or the damage process zone (DPZ) [7].

Double cantilever beam (DCB) is the most common test specimen for determining fracture resistance in mode I and it is used in standards [8–10]. In these standards, the critical energy release rate is exclusively used to characterise the fracture resistance of adhesives. By applying corrections based on the measured compliance, LEFM theory can be used to accurately assess the fracture resistance of not only brittle, but also ductile adhesives [11].

DCB test specimens are manufactured by glueing together two equal adherends/arms in order to later expose them to a symmetric opening load. An initial crack is introduced by inserting a thin film, e.g. aluminium foil, in an otherwise glued interface and pulling the specimen apart causes crack propagation along the bonded surface. Crack propagation increases the DCB cantilever span which makes this problem nonlinear (nonlinear relationship of the prescribed opening displacement and applied load).

British standard for mode-I delamination/debonding [8] accounts for the following loading arrangements (also known as load introduction systems): loading holes, load-blocks, and piano hinges (more details are given in Section 3.2 of this thesis). The main difference between these loading arrangements is the way the load is transferred to the specimen. In fact, the basic closed-

form expressions for the critical energy release rate assume that the load-line displacement is twice the deflection of each DCB arm at the point of application of the load. Moreover, it is assumed that the load is applied on each DCB arm directly on their reference axes. The distance from the point of application of the load to the crack tip represents the crack length. Such conditions are representative only for the loading arrangement with loading holes and pins. However, DCB arms are often too thin to be drilled across the width (which is the case for thin composite specimens), and alternative loading arrangements, such as loading blocks and piano hinges, must be used. In addition to these three types of loading arrangements, other loading arrangements have been proposed in the literature [12, 13], but are not considered in this thesis for the sake of simplicity.

Testing procedure typically requires the continuous monitoring of the force-displacement response from the tensile-testing machine (TTM) and visual measurement of the crack length along the specimen's edge, which has been traditionally done by means of a travelling microscope or video cameras [8, 9]. This procedure may be inconvenient and prone to human error. To avoid this, an additional optical measuring equipment is used in this thesis, namely the digital image correlation (DIC) technique [14] that has become commonplace in laboratories for experimental mechanics.

Regarding the DIC usage in the adhesive joints testing, Gorman and Thouless [15] recently presented procedures for measuring the cross-sectional rotation, initial crack tip separation and cohesive zone length in DCB tests by applying full-field DIC capabilities. DIC can be utilized for crack detection [16, 17] in mode-I delamination problems [18]. Sun and Blackman [19] showed the importance of crack length measurement in procedure from the British standard. They proposed measuring the crack tip at a position where the relative separation between the substrates has a maximum negative value which occurs when the interface is in compression. At this position, there is an extreme (minimum) of the deflection of the upper substrate, which, according to Euler-Bernoulli beam theory, corresponds to the position where the angle of cross-sectional rotation is zero. Rather than the measured crack tip, this position could act as a much more accurate clamping point for the DCB arms, since a very common assumption in LEFM-based methods [20] is that each DCB arm acts like a (fully clamped) cantilever beam. Same authors [19] also confirmed [21] that the critical crack tip opening can be determined by reading the opening along length at which the crack in the observed image propagates.

Measurements from the DCB experiment are the input data required to compute the fracture toughness of the adhesive using methods from the testing standards known as data-reduction

schemes [8]. For example, Berry [22] derived a simple data reduction scheme called 'experimental compliance method' (ECM) that instead of typical cubic dependence of deflection on the crack length assumes a polynomial function of an arbitrary degree. This is particularly suitable in cases when the experimental measurement of compliance is not consistent with the beam theory. Ripling et al. [23] first presented the 'simple beam theory' (SBT) under the assumption that the interface material is perfectly stiff and brittle. After having noticed that the SBT assumptions underestimated the real deflections, they added a correction that increases the measured crack length and called this approach the 'corrected beam theory' (CBT). Hashemi et al [24] presented the load-block correction on the measured displacement, as well as large displacement correction [25]. They also provided a useful expression for the flexural modulus of substrates. Anderson and Stigh [26] introduced the concept of equivalent crack length and assessed the accuracy of commonly used data-reduction schemes. Škec and Alfano [20] used the equivalent crack length to derive so-called 'enhanced simple beam theory' (ESBT) that does not require crack length measurements and takes into account the arm rotation at the crack tip due to shear.

Alternative theories to LEFM, such as J integral [27] and cohesive-zone models (CZM) [28,29], are capable of taking into account the non-linear material behaviour that occurs in front of the crack tip during debonding of adhesive joints. In particular, the J integral can be used to compute the so-called non-linear energy release rate [7] and its change before and during crack propagation, while CZMs are nowadays widely used in the framework of the finite-element analysis to model debonding, delamination and crack propagation in general [30–32]. In contrast to the limit load analysis, the approach with CZM enables inelastic behaviour and a gradual reduction in load-carrying capabilities. By using the J-integral approach, one can experimentally determine the traction-separation law (TSL) from the DCB experiment [15]. Retrieved material properties are typically used in numerical simulations for comparison with experiments.

The procedure of direct identification of the TSL was made possible by Olsson and Stigh [33] who derived the DCB solution for the J-integral as a simple function of force and load-line rotation. Sorensen et al. [34] implemented direct identification of the TSL on DCB specimen loaded with moments by measuring the crack tip opening with extensometer. Catalanotti [35] managed to directly measure the J-integral from the experiment rigorously, using measurement of the displacement and strain fields, as defined originally by Cherepanov [36] and Rice [27] independently. Shen and Paulino [37] were the first to show how the material properties of the interface can be directly identified with the use of DIC. Sarrado et al. [38] studied the effect of

adhesive thickness on its cohesive zone model parameters, both in modes I, II and a combination of the two. In essence, thicker adhesive seemed more ductile but they concluded that this effect seems insignificant since its magnitude is almost comparable to experimental noise. Joki et al. [39] underlined a serious difficulty with measuring TSL by the J-integral approach for small openings since, due to anticlastic bending and stress state variation across the specimen width, they can be reduced or even become negative. Clearly, a way around this could be to somehow measure openings across the width. Heshmati et al. [40] studied the influence of moisture and freeze-thaw cycling on cohesive law obtained by direct identification.

There are alternative methods of the TSL identification which rely on inverse analysis or on analytical/empirical methods. Škec derived a three-phase analytical solution to extract TSL parameters [41]. Monsef et. al. [42] developed an indirect method to extract the TSL parameters using only the force-displacement data. Recently Huo et al. [43] studied separation along the interface in detail to extract the TSL parameters via semi-empirical approach.

Adams [44] explained how the retrieved elastic properties are useful in both bulk and thin layer configurations, while the same may not be true for strength parameters. In any case, there was controversy [45] as to whether the tested mechanical properties of the bulk material are representative of the thin layer adhesive. In this thesis, elastic properties will be assumed as independent of the geometry/constraint.

A mathematical description of a real-world problem that can be solved using computational methods will be referred here as a numerical model. Finite element method (FEM) [46, 47] is a discrete numerical approach that can convert a continuous mechanical problem into a set of mathematical equations, e.g. a set of partial differential equations. The FEM can approximate a solution via variational calculus by minimizing the potential energy of a mechanical system. The physical domain of a problem is encircled by a boundary for which a solution (or its derivative) must be known in advance, i.e. boundary conditions must be defined. In every element we assume the form of the solution across its domain by interpolating between the nodal values. Finding an adequate interpolation, i.e. a function that closely resembles the exact solution, eventually leads to fewer elements required for an accurate simulation and in turn lower computational cost. The division of model into parts (finite elements) is called mesh generation. Better approximation is achieved with more elements, i.e. denser mesh. However, dense meshes are computationally demanding mostly in terms of RAM, while the complex interpolation functions are typically CPU intensive. Technological advancement in computational capabilities has paved the way for

FEM to become a dominant approach in solving various engineering problems.

Substrates (arms) of the DCB can be described effectively by either a beam or a plate model. Beam is a load bearing structural element with one dimension significantly larger than the other two, while the plate model has one dimension significantly smaller than the other two. As a general rule, if the ratio of these two dimension is larger than 2, then a simple beam model is appropriate for use. Fundamental beam theories are known as the Euler-Bernoulli theory and Timoshenko beam theory. The principal difference is that the latter accounts for shear deformation, which is essentially the difference between the slope of the beam's axis and the actual rotation of the cross section. Likewise, plate theory equivalents are the Kirchhoff and Mindlin plate theory, with the latter accounting for shear deformation in two dimensions. When modelling the DCB test, in which only the relative nodal transversal displacements in mode-I are considered, membrane degrees of freedom contained in the shell finite element are redundant. Therefore, in numerical simulations presented in this thesis, DCB plates were modelled using plate finite elements. Many researchers even resort to 3D solid ("brick") elements for which all three dimensions have the same order of magnitude. This is made possible due to an increase in computational power since this approach requires a significantly higher number of degrees of freedom, i.e. number of equations to be solved.

Typically the beam theory is utilised for the DCB problem, although this is mainly due to the simplicity stemming from a well-known closed-form solutions. Besides, the geometry of a DCB test is typically beam-like, rather than plate-like. In this thesis, the plate theory will be used to model the substrates of DCB specimens of varying width. This is appropriate not only for plate-like geometries, but also for beam-like specimens since the free arm can be better described by plates when the crack is short.

Quadrilateral (4-noded) plate elements are an adequate choice for describing the DCB arms due to their simple rectangular geometry. Considering that the deflection curve of a cantilever beam (DCB) can be exactly defined by a cubic polynomial, the desired interpolation function is of cubic order. These requirements are effortlessly satisfied by the chosen finite element Q4U3 presented in [48], which has a displacement-based linked interpolation.

Numerical simulation of the delamination can be performed in two ways. The first one is to directly apply fracture mechanics [7], e.g. virtual crack extension or virtual crack closure technique, while the second approach uses the framework of finite element analysis with either damage mechanics or softening plasticity [30]. LEFM provides methods that are quite effective

in predicting the delamination growth of a crack. When modelling crack propagation, the basic assumption is that delamination propagates when the energy release rate is greater than the critical value that is a material parameter of the interface. However, LEFM methods cannot be applied to predict the initiation of delamination, limiting them to problems in which the initial position of the crack is known beforehand. To overcome this, strategies have been developed to model the interface based on damage mechanics or softening plasticity, which is often referred to as cohesive zone modelling (equivalent to the aforementioned CZM).

The cohesive zone model (CZM) was introduced by Dugdale and Barenblatt [28] in the early 1960s. It is a useful tool that enables the use of fracture mechanics parameters (energy-based approach) in finite element models. Constitutive behaviour of material exhibits nonlinearity that requires an iterative solver (e.g. Newton-Raphson method) and definition of the so-called traction-separation law (TSL).

Alfano [49] studied the influence of different TSL shapes on convergence properties of DCB simulation to find the two-part exponential law most precise and the bilinear law the most efficient one. All this was performed for reversible TSL that does not account for damage in case of reloading but only for softening plasticity. Instead of a two-part exponential law, the exponential law is typically defined by a single expression as derived originally in the early 90s by Needleman and Xu [31, 50]. This law can be used for mixed-mode loads, as well as mode-I loading, which is relevant to this thesis. Nowadays, this exponential law can also be found in literature as BSG (Bosch-Schreurs-Geers) model [32] which is slightly modified to have a more realistic coupling behaviour in a sense that the mode II friction does not increase the mode I toughness. It is interesting to note that the research in the early 80s [51] suggested that the binding energy of bi-metallic interfaces is well described by the exponential expression. This was studied for purely normal separation by means of atomistic calculation from molecular dynamics.

Reedy et al. [52] used springs to describe the interface and shells to describe the DCB arms in a numerical model for a composite delamination. Davila [53] modelled the relative displacements at the interface by taking into account the rotation that kinematically corresponds to the plate degrees of freedom. Russo and Chen [54] derived a numerical model with a corotational formulation for geometrically nonlinear analysis with slender elements for composite plies, along with the higher-order integration. They were able to model delamination with elements that are much larger than the cohesive zone length. Assuming the feasibility of the proposed method, this is significant progress since mesh size requirements were typically very computationally prohibitive

limiting the simulation to laboratory-size coupons. They also indicated that the approach to reduce computation requirements by artificially increasing ductility [55] is considerably imprecise in case of a double delamination problem [56]. In addition to this, they provided future work guidelines to include substrate shear deformation to overcome the oscillations in deflection behind the crack tip.

Following the trends in the last couple of decades [7], this thesis aims to characterize and predict the geometry dependence of adhesive's fracture toughness. These efforts are necessary when traditional single-parameter fracture mechanics is inadequate to describe the real behaviour of materials, including the adhesive joints and composites. The laboratory test results may not be transferable to complex geometries and this presents an obstacle to an accurate and safe design of real structures.

The influences of geometry that are relevant to this thesis were first qualitatively explained by Kinloch and Shaw's [57] in the early 1980s. They found that the measured bond toughness is reduced when the bond thickness does not allow the plastic zone to fully develop due to the restrictions imposed by the substrates. In addition, a correlation of thicker bonds with unstable crack propagation known as the stick-slip fracture was noticed. More importantly for the present work, increase in width was correlated with increased fracture toughness. This phenomenon is one of the principal subjects of this thesis so the next few paragraphs are dedicated to additional theoretical background on this matter.

Geometrical influences on the adhesive's fracture toughness can be formally divided into two categories [58], namely the external and internal constraint effects. The former represents effects outside of the thin adhesive layer, such as substrate arm thickness [59] or state of deformation in general. The latter represents effects within the thin adhesive layer that can affect the size and shape of the plastic zone, primarily the thickness and the width of the adhesive layer.

Note how the terms geometry dependence or constraint effects [58] are used here interchangeably. Actually, the term crack-tip (stress) triaxiality [7] is also occasionally used, as well as the plane stress - plane strain transition [7]. Higher stress triaxiality occurs in the interior of the plate where the plane strain conditions are dominant. On the other hand, lower stress triaxiality occurs at the edges where the plane stress conditions are dominant. In short, the degree of stress triaxiality depends on the magnitude of the stress acting at the crack tip in the direction of crack propagation in the case of mode-I. This stress component is called T-stress [7, 60]. Positive T-stress increases the size of the plastic zone and makes the crack path unstable, while negative

T-stress causes the opposite. Gupta [61] made a detailed literature review about the T-stress in adhesives. Imanaka [62] defined the stress triaxiality parameter S as a ratio of Von Mises stresses and mean stresses. He found this parameter to be 1/3 for the bulk material and 2 for the thin layer material acting as a bond, with higher value of this parameter corresponding with higher maximum principal stress, especially for the case of epoxy adhesives.

Davidson and Schapery [63] studied the effect of the finite width of a composite structure on the energy release rate which can overestimate it by apparent ca. 30-40 percent. Depending on the considered plate's aspect ratio, they also provided finite width correction factors for use with the energy release rate for plane stress conditions. Furthermore, they theorised that area method with true surface crack area extension should be used in order to account for the changing crack curvature. This approach is adopted in the present thesis instead of the aforementioned data-reduction schemes that assume a straight crack front orthogonal to the longitudinal axis.

Jumel et al. [64] developed a beam on elastic foundation model that takes into account the anticlastic curvature. Furthermore, they stressed how the crack front curvature can have a considerable effect on the energy release rate. This was also previously investigated by Davidson et al. [65] who demonstrated how the error in the energy release rate may reach up to 40 percent for small crack length versus beam width ratio. Budzik et al. [66] studied the crack front curvature in bonded joints, namely the single cantilever beam (SNB) and DCB joints, to numerically find the causes of curvature to be anticlastic bending and stress heterogeneity in the bondline. They also found that the specimen edges, ca. 0.6 mm wide strips, endure mode II and III in addition to the mode I, which they experimentally confirmed by observing the so-called river patterns under a microscope. Furthermore, they expressed the curvature of the crack front using a simple real-exponent polynomial expression so that their model can account for curved crack front with the use of curved shell finite elements. This model predicts lower energy release due to crack curvature effect.

Even though the primary intention of CZM is to simulate damage propagation at a low numerical cost, as one would expect the elastic behaviour of a joint can also be successfully simulated. Hesebeck [67] focused on the improvement of the CZM model elastic behaviour by considering the capability of the lateral contraction using Tsai's [68] closed form solution for the rectangular layers between rigid boundaries. Aside from lateral contraction, this model analogously accounts for mid-section higher apparent stiffness stemming from the prevention of lateral contraction in plane strain conditions. For academic purposes at least, Hesebeck [67]

recommended modelling spatially varying stiffness based on the distance from the free surface. The present thesis is a good candidate to test this. However, a good agreement was achieved using the usual homogeneous approach with spatially independent interface stiffness.

Cabello et al. [69] developed a general analytical elastic foundation beam model that is applicable to both flexible or rigid adhesives, where the former represents almost incompressible material ($\nu = 0.5$) with unusually high total strain. They showcased the importance of the adhesive layer's width-to-thickness ratio (B/t_A) by accounting for the stress state in the two transversal directions. Their model is comparable to the one previously published [64, 70] for simpler limiting cases, such as full plane strain and combination of plane strain and plane stress in a cross transversal direction, respectively. The model was validated for three cases, namely flexible adhesive in addition to the rigid adhesives with higher and lower B/t_A ratio. Important to note is that they focused exclusively on modelling the elastic behaviour of an adhesive joint before the crack propagation.

The work of Kinloch and Shaw [57] was extended by Manterola et al. [71] who quantified the influence of width-to-thickness ratio on mode I fracture toughness. The mentioned variation in fracture toughness is due to combination of two constraint effects. First is the well-known increase in toughness in case of plane stress condition [57, 60], while the latter is the lateral contraction near the edges resulting in decreased section area. Using their approach, one can measure the fracture toughness for a specimen with a large B/t_A ratio and then derive the toughness for cases with different ratios. One thing to note is that they relied on the previously mentioned beam on elastic foundation model that is unable to reproduce the anticlastic bending of the substrates. In any case, their approach [71] may be useful to explain the experimental results of the present thesis.

In this thesis, the aim is to numerically and experimentally investigate the influence of the specimen width on the DCB delamination. The starting hypothesis made in the present thesis can be summarised as follows:

- DIC will facilitate accurate identification of material properties on narrow DCB geometries,
- the indentified material properties will be sufficiently accurate and representative to model wide DCB geometries,
- the developed numerical models will be robust and efficient in comparison with competitive models.

The external constraint effects will be considered by using the plate theory to model the substrates. However, attempt to fully account for the internal constraint effects will not be made since the starting hypothesis is that wide specimens can be modelled using the test results for the narrow specimens as is usually assumed. Thin layer will not be modelled by a single-parameter fracture mechanics, but by CZM which is basically a simple multi-parameter approach.

The aims of the research conducted for the present thesis are given hereafter:

- conduct an experimental programme of DCB tests with variable width,
- apply the DIC technique to study the behaviour of layered plates with an emphasis on the crack front and DPZ shape,
- model the DCB arms using the plate finite element formulation with a higher order linked interpolation,
- develop an interface finite element in a way that the interpolations used for separation are kinematically compatible with the plate degrees of freedom,
- describe the constitutive model of an interface using a TSL shape that is sufficiently precise and robust on sparser meshes,
- compare the experimental and numerical results to validate the presented model and experimentally identified parameters of an interface.

The thesis is organised as follows. Chapter 2 consists of the selected introductory theory relevant to this thesis. Elementary topics such as the crack tip plasticity and the stress state transition are covered, along with a discussion about the plastic zone suppression. At the end of Chapter 2, a brief presentation of data-reduction schemes is given, while a rigorous study of their accuracy is presented in the next chapter. Moreover, in Chapter 3, details about the preparation of the specimens and DIC measurements are given, with special emphasis on the comparison between the crosshead and load-line displacement and its significant effect on fracture toughness. This is followed by a presentation of the method for extracting the actual shape of the traction-separation laws (TSLs) and a novel experimental procedure for the full-field observation of delamination necessary for plate-like specimens. Chapter 4 is dedicated to the numerical model consisting of quadrilateral Q4U3 plate and kinematically compatible INT8 interface elements. In the same chapter, an effort is made to address convergence issues typical

for delamination simulations, which transfer to high computational costs and in turn limit their real-world application. In this thesis, a novel approach to an existing data-reduction scheme called the 'area method' is proposed along with the aforementioned full-field observation The approach is also validated on the synthetic data generated from the virtual experiments. Chapter 5 is dedicated to a comparison of the experimental and numerical results, followed by a summary of thesis's contributions in the final chapter.

Chapter 2

Underlying theory

In this chapter, fundamental concepts of fracture mechanics are briefly described. Linear Elastic Fracture Mechanics (LEFM) was developed in the 20th century primarily by pioneers Griffith [72] and Inglis [73] in the 1920s. Thanks to the work of Irwin [74, 75] and co-workers in the 1960s, fracture mechanics was extended to include non-linear material behaviour, such as plasticity. This led to still evolving theory of Elastic-Plastic Fracture Mechanics (EPFM), with current efforts [2] aiming to account for other sources of non-linearity such as viscosity, fatigue and dynamic effects.

This chapter explores textbook topics, such as the plastic zone, and also considers the possibility of its suppression by the substrates which may have an influence on fracture parameters as an internal constraint effect. At the end of the chapter, in addition to J integral derivation, a brief overview of other selected data-reduction schemes is presented.

2.1 Type of Loading

Generally, type of structure failure depends on the material brittleness, i.e. brittle materials will fail from fracture and ductile materials will fail from yielding. Low temperatures, high strain rates and triaxial stress state generally suppress yielding and accommodate brittle fracture. Structures subject to yielding-dominant failure are designed via limit load analysis in which maximum strength of material must not be exceeded by acting stresses. On the other hand, fracture-dominant yielding occurs when there are significant defects present in brittle material which might lead to crack propagation at stresses lower than yield strength (σ_{YS}) of material. This approach is also known as energy based because the total energy of the system is lowered

when the crack growth occurs. There are three modes of crack propagation, namely the opening mode-I and the shearing modes II and III (Figure 2.1).

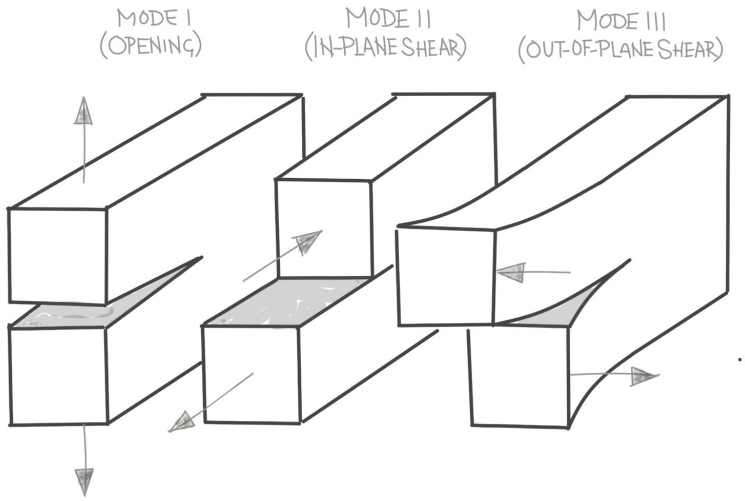

Figure 2.1: The three modes of loading (figure redrawn from [7])

Delamination is one of the most important and severe failure modes of composite structures. Resistance to delamination is essentially resistance to fracture of the interlayer connection, which is expressed in terms of fracture-mechanics parameters such as the critical energy release rate (G_C), the stress intensity factor (K_C) or the J integral.

2.2 Fracture Toughness

The Griffith energy balance states that the change in total energy E_T in respect to infinitesimal increase in crack area dA is equal to

$$\frac{dE_T}{dA} = \frac{d\Pi}{dA} + \frac{dW_s}{dA} = 0 \tag{2.1}$$

where π is the potential energy from the internal strain energy and external forces, while the work required to create new crack surfaces is denoted W_s. This approach was further developed by Irwin [74] who defined the change of the potential energy as the energy release rate,

Crack growth occurs when the energy release rate approaches a critical value,

$$G_C = \frac{dW_s}{dA} \tag{2.2}$$

which is a material property called **fracture toughness** (or fracture resistance). Substituting

2.2 in 2.1 yields

$$G_C = -\frac{d\Pi}{dA} \tag{2.3}$$

which is valid only during crack propagation. The potential energy can be defined as follows

$$\Pi = U - E_P \tag{2.4}$$

where the strain energy is denoted as U and the work done by external forces as E_P.

Now consider a cracked plate, very similar to compact tension (CT) specimen, depicted in Figure 2.2. Load is introduced to the plate by displacement control which means that the external forces are equal to zero, i.e. $E_P = 0$, while the potential energy can be expressed as the area under the force-displacement curve

$$U = \int_0^{\Delta} \frac{1}{2} P d\Delta \tag{2.5}$$

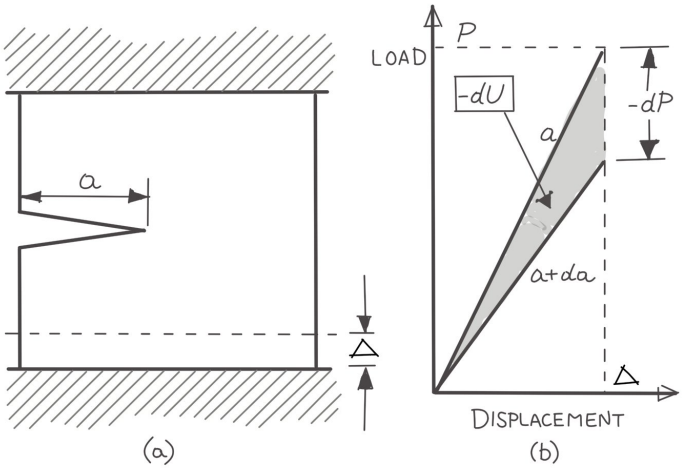

Figure 2.2: Cracked plate at a fixed displacement (figure redrawn from [7])

Assuming a straight crack front, crack area can be written as $A = BdA$, where B is the plate width and a is the crack length. Therefore, the critical energy release rate for a considered problem with prescribed displacement Δ reads

$$G_C = -\frac{1}{B}\left(\frac{dU}{da}\right)_{\Delta} = -\frac{\Delta}{2B}\left(\frac{dP}{da}\right)_{\Delta} \tag{2.6}$$

Substituting for compliance $C = \Delta/P$, i.e. inverse of the plate stiffness, the critical energy

release rate is given by expression

$$G_C = \frac{P^2}{2B}\frac{dC}{da} \tag{2.7}$$

also known as Irwin-Kies equation [76]. Solution for a double cantilever beam (see Figure 2.9) is straightforward. By defining the moment of inertia for a rectangular cross-section as $I = Bh^3/12$ and assuming a Bernoulli beam theory, a well-known known expression for cantilever beam reads

$$\Delta/2 = \frac{Pa^3}{3EI} \tag{2.8}$$

so that the compliance

$$C = \frac{\Delta}{P} = \frac{2a^3}{3EI} \tag{2.9}$$

leads to the critical energy release rate

$$G_C = \frac{P^2a^2}{BEI} \tag{2.10}$$

Aside from cracked plate or CT test, this expression is also valid for DCB test.

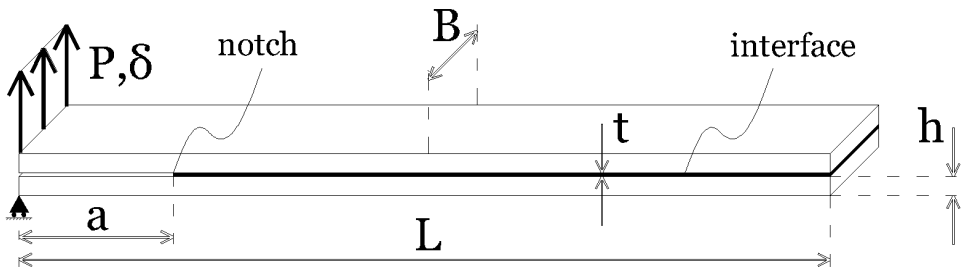

Figure 2.3: Geometry of the DCB specimens

2.3 Crack Tip Plasticity

It is well known [7] that LEFM predicts a sharp crack and infinite stress at the crack tip. This implies that LEFM is invalid for blunt notches.

In contrast, the concept of crack tip plasticity takes into account yielding zone near the crack tip where the material is unable to transfer tractions larger than the yield strength (Figure 2.4). Redistribution of traction must ensue in order to satisfy the equilibrium which results in a plastic zone ahead of a crack tip. Its radius was first expressed by Irwin [75] as

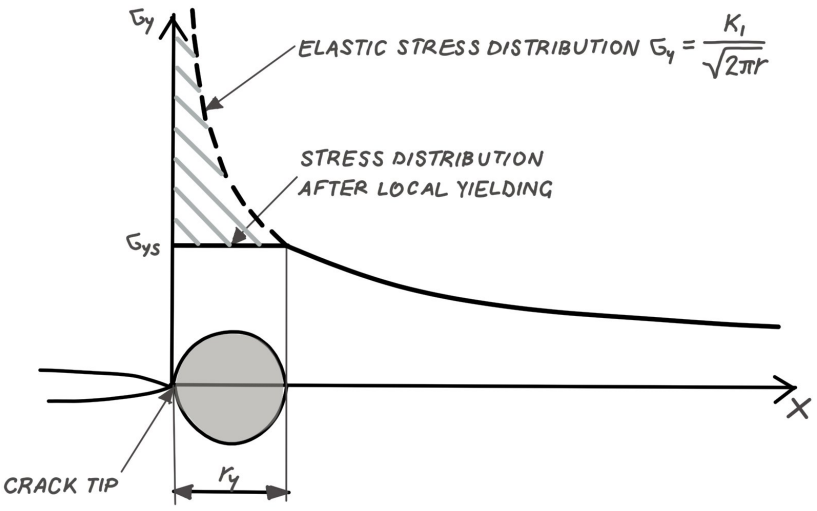

Figure 2.4: A first approximation to the crack tip plastic zone (figure redrawn from [60])

$$r_p = \frac{1}{\pi}\left(\frac{K_I}{\sigma_{YS}}\right)^2 = 2r_y \tag{2.11}$$

which is a first order estimate with stress intensity factor denoted as K_I. This definition of first order estimate assumes plane stress conditions, which may be taken as an approximation of stress conditions for very narrow DCB specimens since plane stress is present near the specimen edges across the width. In case of plane strain, the plastic zone radius becomes about three times smaller, according to Irwin [75], since yielding is suppressed by the triaxial stress state.

Material in the plastic zone can sustain less stress than it would if it remained elastic. Softening of plastic zone justifies the increase in the DCB (or CT) effective lever (a_{eff}). In a similar way to corrections used in some data-reduction schemes described later at the end of this chapter, Irwin plastic zone correction increases an effective crack length

$$a_{eff} = a + r_y \tag{2.12}$$

Even though the plastic zone shape is considered circular, there is no reason for this assumption aside from simplicity. Actually, shape was found to be slightly different in reality, although exact shape is not very significant since analyses are typically made along the x-axis (crack propagation direction). In any case, plastic zone shape is usually estimated by 2.11, which actually assumes stresses going to infinity near the crack tip [7], while in reality all stresses exceeding the yielding limit must be redistributed.

A way to achieve this is to substitute the Von Mises yield criterion in appropriate stress field

equations, which leads to a definition of plastic zone shape. See Refs. [7, 60] for more details on derivation presented hereafter.

The Von Mises yield criterion states that yielding will occur at

$$(\sigma_1 - \sigma_2)^2 + (\sigma_2 - \sigma_3)^2 + (\sigma_3 - \sigma_1)^2 = 2\sigma_{YS}^2 \tag{2.13}$$

where $\sigma_1, \sigma_2, \sigma_3$ are the principal stresses. Elastic stress field equations for a 2D case is given by the following equations

$$\sigma_1 = \frac{K_I}{\sqrt{2\pi r}} \cos\frac{\theta}{2}(1 + \sin\frac{\theta}{2}) \tag{2.14}$$

$$\sigma_2 = \frac{K_I}{\sqrt{2\pi r}} \cos\frac{\theta}{2}(1 - \sin\frac{\theta}{2}) \tag{2.15}$$

with polar coordinates (r, θ), while the third principal stress is either 0 or $\nu(\sigma_1 + \sigma_2)$, depending on whether a plane stress or a plane strain conditions apply. If plane stress is assumed, the Von Mises yield criterion gives

$$\frac{K_I^2}{2\pi r}\left(1 + \frac{3}{2}\sin^2\theta + \cos\theta\right) = 2\sigma_{YS}^2 \tag{2.16}$$

Solving for the radius and dividing by first order approximation from Equation (2.11) in case of plane stress conditions leads to a following dimensionless expression for plastic zone shape

$$\frac{r(\theta)}{r_y} = \frac{1}{2} + \frac{3}{4}\sin^2\theta + \frac{1}{2}\cos\theta \tag{2.17}$$

As expected, the first order approximation is indeed correct for $\theta = 0$, i.e. $r(\theta = 0) = r_y$. Also, for the case of plane stress conditions, plastic zone shape does resemble a circular shape. For plane strain conditions the third principal stress is equal to $\nu(\sigma_1 + \sigma_2)$, which leads to the following expression for plastic zone shape

$$\frac{r(\theta)}{r_y} = \frac{3}{4}\sin^2\theta + \frac{1}{2}(1 - 2\nu)^2(1 + \cos\theta) \tag{2.18}$$

Depiction of the calculated shapes (Eqs. 2.17,2.18) is shown in Figure 2.5. Stress triaxiality transitions across width from plane stress at the edges to plane strain at the inside. At the plate sides, no stresses along the width are present, which leads to biaxial condition of plane stress.

Proceeding inwards the degree of triaxiality increases and, starting from one limiting point, stress state corresponds to plane strain. This transition and interaction of the two stress state is usually described only qualitatively due to the involved complexities. Even though plane stress zone is larger than the plane strain, its stiffness E is lower than effective modulus of elasticity $E/(1-\nu^2)$ for the case of plain strain. This leads to so-called load shedding [60], which transfers the load from more compliant surface regions to the interior.

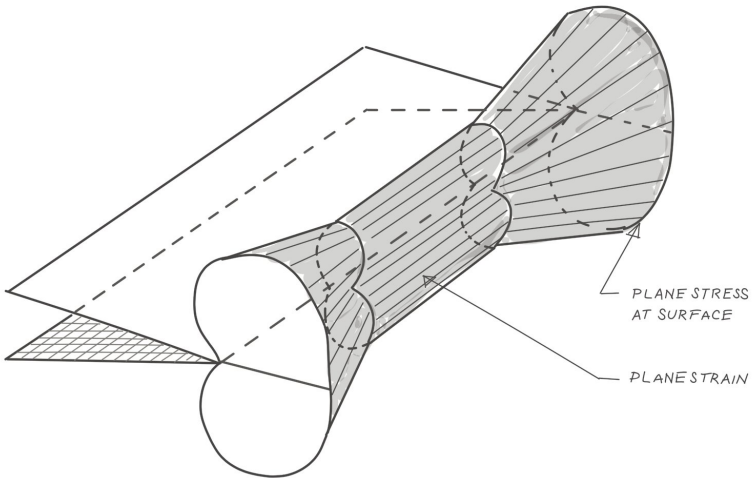

Figure 2.5: Through-width plastic zone in a plate of intermediate width (figure redrawn from [60])

Specimen geometry with full plane stress condition is empirically limited to width of $B = 2r_y$, while the plane strain dominates for widths higher than $B = 10 \cdot 2 \cdot r_y$, according to empirical rules given in [60].

In theory, knowing both the plane strain and plane stress material parameters can be combined to arrive at mixed condition parameters (e.g. in Ref. [77]).

2.4 Crack Path

Typically the crack propagation direction is orthogonal to the applied normal stress. However, crack propagation is not always confined to its initial plane. Angled cracks propagate in the direction of least resistance or the path of maximum driving force [7]. This can be demonstrated by analysing the stress fields using the Westergaard solution [7]. Crack will propagate in such a way as to maximize the energy release rate [7]. From Figure 2.6 is evident how the crack will tend to propagate in a stable manner across height. Even though fracture toughness is lower when not at middle, crack tends to approach the mid.

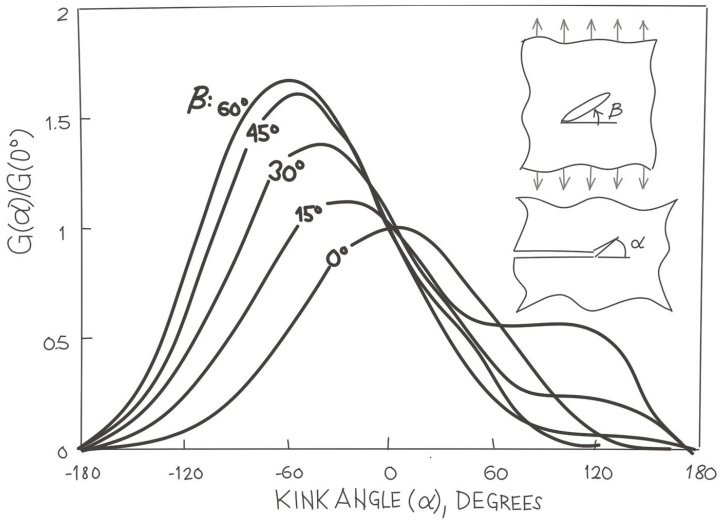

Figure 2.6: Local energy release rate at the tip of a kinked crack (figure redrawn from [7])

Change of fracture toughness during crack propagation is typically depicted by resistance curve (R-curve), which is basically a plot of fracture toughness vs crack extension. To account for variation of fracture toughness along the R-curve presented in Section 3.3 from the next chapter, suppression of plastic zone may be considered [57]. Fractured specimens geometry should be analysed for crack path in order to measure the degree of plastic zone suppression. The suppression of plastic zone is important for two slightly distinct reasons, the first is to exclude any constraint influence not associated with variable plate width, and second being the possible interaction of the two.

2.5 J Integral

The concept of J integral was introduced by Cherepanov [36] and Rice [27] independently in 1967 and 1968, respectively. J is a path-independent line integral that is equal to the decrease in potential energy per increment of crack extension. It is applicable both for linear and nonlinear elastic material as a measure of energy release rate. Eqs. (2.3) and (2.4) define the the energy release rate for linear material, however, these equations can be reused for nonlinear elastic material, except that G is replaced by J

$$J = -\frac{d\Pi}{da} = \frac{d}{da}(U - E_P) \tag{2.19}$$

For an arbitrary clockwise path Γ around the tip of a crack, as in 2D situation depicted

in Figure 2.7, the J integral is given as (see Appendix 3.3 in Ref. [7] for more details on steps between Eqs. (2.19) and (2.20))

$$J = \int_{\Gamma} \left(w n_1 - T_i \frac{\delta u_i}{\delta x_1} \right) ds \tag{2.20}$$

where

w = strain energy density

T_i = components of the traction vector

u_i = displacement vector components

ds = length increment along the contour Γ

The strain energy density is defined as

$$w = \int_0^{\epsilon_{ij}} \sigma_{ij} d\epsilon_{ij} \tag{2.21}$$

where σ_{ij} and ϵ_{ij} are the stress and strain tensors, respectively. The traction is a stress vector at a considered point on the contour, with its components defined in a following manner

$$T_i = \sigma_{ij} n_j \tag{2.22}$$

where n_j are the components of the unit vector normal to Γ.

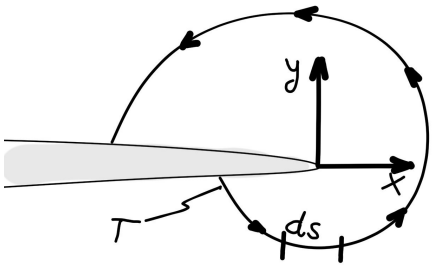

Figure 2.7: Elastic body in which an arbitrary contour is embedding the crack tip (figure redrawn from [7])

In most cases [60], this nonlinear elastic energy release rate can also be used as a measure of elasto-plastic energy release rate. Similiarly to G_C in LEFM, there is also a critical value J_C that J value must not exceed, otherwise crack propagation will ensue.

For a DCB problem, J integral defined by Eq. (2.20) can be derived into a simpler closed-form expression, as shown in [11]. Along contour Γ (line ABCDEG in Figure 2.8) both w and n_x are

not zero only for two straight lines AB and EG. For the case of Timoshenko beam theory, along this part of contour Γ the strain energy is only due to the shear stresses and strains, which are assumed constant and equal to F/A and $F/(\mu A_S)$, respectively, with $A_S = A \cdot k$. Therefore, the first term of integral (2.20) results in

$$\begin{aligned} &\int_\Gamma w n_x ds = \\ &= \int_A^B \frac{F^2}{2\mu A_S A} dy + \int_E^G \frac{F^2}{2\mu A_S A} dy = 2\int_0^{-h} \frac{F^2}{2\mu A_S A} dy = \frac{F^2}{B\mu A_S A} \int_0^{-h} B dy \\ &= -\frac{F^2}{B\mu A_S} \end{aligned} \tag{2.23}$$

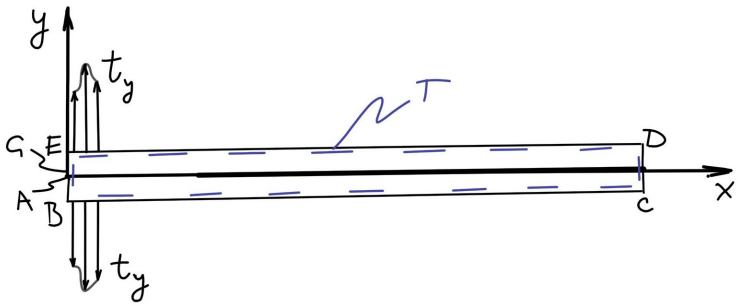

Figure 2.8: J integral contour Γ on a DCB (figure redrawn from [7])

To derive the second term, the reaction forces where displacements are prescribed are assumed as concentrated forces, meaning that the traction t_y can be considered applied on infinitesimal areas where $\partial u_y/\partial x$ is constant so it can be taken out of the integral in Eq. (2.20). The rotation of the top arm at the position of prescribed displacement can be written as

$$\frac{\partial u_y}{\partial x} = \theta - \frac{F}{\mu A_S} \tag{2.24}$$

while the rotation of the bottom arm at the position of prescribed displacement is defined as

$$\frac{\partial u_y}{\partial x} = -\theta + \frac{F}{\mu A_S} \tag{2.25}$$

Recall that $\partial u_y/\partial x$ can be taken out of the integral, and with t_y positive on the top and negative on the bottom, second term of integral (2.20) results in

$$\int_{\Gamma} t_y \frac{\partial u_y}{\partial x} ds = 2\left(\theta - \frac{F}{\mu A_S}\right)\frac{1}{B}\int_{\Gamma_{top}} t_y B ds = \frac{2}{B}\left(F\theta - \frac{F^2}{\mu A_S}\right) \tag{2.26}$$

where Γ_{top} is the infinitesimal area where the tractions are applied at the top arm.

Replacing Eqs. (2.23) and (2.26) into Eq. (2.20) leads to a solution for the DCB problem according to Timoshenko theory

$$J = \frac{F^2}{B}\left(\frac{1}{\mu A_S} - \frac{2\theta}{F}\right) \tag{2.27}$$

2.6 Data Reduction Schemes

Current thesis deals only with the case of DCB specimen depicted earlier in Figure 2.9 with typical geometry, boundary conditions and loading. Apart from formula 2.10 from the beginning of this chapter, there are numerous so-called data-reduction schemes used to quantify fracture toughness. ISO 25217:2009 [8] and ASTM-D3433-99 [9] are international standards for determining the fracture resistance of adhesive joints in mode I. In the first one [8], three different data-reduction schemes are given, namely: 'Simple beam theory' (SBT), 'Corrected beam theory' (CBT) and 'Experimental compliance method' (ECM). On the other hand, ASTM-D3433-99 contains only one data-reduction scheme that is equivalent to SBT. Therefore, in this thesis the focus is mostly on the data-reduction schemes given in ISO 25217:2009, while the assessment of their accuracy is given in the following chapter.

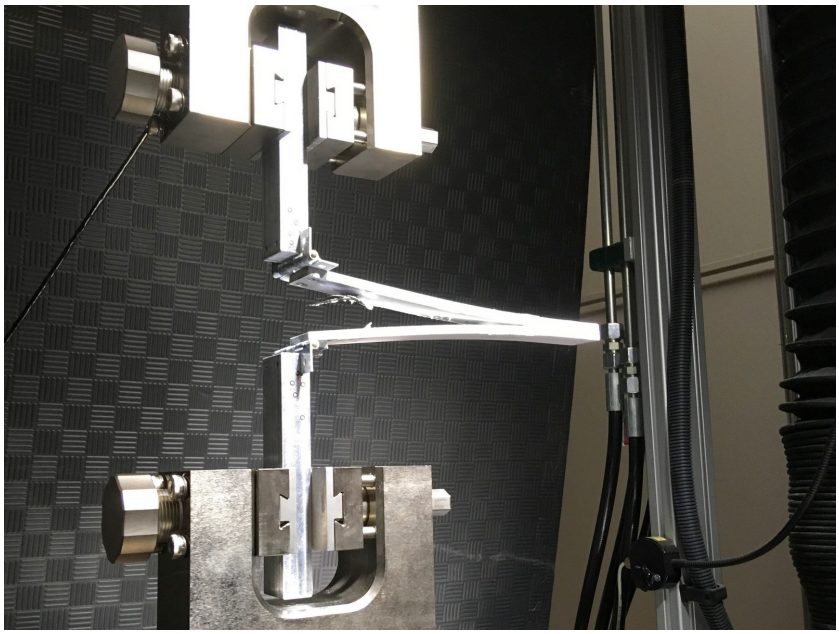

Figure 2.9: DCB test

Critical energy release rate given by SBT method is derived by inserting compliance given by Timoshenko beam theory in Irwin-Kies Equation (2.7) based on LEFM

$$G_{IC}^{SBT} = \frac{4P^2}{EB^2}\left(\frac{3a^2}{h^3} + \frac{1}{h}\right) \tag{2.28}$$

This method assumes that DCB adherends act as if they were Timoshenko beams clamped at the crack tip. This implies that the adhesive is infinitely stiff and perfectly brittle, which, of course, can be only a theoretical assumption and by no means a representative behaviour of a real adhesive. It is clear that no adhesive (even an infinitely stiff one) can prevent the rotation of the arms at the crack tip and in front of it if the shear deformability of the arm is taken into account [20]. Moreover, adhesive usually deforms before breaking, which means that at the crack tip, there will be some compliance before the crack starts to propagate. For these reasons it is clear that the measured values of displacement δ, force P and crack length a will never satisfy the assumptions made in the SBT data-reduction scheme. Accordingly, SBT will generally not give accurate predictions of adhesive's fracture resistance.

To adress the aforementioned inaccuracies of the SBT data-reduction scheme, the critical energy release rate can be calculated using the corrected beam theory (CBT) method based on the LEFM (Irwin-Kies Equation (2.7)) and Euler-Bernoulli beam theory. In this approach it is still assumed that the arms are clamped at the crack tip, but it also takes into account the plastic zone around the crack tip, similarly to what has been proposed by Irwin [75], i.e. by introducing the effective crack length [78]. The CBT expression for the fracture resistance, expressed as the critical energy release rate, reads,

$$G_{IC}^{CBT} = \frac{3P\delta}{2B(a + |\Delta|)} \tag{2.29}$$

where the crack length correction Δ represents the x-intercept of the linear fit of the $(\delta/P)^{1/3} - a$ plot (see Figure 2.10 or [8] for more details).

Alternatively, the third method suggested by ISO 25217:2009 standard, called enhanced compliance method (ECM), also includes an experimental correction of the measured compliance. This method corrects the exponent in the formula (2.30) ([22]). The new value of the exponent is obtained experimentally by a linear fit of the logarithm scale plot of compliance versus crack length, i.e. $\log C - \log a$. The slope of the linear fit of the data points is the corrected exponent n. Finally, the critical energy release rate given by ECM equals

$$G_{IC}^{ECM} = \frac{nP\delta}{2Ba} \tag{2.30}$$

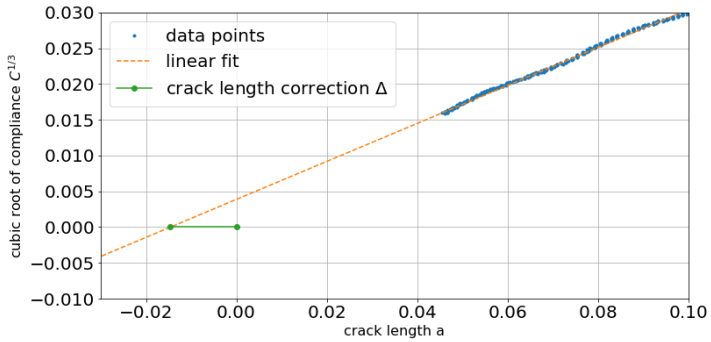

Figure 2.10: CBT correction

Another method, which is not a part of any standard, is the recently developed enhanced simple beam theory (ESBT) method [20]. It is based on the concept of the equivalent crack length, which for Timoshenko beam theory is defined as

$$a_{eq} = \sqrt[3]{\left(\frac{1}{\sqrt{\alpha}}\right)^3 + \frac{3EI\delta}{2P} - \frac{1}{\sqrt{\alpha}}} \tag{2.31}$$

where $\alpha = \mu A_s/EI$, μ is the shear modulus, $A_s = A \cdot k_s$, A is the cross-sectional area of a single DCB arm, $k_s = 5/6$ is the shear correction factor, E is the Young's modulus of substrates and I is the moment of inertia of a single DCB arm. Note that such a definition of a_{eq} accounts for cross-sectional rotations of the DCB arms at the crack tip and ahead of it due to shear strains (for details see [20]). Fracture resistance, expressed as the critical energy release rate, can be then computed as:

$$G_{IC}^{ESBT} = \frac{P^2}{b}\left(\frac{a_{eq}^2}{EI} + \frac{1 + 2a_{eq}\sqrt{\alpha}}{\mu A_s}\right) \tag{2.32}$$

Apart from the methods based on the critical energy release rate (G_C), fracture resistance of the adhesive can be computed by means of the J integral [33]. Neglecting the contribution of shear strain in Eq. (2.27) by assuming a high value of μA_S leads to a slightly simpler J integral definition

$$G_{IC}^{J-INT} = \frac{P \cdot \theta}{B} \tag{2.33}$$

where θ is the cross-sectional rotation of the substrates load-line. In the present work, θ is

measured by means of DIC (explained in detail in the next chapter).

Chapter 3

Experiments

This chapter explains the experimental setup used for this thesis. In experiments described in next four sections [79], the DCB substrates are made of aluminium 6060 alloy (E=70 GPa, ν=1/3), while the adhesive used is SikaPower® 4720. Aluminium grade was increased to 7075 for experiments in the last section (3.5) due to problems with substrate plastification during bending. First, experimental methods and techniques used are explained, which is followed by an extensive study on the influence of different loading arrangements on the test results. After applying the data-reduction schemes presented in the previous chapter, the obtained R-curves along with traction separation laws are presented in the following two sections. At the end of this chapter, the experimental setup used for plate-like specimens is presented along with a novel technique of identifying fracture toughness regardless of specimen width.

3.1 Experimental Methods

The DCB specimens (Figure 2.3) were tested in equal conditions using the tensile testing machine Zwick Z 600E with force capacity up to 10 kN which is twice the required amount in present case (evident from the next Section).

Before bonding, the substrate surface was sanded down with a 180-grit sandpaper and then cleaned with pure acetone. A uniform thickness and distribution of the adhesive on each substrate was accomplished by means of guide rails for the putty knife. After the adhesive was applied on each substrate, the specimens were assembled and loaded with weights to ensure the removal of the excess adhesive. A 0.5 mm thick fishing lines were placed between the substrates at the edges of the bonding area to control the final thickness of the adhesive layer [80] as a large

variance in thickness may affect the measured material properties of the adhesive [81]. The initial crack (pre-crack) was formed by placing an aluminium foil along the first 50 mm of the substrate. According to the manufacturer, full bearing capability of the adhesive joint is reached after curing the adhesive for 2 days at room temperature, but in this particular case, specimens were cured during the whole week. After curing, all excessive adhesive was removed from the specimen edges.

In this thesis, instead of measuring the crack length by visual inspection as suggested in [8], the experiments were recorded with optical measuring equipment (cameras) and processed by digital image correlation (DIC). Digital image correlation uses an optical measurement technique that traces displacement of a body. It is used mainly in experimental mechanics but it also finds its use in research and research and development departments of numerous industries for its simplicity over other alternatives.

3.1.1 Digital Image Correlation

If a single camera is used, plane displacements can be tracked in two dimensions orthogonal to the camera ray, therefore, this technique is sometimes called 2D DIC. By adding another camera, displacements can be measured in all three directions, which is why this technique is sometimes called 3D DIC. Cameras capture raster graphics where a single pixel is represented only by its light intensity (brightness) on a scale from 0 to 255, in case of 8-bit cameras. By knowing the position of the two cameras, one can triangulate the spatial position of each pixel, i.e. material point. This concept is usually implemented by painting or spraying the surface of a mechanical body with a stohastic speckle pattern prior to recording. This part of the specimen preparation is paramount because, in case of a poor pattern quality, there is a risk that the system will not be able to recognise any movement or deformation of the body. Quality of the speckle pattern depends on several factors such as camera settings, calibration of cameras, pattern paint reflectiveness, as well as randomness of the pattern brightness and frequency of the recording [82]. Pixel brightness of a speckle pattern can then be interpolated by a surface fit across a square area of image of predetermined size. These areas of image are also called facets. Pixels brightness of a single facet is interpolated by a surface spline.

For a mechanical body to be tracked, one must find the correlation between the deformed and undeformed facet (deformation mapping) across two frames [83]. This is done iteratively by maximising the so-called correlation coefficient. Finally, one can determine the displacement

field and, consequently, obtain deformation, speed and acceleration of a mechanical body.

The prepared specimens were sprayed with the anti-reflective white paint, and then speckled with dots of black paint to create a stochastic pattern for the DIC tracking. First the surface was coated with a layer of anti-reflective white spray and then, by applying a very slight pressure on the valve of black spray can, the black spray patches were speckled randomly across the surface. Different sizes of black speckles were tested prior to final application. Useful guidelines, such as speckle pattern creation recommendations, are given in [82]. Actual pattern feature size was ultimately around 4 px which is in line with recommended optimum size [82] of 3-5 px. Furthermore, key DIC processing parameters are subset size (or facet size) and point distance (or step size). Recommended subset size is 21 x 21 pixels with a minimum of three transitions between black and white pattern features in all directions. The second parameter is 18 px facet point distance, which satisfies the recommended [82] 1/3-1/2 amount of subset overlap.

8-bit stereo greyscale 4 MP (2358x1728) resolution cameras Titanar 20 mm paired with GOM Aramis V8 software were used to extract the full-field surface displacements. For the experiments described in the next few sections (starting with Section 3.2), relatively small measuring volume of 150 x 110 x 110 mm was used in order to gain more precision for the detection of the crack-tip position. This was sufficient to capture only the first 75 mm of crack length propagation, which means that the remaining part (approximately 130 mm) was out of frame.

With DIC calibration object of 90 x 72 mm at a desired measuring distance, the focus was set up manually at maximum aperture setting of F 2.8 with the intention of fine-tuning the focus within a smallest margin of error possible. The aperture was then increased for two F-stops in order to achieve the optimal aperture of F 5.6 (sweet spot) i.e., sharpest images possible. Choosing a larger aperture (smaller F-number) leads to quality degradation caused by aberration, while a smaller aperture (larger F-number) causes problems with diffraction. The depth of field at F 5.6 aperture was large enough to sharply capture the details across the region of interest. Exposure time for this setup was found to be below 0.01 seconds.

The specimens were pulled apart in the tensile testing machine by a crosshead rate of 2 mm/min, which corresponds to 0.0002 mm motion during the exposure time of 0.007 s. Static images of a prepared specimen were acquired with the measured displacement noise floor of about 0.00025 mm, which is depicted in Figure 3.1. Because the test piece motion was slightly smaller than the noise floor, the conservative threshold [82] was satisfied and, consequently, the measurement uncertainty from motion blur was avoided. Pixel size for the DIC setup used in

sections 3.2-3.4 was 150 mm / 2358 px = 0.06 mm. Considering that the theoretical uncertainty of the DIC method is around 0.01 pixel [84], the current setup allowed to obtain the submicron precision in an ideal scenario.

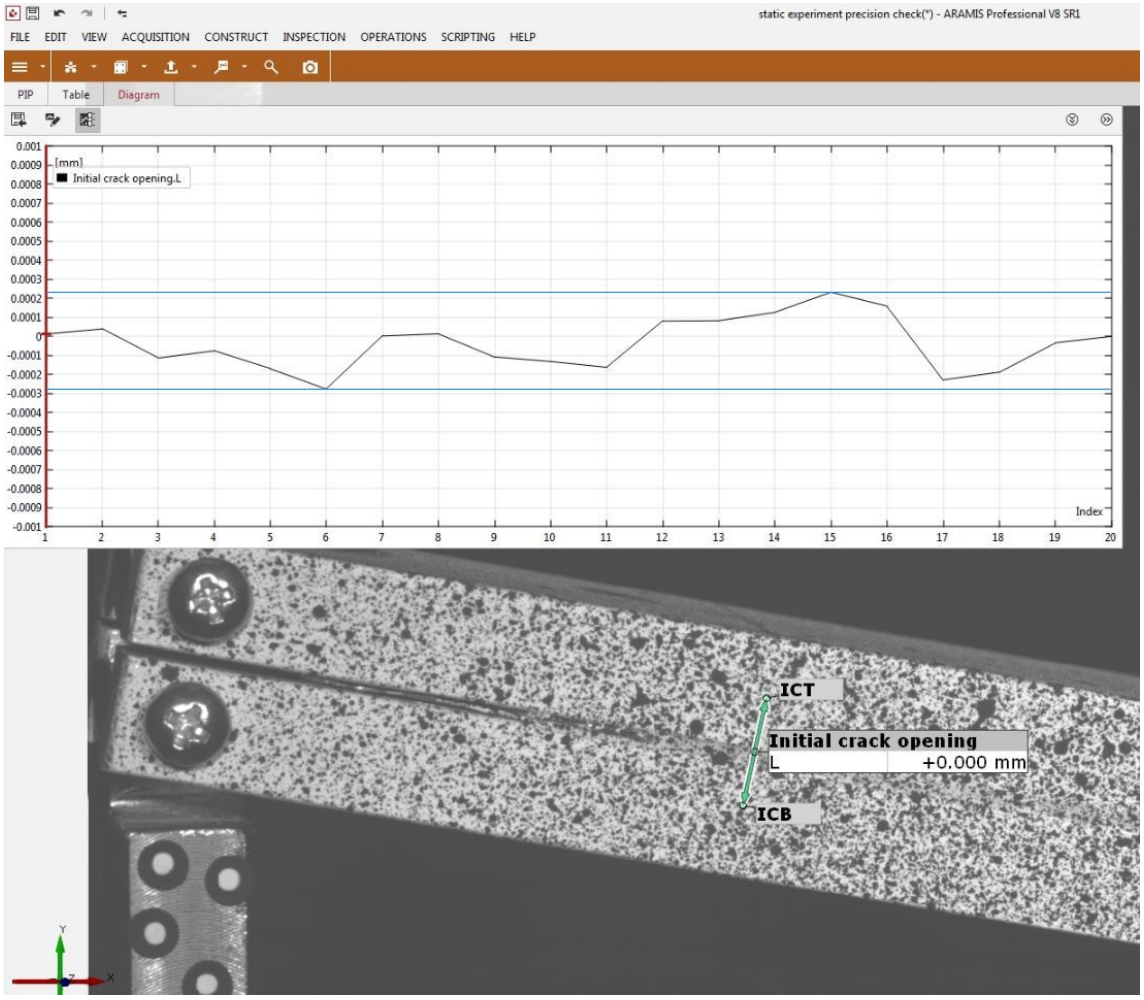

Figure 3.1: Static experiment for measuring the displacement noise at the position of initial crack opening, note that the graph y-axis limits are from -1 to +1 micron, while the noise floor values are marked by blue colour at the positions of the maximum displacement measurements

3.1.2 Measurements of the Key Quantities

Fracture resistance along the interface was calculated from the measured data, i.e., load-line displacement δ, applied force P, crack length a and cross-sectional rotation at the load-line θ. The applied force was measured directly from the tensile-testing machine (TTM), while the crosshead displacement was measured either from the TTM or using DIC as the relative displacement of measuring points on the upper and bottom rigid block connected to TTM grips (because the grips were not captured in the frame, as it can be seen in Figure 3.2). Having independent measurements of the crosshead displacement was essential for synchronising the

data acquired from the TTM with those obtained from DIC, which was performed by matching displacements in the initial phase (during the take up of play). In particular, 0.1 mm crosshead displacement measured by TTM and DIC matches within 0.001 mm, i.e., error between these measurements is below 1 percent.

In addition, the load-line displacement (i.e., the displacement at the position where the load is applied on the specimen) was measured using DIC as the relative displacement of measuring points located directly on the DCB arm. Therefore, it will be assumed that, in general, the crosshead displacement and the load-line opening are different.

Right-hand side of Figure 3.2 illustrates the following DIC measurements: crosshead displacement δ_{TTM} (also acquired from the TTM), load-line opening displacement δ_{DIC} at the DCB arms, relative rotation of the arms at the specimen's free end θ (for each arm the rotation of the reference line is measured), separation at the initial crack tip δ_{INIT} and the separation along the interface, which is computed as the relative deflection δ_{rel}, i.e., the difference of the deflection lines (blue lines in Figure 3.2 b), d) and f)) for each arm. The layer deflection lines were constructed at the initial stage as straight splines with nodes (knots) at 1 mm spacing. Their deformed shape in later stages is automatically determined by the software using the definition from the initial stage. Note that if the DCB arms are assumed to be transversally rigid, the displacements at the glued edges of the arms are equal to the corresponding displacements at the reference lines.

The crack length was computed automatically from the DIC measurements as a location at which the interface separation reaches its critical value δ_C corresponding to a complete failure of the material. By analysing the recorded frames, it was found that the interface separation corresponding to a visually noticeable crack is 0.2 mm. Visually noticeable crack tip was identified from a sudden decrease in pixel intensity at one of approximately 8 pixels across the thickness of the interface. However, after identifying the complete shape of the traction-separation law of the interface, which is explained in detail in Section 3.4, it was concluded that after the separation of approximately 0.08 mm, the tractions transmitted at the interface become negligible, implying that the material of the interface is fully damaged. This result was independent of the loading arrangement. It was also confirmed that the stage at which the separation at the initial crack tip reaches 0.08 mm is located slightly after the peak of the load-displacement diagram, which is in accordance with the analytical solution for a DCB presented in [85]. Therefore, for the purpose of automatic identification of the crack tip position using the DIC, $\delta_C = 0.08$ mm was used.

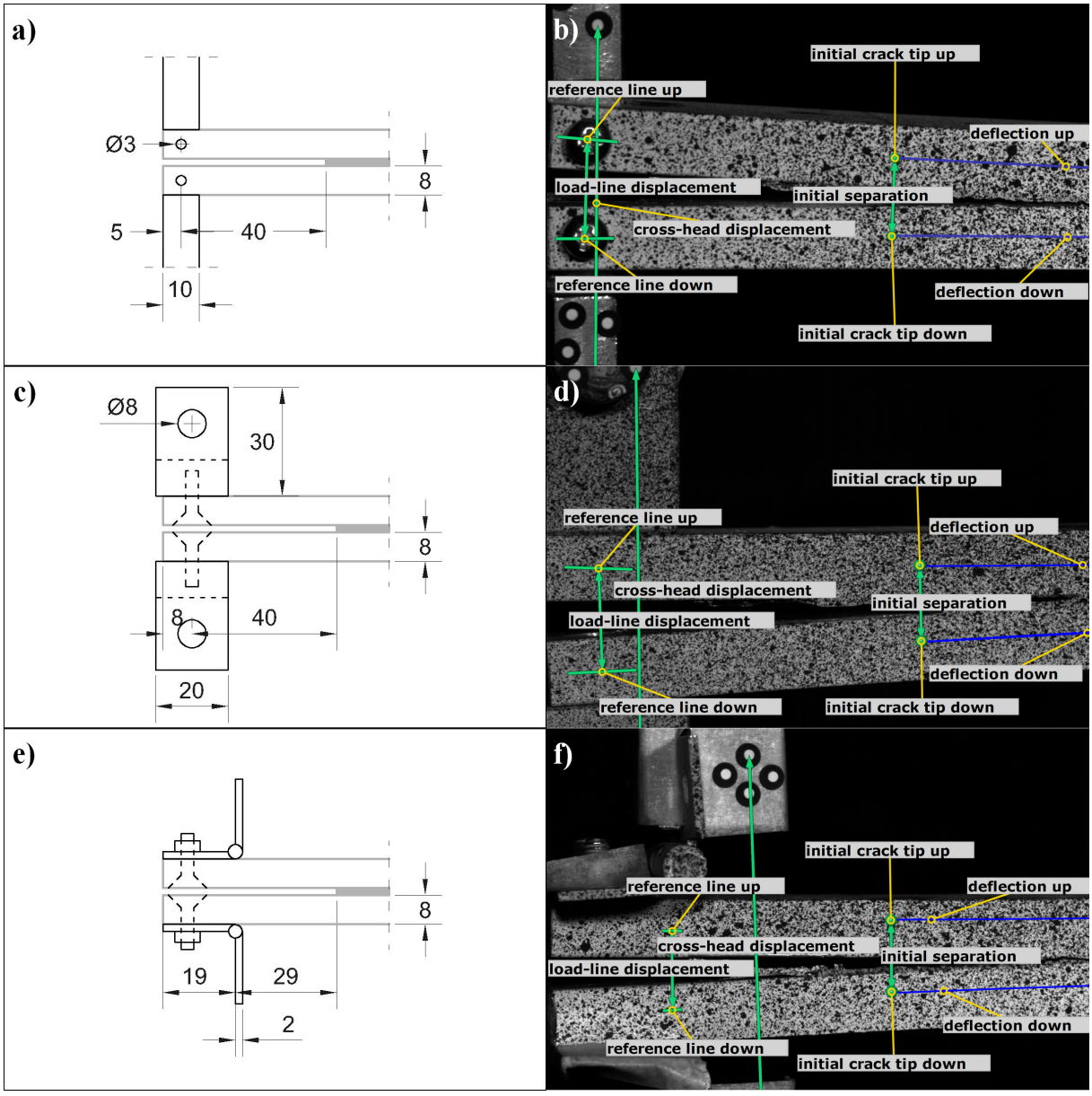

Figure 3.2: Schemes of the loading arrangements used in the analysis (left-hand side) with the corresponding DIC measurements (right-hand side), namely: a) - b) loading pins, c) - d) loading blocks and e) – f) piano hinges

Cross-sectional rotation of each arm at the load line was determined from the DIC data by assuming that it is equal to the rotation of the reference line, which is marked in Figures 3.2.b), d) and f). Because the rotations of the top and bottom arm do not perfectly coincide (experiments are not perfectly symmetric), θ is computed as a mean cross-sectional rotation, i.e., half of the relative rotation between the top and bottom arm.

3.2 Load Arrangement Analysis

Two equal aluminium substrates (E=70 GPa, ν=1/3) were glued together along the interface, with the exception of an initial notch of length a_0. Dimensions of the specimens, according to Figure 2.3 presented previously, are L = 250 mm, h = 8 mm, B = 30 mm and t = 0.5 mm, while the initial crack length a_0 is equal to 29 or 40 mm, depending on the loading arrangement. Actual thickness of the adhesive layer ranged between 0.47 mm and 0.62 mm, with the mean thickness equal to 0.53 mm and the standard deviation of 0.05 mm. In total, 9 specimens were produced, i.e., 3 specimens for each of the 3 loading arrangements considered.

Three different loading arrangements for DCB tests were used in the experimental programme, namely: loading holes/pins, loading blocks and piano hinges. Three specimens were tested for each loading arrangements so that abbreviations Pi, Bi and Hi were introduced for pins, blocks, and hinges, respectively, where index i=1,2,3 is the specimen number. According to [8], piano hinges are an alternative to loading blocks, while for metallic substrates, loading holes can be used as an alternative loading arrangement. In Figure 3.2, all three types of loading arrangements are shown schematically (left-hand side) together with the corresponding DIC measurements (right-hand side).

Loading holes for specimens P1-P3 were drilled through the specimen width and a pin of diameter 3 mm was inserted to introduce the load from TTM via a block that was held in the grips (see Figure 3.2.a) and b)). The distance from the point of application of the load to the crack tip represents the crack length, while the load-line opening is equal or slightly smaller than the crosshead displacement.

Loading blocks are usually glued on the specimens, but in case of metallic substrates they can be attached by means of screws [86]. For specimens B1-B3, each steel loading block was screwed on the substrate and connected with a steel pin of diameter 8 mm to another block that was held in the grips of the TTM (see Figure 3.2.c) and d)). At the initial stage of the

experiment, it can be assumed that the crosshead displacement of the tensile testing machine (TTM) is equal to the load-line displacement on the specimen. However, as the arms bend, the blocks rotate creating a difference between the load-line displacement and the crosshead displacement. For the loading-block arrangement, the crosshead displacement was measured at the edge of the screw head (Figure 3.2.d). By comparing these measurements with those from the TTM, it was confirmed that the rotation of the screw head during experiments was negligible and has therefore no influence on the results. Moreover, in the case of glued blocks it is very questionable where exactly the point in which the load is applied on the specimen is. Usually, it is assumed to be in the middle of the block [8], which is a reasonable assumption for blocks connected by means of screws (as it has been done in this study and shown in Figure 3.2.c) and d)). The point of application of the load is essential for defining the crack length.

In ISO 25217:2009 standard [8], the stiffening effect due to end blocks is considered by dividing the load-line displacement by a factor N dependent on block dimensions and current values of the crosshead displacement and crack length (which essentially defines the rotation of the block) [24,78]. Because $N<1$, this results in an increase of the fracture resistance with respect to the uncorrected value (with $N=1$). Since this effect is negligible in case of small rotations of blocks, Williams [78] derived the expression for N considering large displacements of the arms and (later in the derivation) assuming small rotations. On the other hand, Škec and Alfano [86] demonstrated that, for small displacements and rotations, the rotation of the block creates an additional concentrated moment on each DCB arm, which in turn reduces the fracture resistance.

The piano hinges are also typically glued on the specimens, but in case of metallic substrates they can be attached by means of screws (as it has been done in this study and shown in Figure 3.2.e) and f)). Piano hinges were screwed on the substrates of specimens H1-H3 and connected to a block that was held in the grips of the TTM (see Figure 3.2.e) and f)). In this work, commercial-grade quality piano hinges were used. The load-line is assumed to pass through the pins connecting the two parts of each piano-hinge [8], which means that a vertical force from the TTM is transferred from the pin directly on the specimen throughout the experiment. Therefore, unlike loading blocks, no special corrections are needed to account for the piano hinges. For loading arrangement with piano hinges, the aforementioned load line, connecting the pins of the hinges at both sides of the specimen (as defined in [8]), is shifted horizontally with respect to the vertical line connecting the TTM grips. Given that the crack length is measured as a distance between the load-line and the crack tip, the arrangement with piano hinges has

a smaller initial crack length $a_0 = 29$ mm, compared to other arrangements where $a_0 = 40$ mm. Nevertheless, in ISO 25217:2009 standard [8], corrections of the crack length that take into account large displacements (but at the same time assume that the rotations are small) can be used for both loading blocks and piano hinges.

Consequently, it is reasonable to deduce that different loading arrangements should not affect the calculated fracture resistance if appropriate corrections are applied. In fact, the aim of this investigation is to test this hypothesis. Vina et al. [87] found that geometrical non-linearities of loading-block arrangements lead to an apparently higher fracture resistance. Aalami and Chakherlou [88] have recently studied the influence of T-stress for different loading arrangements. They concluded that the higher stress triaxiality of loading-block arrangements leads to a higher fracture resistance.

The previous discussion is based on the assumption that the DCB specimen is connected to the TTM by means of an infinitely stiff loading system. However, due to effects such as take-up of play and machine compliance (or system compliance), a relatively small part of the cross-head displacement of the TTM will not be transferred directly to the specimen. The results from the inter-laboratory round-robin presented in [80] showed that neglecting the effects of the system compliance can lead to non-negligible differences in the computed fracture resistance of adhesive joints of steel substrates. Motivated by these findings, a protocol for correcting the cross-head displacement measured from the TTM by taking into account the system compliance became a part of DCB standards BS 7991: 2001 and later BS ISO 25217: 2009 [8]. The system compliance is determined via a tensile test of a rigid calibration specimen (or specimens [89]) of known compliance. A linear fit of the load-displacement data of the calibrations specimen's tensile test gives a constant system compliance. Finally, the measured cross-head displacement from the TTM is corrected by subtracting from it the system compliance multiplied by the corresponding value of the applied load.

Although such a procedure undoubtedly increases the accuracy of the computed fracture resistance, it also has its drawbacks. In particular, it does not account for non-linear machine compliance [90], as well as linear (elastic) and non-linear (plastic) deformations of the some parts of the loading arrangement, such as pins, screws and hinges.

The system-compliance correction can be omitted if an extensometer attached to the specimen [8] or DIC is used to measure the opening displacement. As confirmed by the present study, such a procedure is more reliable than the tensile test of the calibration specimen. It is worth mentioning

the system-compliance correction does not exist in ASTM D3433 – 99 (2020) [9] standard for bonded metal joints, while in ASTM D 5528 – 01 (Reapproved 2007) [10] for unidirectional fibre-reinforced polymer matrix composites it is stated that an external gauge or transducer shall be attached to the specimen if the deformation of the TTM with the specimen grips attached is greater than 2 percent of the opening displacement of the test specimen. However, a procedure from which this information should be obtained is not described.

It has been found in this study that the tested properties of adhesive depend not (primarily) on the loading arrangement, but on the position where the load-line displacement is measured. It has been shown that the difference between the crosshead displacement measured on the TTM and the load-line displacement measured directly on the specimen using DIC is strongly dependent on the loading arrangement. This difference is for all loading arrangements also due to elastic or plastic deformation of parts (pins, blocks, hinges, screws) that connect the TTM and tested specimens, and possibly due to clearance (gap) between those parts. Note that this difference cannot be accurately determined using the standard procedure for determining the machine compliance [8].

Examination of all specimens after failure revealed a very small amount of interfacial failure which was noticed only outside the DIC frame and only in specimen P3, thus not affecting the presented analyses. In all other specimens the failure was perfectly cohesive, which confirms that the method used to prepare the specimens was successful. Specimens P2, P3 and B3 had some adhesive over the edge of aluminium foil boundary, but this had no apparent influence on the measured load-displacement curves (shown in the following section). Furthermore, visual inspection of the specimens after failure showed no signs of permanent plastic deformation of the arms that might have occurred during loading.

3.2.1 Acquired Load-Displacement Data

In order to accurately assess the adhesive's fracture resistance, it is essential to have a reliable load-displacement data. While the applied load measured by the TTM is generally very accurate and can be readily used in closed-form expressions for the fracture resistance (either G_{IC} or J_{INT}), obtaining the exact value of the load-line displacement is not straightforward. This is because the relative displacement of the grips of the TTM is not directly and completely transferred to the specimen, which is why in general the actual load-line displacement is smaller than the cross-head displacement of the TTM. The main reasons for this are (a) the clearance

between the assembled parts, (b) machine compliance and (c) deformation of parts of the loading arrangement (pins, blocks, piano hinges).

At the beginning of test, the specimen is pre-loaded, which however is not sufficient to fully eliminate the clearance between the specimen, the loading arrangement and the TTM, i.e. the so-called take-up of play effect [80]. In fact, all aforementioned standards except for [9] suggest that the initial deviations due to take-up of play should be removed from the load-displacement data (for more details about this procedure see [80]). In the present work, this correction has been performed, as discussed later in more detail.

The correction of the load-displacement data that takes into account the machine compliance is a part (annex) of standards [8,10]. In this work, this correction has not been performed because the actual load-line displacement has been measured directly from the specimen using the DIC. Note that standards [8, 10] suggest using extensometer for that purpose. Nevertheless, when measuring the load-line displacement directly from the specimen, one is accounting not only for the machine compliance, but also for elastic (and possibly plastic) deformations of the parts of the loading arrangement (pins, blocks, piano hinges). Thus, such a procedure will certainly yield more accurate results than performing only the standard machine-compliance correction.

Force-displacement graphs measured by the TTM (δ_{TTM} is used) are given in Figure 3.3, while the force-displacement graphs from DIC measurements (δ_{DIC} is used) are given in Figure 3.4. In Figure 3.3.d) and Figure 3.4.d), the average plots of the three specimens for each of the considered loading arrangements are compared. Note that the loading arrangement with piano hinges has smaller initial crack length than the other two arrangements (see Figure 3.2), which results in higher values of the peak force. Furthermore, it can be noticed that the average curve for the piano hinges in Figure 3.3.c) has an apparent "elbow" of the averaged curve near the onset of crack propagation, which is not the case when the load-line displacement δ_{DIC} is used (see Figure 3.4.c)).

It should be emphasised that load-displacement plots in Figure 3.3 have been corrected by excluding the initial deviations due to take-up of play from the measured cross-head displacement. This is achieved by shifting the plots horizontally so that the liner part of the curve is aligned with a straight line passing through the origin of the coordinate system following the automatic procedure described in [41], which can be also done manually, as proposed earlier in standard BS 25217:2009 [8]. Machine compliance has not been used to additionally correct the cross-head displacement, because the cross-head displacement δ_{TTM} measured from the TTM and

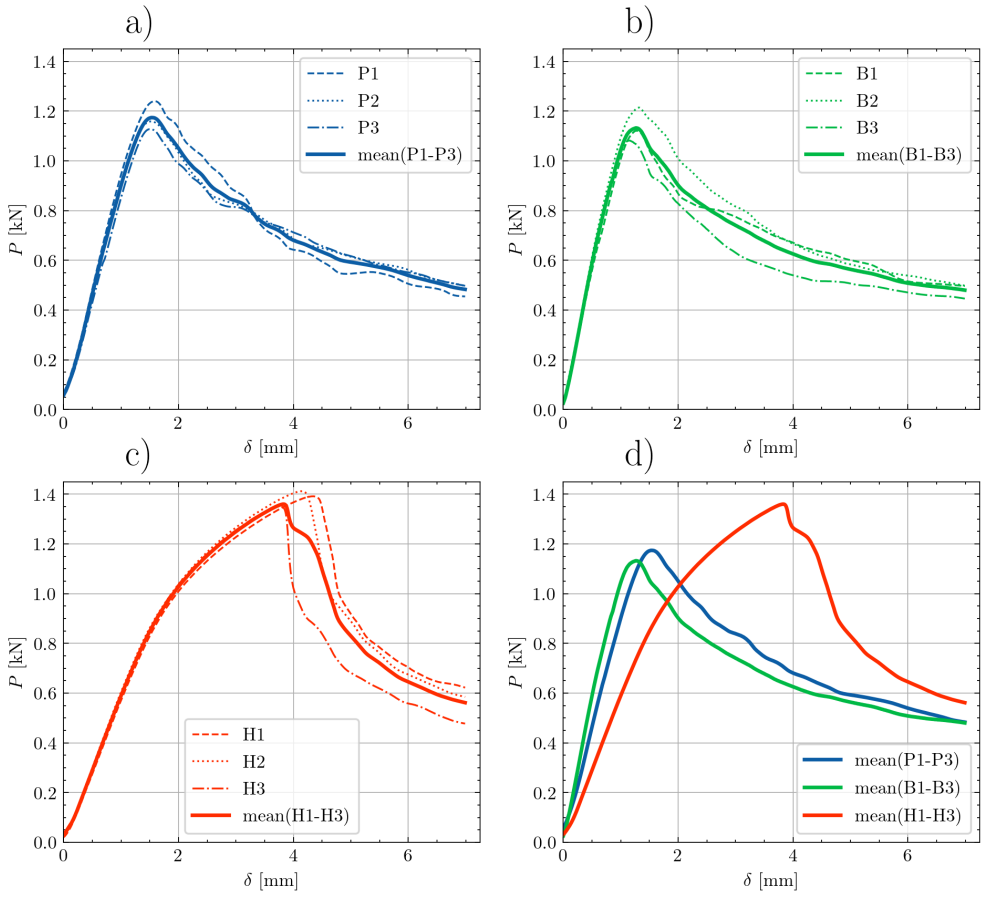

Figure 3.3: Force-displacement curves from the TTM measurements: a) loading pins, b) loading blocks, c) piano hinges and d) comparisson between loading arrangements

that measured by the DIC (see Figure 3.2) for the purpose of synchronisation yielded negligible differences of the compliance in the linear-elastic range.

Nevertheless, as it can be seen by comparing Figures 3.3.d) and 3.4.d), excluding the initial deviations due to take-up of play (and machine-compliance) from the load-displacement data is not sufficient to account for the discrepancy of the DIC and TTM measurements. It was noticed that the load-line displacement measured from the TTM is greater than that measured using the DIC, which can be attributed to the elastic deformations of the blocks used to connect the specimens to the TTM grips, but also to elastic and plastic deformations of the weakest elements of some connection systems.

Moreover, by subtracting the plots from Figure 3.4 from the corresponding plots in Figure 3.3, plots with the difference between the crosshead displacement and load-line opening ($\delta_{TTM} - \delta_{DIC}$) on the horizontal axis can be obtained, which is shown in Figure 3.5. It can be noticed that the difference $\delta_{TTM} - \delta_{DIC}$ is dependent on the load (i.e., it increases as the load increases and vice versa), which confirms that the deformation of the loading arrangement is partially elastic.

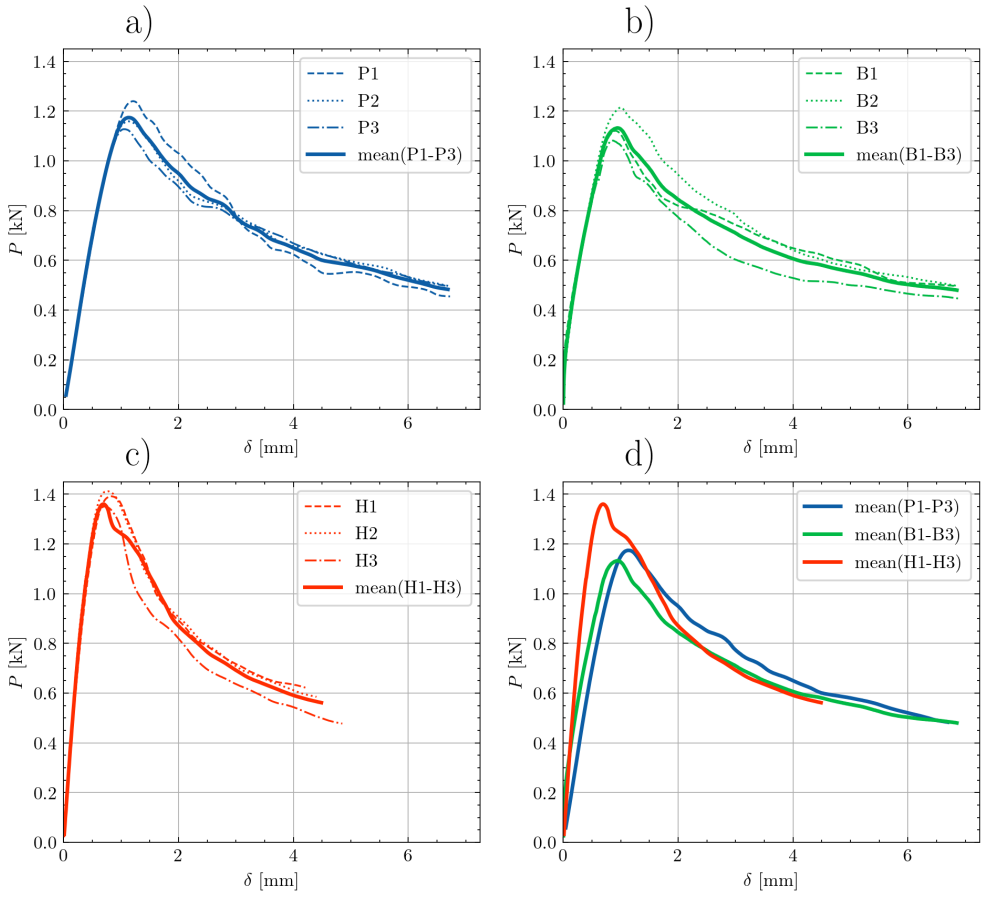

Figure 3.4: Force-displacement curves from the DIC measurements: a) loading pins, b) loading blocks, c) piano hinges and d) comparisson between loading arrangements

However, the increasing and the decreasing part of the curve do not coincide for any of the considered loading arrangements.

In particular, Figure 3.5.a) shows that for the same value of the load the difference $\delta_{TTM} - \delta_{DIC}$ for loading pins is greater after the peak force than it was before. This implies that, between the specimen and the grips of the TTM, a certain amount of plastic deformation has occurred. In fact, visual inspection of the pins after the experiments confirmed relatively small permanent plastic deformations.

Results for loading blocks shown in Figure 3.5.b) indicate an opposite behaviour – the difference $\delta_{TTM} - \delta_{DIC}$ decreases after the peak force. The stiffness of the loading arrangement cannot increase during the experiment (it can only decrease).The more the block rotates, the less the difference, which implies that the difference will reduce as the crack propagates (longer crack lengths give greater rotations at the load line). It can be noticed that $\delta_{TTM} - \delta_{DIC}$ is not reduced immediately after the peak load because, even in the case of loading blocks, there is obviously some small amount of plastic deformation taking place in the loading arrangement.

The plates of the piano hinges attached to the substrates, shown in Figure 3.2.e), deform during the experiment, and, after the load is removed, remain plastically deformed, which is shown in Figure 3.5.c). A comparison of the three loading arrangements shown in Figure 3.5.d) demonstrates that the magnitude of plastic deformation of piano hinges significantly exceeds that of the pins and loading blocks.

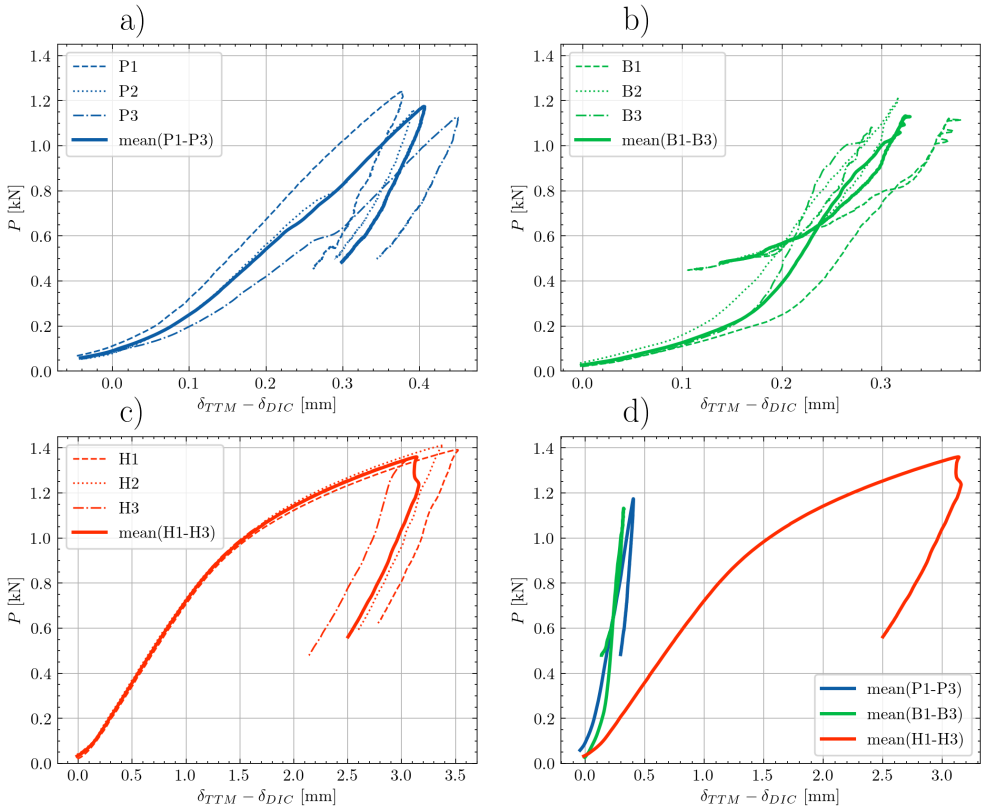

Figure 3.5: Difference between TTM and DIC measurements: a) loading pins, b) loading blocks, c) piano hinges and d) comparisson between loading arrangements

In order to explain the difference in the TTM and DIC measurements depicted in Figure 3.5, a preliminary experimental investigation with rigidly connected aluminium plates, instead of DCB specimens, was performed for each loading arrangement (pins, blocks, piano hinges). By loading the rigid specimen up to the peak force from the previous DCB tests, cross-head displacement δ_{RIGID} was obtained. Therefore, $\delta_{TTM} - \delta_{RIGID}$ can be used as an estimate of the actual load-line displacement δ_{DIC}, without the use of the DIC or the extensometry equipment. It was shown that for loading pins and piano hinges the rigid-specimen correction overestimated the actual compliance of the loading arrangement, so that $\delta_{TTM} - \delta_{RIGID} < \delta_{DIC}$. However, this correction noticeably improved the accuracy of computed values of the fracture resistance, especially for the case of loading blocks, where $\delta_{TTM} - \delta_{RIGID} \approx \delta_{DIC}$. In fact, this procedure

could be used to assess the fracture resistance of an adhesive more accurately in cases where the DIC (or other measuring tools) are not available or desirable. Note that this procedure is not equivalent to that described in Annex A of standard BS 25217:2009 [8] because in addition to the machine compliance, it also takes into account the compliance (deformability) of the parts of the loading arrangement.

3.3 R-curves

In this Section, the change of fracture resistance during crack propagation is presented graphically in form of resistance curves (R-curves) [77] for all specimens to determine to what extent different loading arrangements can affect the computed fracture resistance. Three different data-reduction schemes are considered, namely the Enhanced Simple Beam Theory (ESBT) [20], Corrected Beam Theory (CBT) [8] and the J integral [27, 36]. In the first part, each of them is briefly presented, which is followed by a comparison of the three methods using the average data for each loading arrangement. Scatter of the results is analysed by comparing R-curves for all 9 specimens and, finally, the effect of the difference $\delta_{TTM} - \delta_{DIC}$ on the results is assessed. In the following expressions δ is used for the displacement that can be either a crosshead displacement δ_{TTM} or a load-line displacement δ_{DIC}.

In all data-reduction schemes used in standards [8,9], besides the load-displacement measurements, the measurement of the crack length is also required for the calculation of the fracture resistance. However, as shown in [20], if we look into the standard [8], only the Corrected Beam Theory (CBT) can accurately predict the actual fracture resistance for quasi-brittle interfaces and has been therefore used in the present analysis. On the other hand, in [20] it has been demonstrated that the ESBT method, in which the crack-length measurement is not required, can be even more accurate than the CBT method. This is an important practical advantage of the relatively new ESBT method with respect to all other methods from standards because no special equipment is required for measuring the crack length. It should be noticed that in all methods, except for the J integral, measuring δ from the TTM or directly from the specimen will affect the results of the computed fracture resistance, as it is shown later in the present Section.

In standards, corrections for loading arrangement exists only for the stiffening effect of loading blocks [8]. It is suggested to divide the computed values of the fracture resistance by [25, 78]

$$N = 1 - \left(\frac{l_2}{a}\right)^3 - \frac{9}{8}\left[1 - \left(\frac{l_2}{a}\right)^2\right]\frac{l_1\delta}{a^2} - \frac{9}{35}\left(\frac{\delta}{a}\right)^2 \tag{3.1}$$

where l_1 and l_2 are the distances from the centre of the horizontal hole in the block to the reference axis of the adjacent arm and the right-hand edge of the block, respectively. According to Figure 3.2, $l_1 = 26mm$ and $l_2 = 9mm$.

For the J-integral, stiffening effect of loading blocks has been taken into account by adding an additional member $M^2/(bEI)$ to Equation 2.33, where $M = Pl_1\theta$ is the eccentricity moment [15]. However, in the course of this study it has been noticed that this contribution may be disregarded here as insignificant. Moreover, large-displacement corrections proposed in [8] were not considered in the present paper because, as it can be seen in Figure 3.4 the displacements were relatively small compared to specimen dimensions (and correction from [8] would influence the results for less than 1 %).

Note that modulus of elasticity E was back-calculated from experimental data by rearranging the expression for compliance [80],

$$C = \frac{\delta}{P} = \frac{(2(a + |\Delta|))^3}{3EI} \tag{3.2}$$

where $|\Delta|$ has been previously determined in the CBT data-reduction scheme. The obtained value of E was in the expected range for aluminium, i.e., slightly over 70 GPa or, specifically, 71 GPa for loading pins, 76 GPa for loading blocks and 72 GPa for piano hinges loading arrangement.

Average R-curves during crack propagation obtained using different data-reduction schemes (ESBT, CBT and J integral) are compared in Figure 3.6. They were obtained by averaging the individual R-curves for each loading arrangement with respect to the crack length, as it is shown later in Figure 3.7.a)-c) for the ESBT method. Note that for ESBT and CBT R-curves shown in Figures 3.6 and 3.7, $\delta = \delta_{DIC}$ was used.

Generally, the agreement between different methods is excellent. Considered data-reduction schemes yield results within 1 percent difference, which is shown on the right-hand side of Figure 3.6, where normalised values with respect to the fracture resistance given by the J integral are given, as also done in [11, 91]. A detailed analysis of the computed values of the fracture resistance for each loading arrangement are given in the following subsection.

In the following analyses, only the ESBT data-reduction scheme is used for the sake of simplicity. A comparison of all individual tests and mean R-curves is given in Figure 3.7. First,

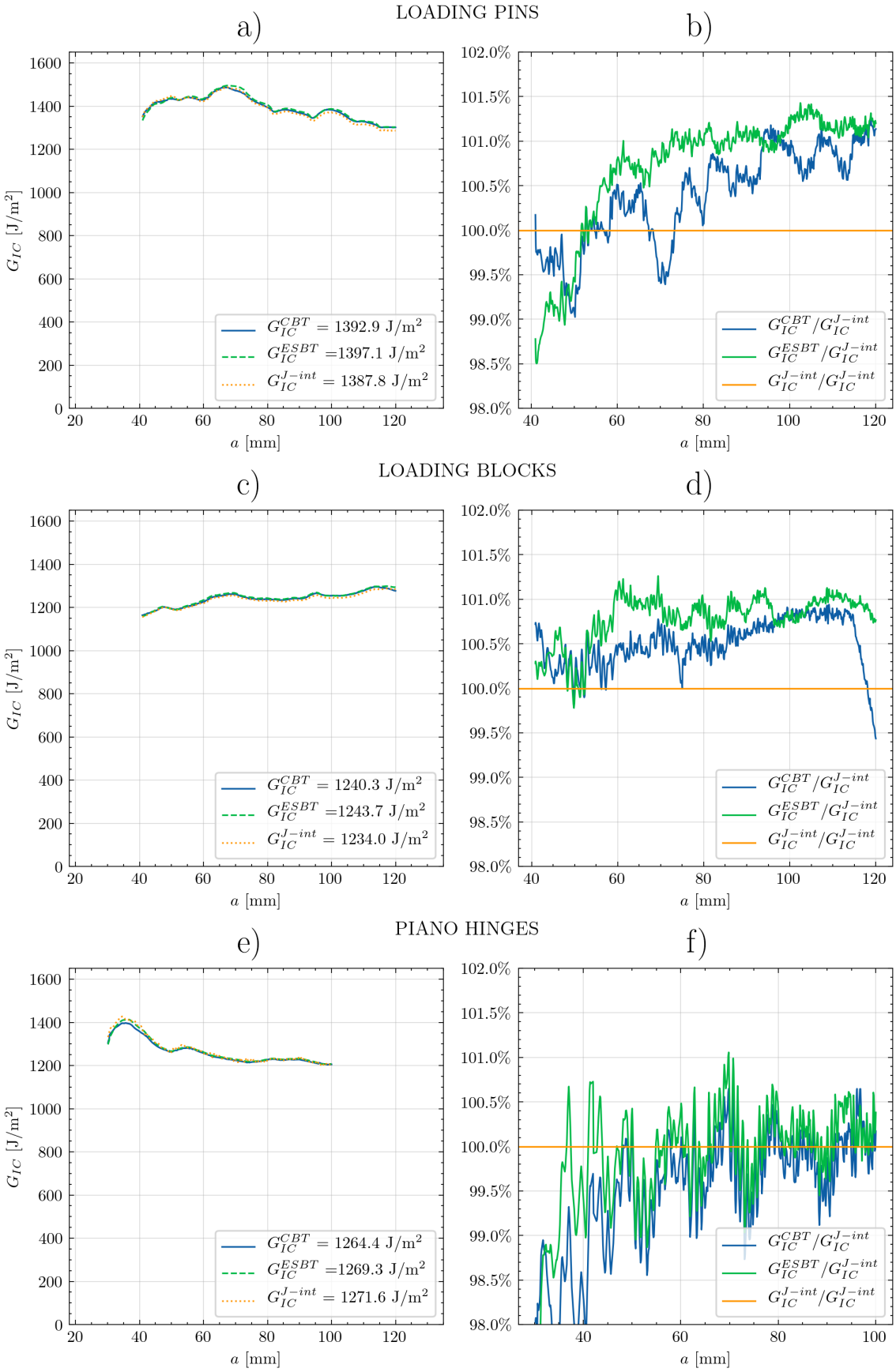

Figure 3.6: R-curves obtained using different data-reduction schemes for: a) - b) loading pins, c) - d) loading blocks and e) – f) piano hinges. Note that in legends of the left-hand side figures average computed values of the fracture resistance are given

from Figure 3.7.d) it seems that the specimens with loading pins show higher fracture resistance than the other two loading arrangements. However, it can be noticed that the scatter, not only between individual tests, but also within a single test is relatively large.

In theory, in case of a homogeneous interface, the shape of the R-curve should be a plateau, suggesting that the fracture resistance is an inherent material property constant along the interface. However, this is rarely achieved in reality because of the influence of the imperfections at the interface between the substrates (e.g., substrate surface preparation [92], type of failure, voids in the adhesive, variation in thickness [93, 94]). On the tested specimens, no significant differences in thickness of the adhesive layer or defects on the interface (such as voids of interfacial failure) that could be responsible for such a behaviour were noticed. Nevertheless, a more careful visual inspection indicates that the crack surface is not completely uniform.

It was noticed in the course of this work that the roughness of the crack surface can significantly differ along the interface. The calculated values of the fracture resistance were higher on rougher parts of the interface than on the smoother parts. Because these smoother areas, unlike the rougher ones, appeared to be very close to one of the substrates, such a variation of the fracture resistance along the interface might also be caused by a variable crack path over the thickness of the adhesive. In theory [57], if the crack approaches the substrate, the development of the plastic zone is constrained, which is less pronounced when the crack propagation is in the mid-thickness [81]. Therefore, the fracture resistance should be at its peak when the crack is at the half of interface thickness, and gradually decrease when approaching the arms (substrate). A more detailed analysis of the correlation of the topography of the crack surface and the measured fracture resistance is, however, outside the scope of this study, but will be investigated in the future.

Figures 3.7.b),c) and 3.8 show that loading arrangements with blocks and piano hinges had one tested specimen with significantly lower fracture resistance than the remaining two. This is clearly the reason why the mean values of the fracture resistance for arrangements with loading blocks and piano hinges are lower than the mean value obtained for the pins. The average value of the R-curve for each individual specimen with the corresponding standard deviation across the crack length is shown in Figure 3.8, namely for holes/pins (P1-P3), blocks (B1-B3) and piano hinges (H1-H3). If the two specimens with lower fracture resistance (B3 and H3) are omitted from the calculation, fracture resistance appears to be independent of loading arrangement, leading to the mean fracture resistance of 7 considered specimens $G_{IC}^{MEAN} = 1361$ J/m^2. On the other

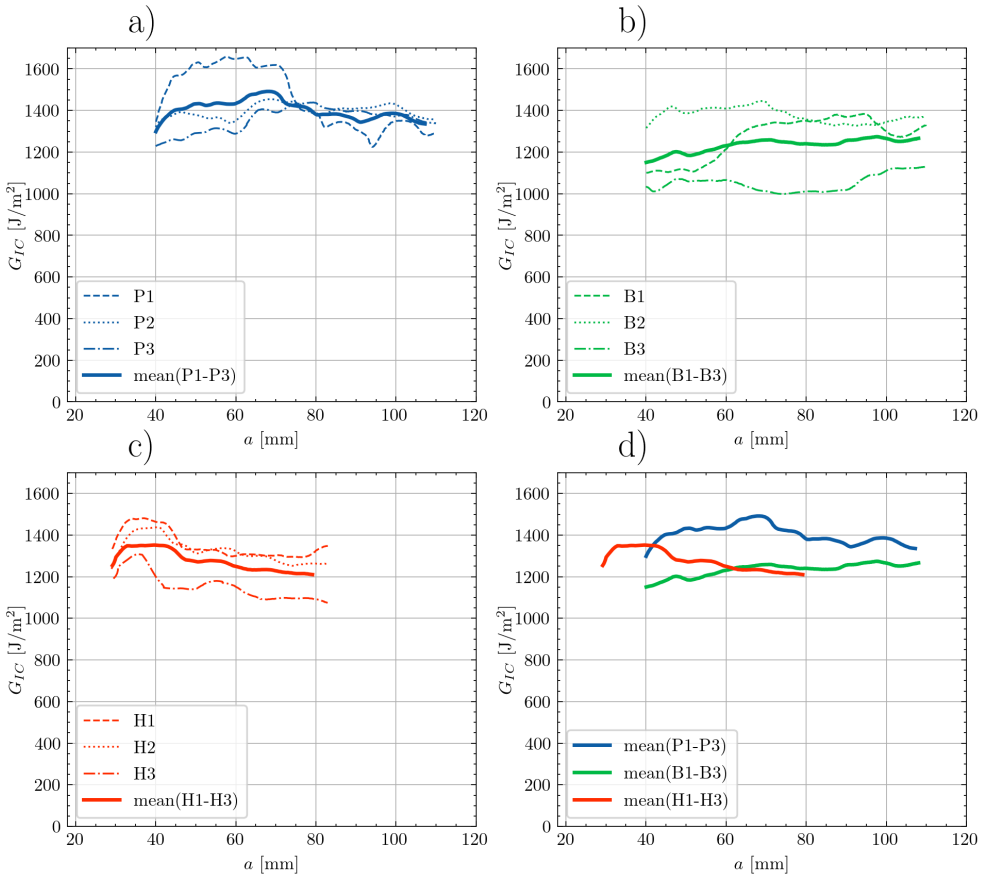

Figure 3.7: R-curves computed using the ESBT data-reduction scheme: a) loading pins, b) loading blocks, c) piano hinges and d) comparisson between loading arrangements using the mean curves. Note that the mean value of the fracture resistance for each specimen or group of specimens

hand, without excluding any specimens, $G_{IC}^{MEAN} = 1303$ J/m^2 is obtained, which is consistent with values reported in [95] for the same adhesive. It should be also mentioned that maximum values of the fracture resistance were obtained for specimen P1, especially on the first part of the interface (see Figure 3.7.a)), where the crack surface was particularly rough.

Specimens with piano hinges show an unusual trend for smaller crack lengths, where a rapid increase in the fracture resistance is followed by a progressive decrease. Initial increase of resistance may be attributed to so-called effect of finite width that is pronounced for smaller crack-length-to-width ratio [63, 64].

On the left-hand side of Figure 3.9, a comparison of force-displacement graphs is shown, where the force is measured by the TTM, while δ on the horizontal axis is either δ_{TTM} (measured from the TTM) or δ_{DIC} (measured directly on the specimen using DIC). Again, only average plots of the three specimens for each of the considered loading arrangement is shown.

On the right-hand side of Figure 3.9, the R-curves are computed using the force-displacement

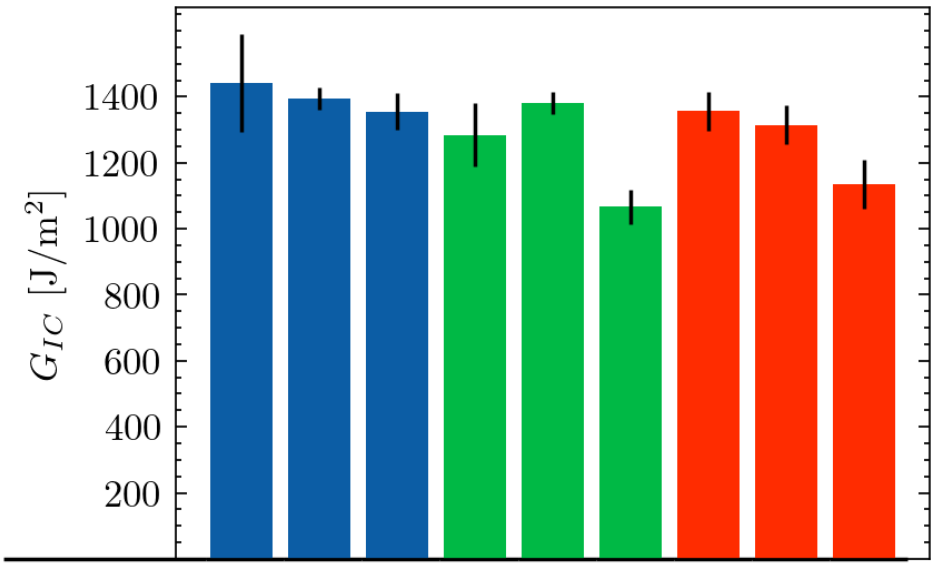

specimen	P1	P2	P3	B1	B2	B3	H1	H2	H3
G_{IC} [J/m^2]	1441	1395	1355	1285	1380	1067	1357	1315	1136
SD [J/m^2]	149	33	56	95	34	52	59	59	74

Figure 3.8: Average value of the fracture resistance obtained using the ESBT data-reduction scheme for each individual specimen with the corresponding standard deviation (SD) across the crack length.

data from the left-hand side of the figure. A comparison of the results obtained using the displacements from the TTM and DIC reveals significant differences in the computed values of the fracture resistance. This effect is most pronounced for the loading arrangement with the piano hinges because, as discussed earlier, this is a loading arrangement that exhibits the largest (plastic) deformations during the test. In addition, it can be noticed that the difference decreases as the crack propagates (and the load decreases), which confirms that the deformation of the loading arrangement is partially elastic.

Erroneous measurement of crack length does not influence the fracture toughness computed by methods adopted in this work. CBT data reduction schemes has an embedded corrections that accounts for an effective lengthening of the crack length, while the ESBT data-reduction scheme and J-integral method do not rely on crack length measurements at all. However, other data-reduction methods from the standard [8] are sensitive to crack length readings, which is demonstrated in the Appendix A.

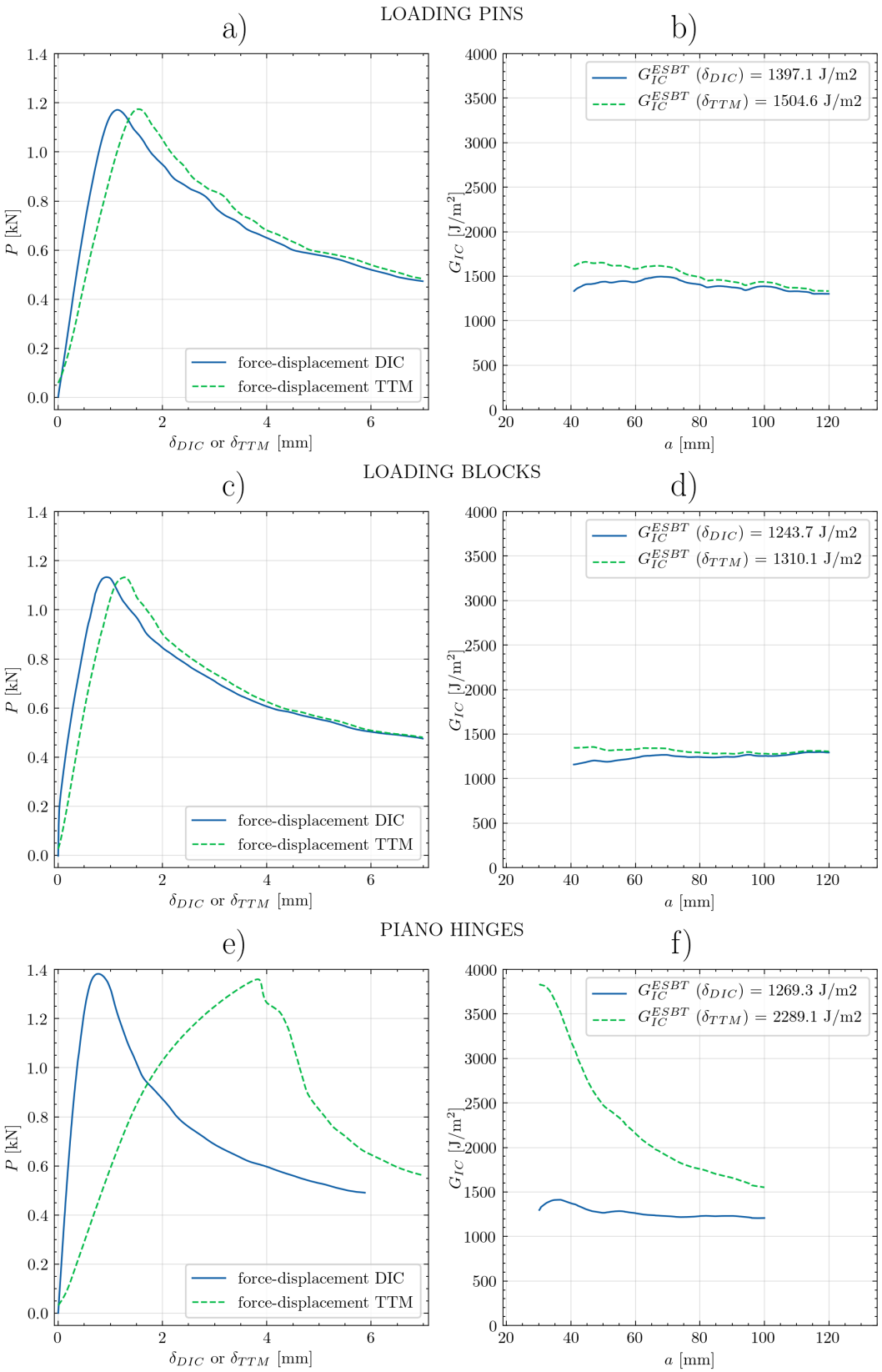

Figure 3.9: Force-displacement plots on the left-hand side and R-curves on the right-hand side plotted with respect to either cross-head displacement from the TTM or load-line displacement measured using the DIC for: loading pins a) - b), loading blocks c) - d) and piano hinges e) – f). Note that in legends of the righ-hand-side figures the average values of the fracture resistance are given.

3.4 Direct Identification of traction-separation law

In this Section, the standard procedure for obtaining the traction-separation law (TSL) of the adhesive interface [15,19,26,34] is used to assess the effect of the loading arrangement on the shape of the TSL. In a DCB test, a TSL defines the change of normal traction (stresses) transmitted at the interface between the substrates with respect to their relative separation δ. Therefore, a TSL essentially defines the function $\sigma(\delta)$, whose integral over δ is in general equal to the non-linear critical energy release rate [7], which, for homogeneous interfaces [11], is equal to the J integral, i.e.

$$J_{INT}(\delta) = \int \sigma(\delta) d\delta \tag{3.3}$$

Here it must be emphasised that values of the J integral shown in R-curves in Section 3.3 are the critical values of the J integral (J_{IC}, as defined in Equation 2.33), which are obtained when in integral 3.3 the lower and the upper boundary are 0 and δ_C (the critical opening), respectively. The critical opening corresponds to a complete failure of the adhesive, after which the transmission of normal tractions between the substrates is no longer possible, i.e., $\sigma(\delta_C) = 0$.

Therefore, at the beginning of a DCB test, at the initial crack tip, the values of the J integral (as defined in 2.33) will increase from 0 to the J_{IC}, where the latter represents the fracture resistance. Once the fracture resistance is reached, the crack will propagate to $a > a_0$. According to Equation 2.33, $J_{IC}(\delta)$ is computed using the cross-sectional rotations of the arms at the load line θ. By analogy, values of $J_{INT}(\delta_{INIT})$ at the initial crack tip prior to crack propagation can be evaluated using the corresponding θ, where δ_{INIT} is the separation of the interface at the initial crack tip. Once that $J_{INT}(\delta_{INIT})$ is defined, the TSL can be expressed as the change (derivative) of the fracture resistance (J_{INT}) with respect to increase in separation, i.e.

$$\sigma(\delta_{INIT}) = \frac{dJ_{INT}}{d\delta_{INIT}} \tag{3.4}$$

Left-hand side (orange dots) of Figure 3.10 shows experimental data of fracture resistance vs. separation obtained using the mean values for each loading arrangement. Because of the scatter of these data, evaluating the derivative in Equation 3.4 is not straightforward. One approach would be to fit the data using a smooth and derivable function, but this has not been done here, because the aim was not to make any a priori assumptions about the TSL shape, but to obtain

it with minimal modifications of the measured data.

Piece-wise quadratic fit by Savitzky-Golay (SG) filter [96] was used because its derivative will yield piece-wise linear function with no overfitting, resulting in TSL shown in right-hand side of Figure 3.10. This method relies on fitting successive subsets of adjacent data points which reduces the high frequency noise and yields a smooth differentiation. For least square quadratic fitting, three neighbourhood points are considered at each side, i.e. window length for Savitzky-Golay filter is 7. Passing filter shifts vertically the centre point so that it satisfies the quadratic best-fit function for a given window, which is repeated for each successive point. The aim is to smoothen the noisy data before taking the derivative without distorting the original data.

In addition to the presented procedure of direct identification, non-linear least square method exponential fitting can be used. However, the differences are not significant so the straightforward best fit approach is only briefly presented in Appendix B.

The direct identification procedure is highly dependent on measurement precision. Theoretical precision of DIC for the current setup is below 1 micron. In Figure 3.10, one can see that the experimental noise has increased over the course of the experiment. Best precision is achieved for loading pins arrangement, which was tested first, while the piano hinge arrangement has the highest noise. Temperature, lighting conditions or possibly pattern quality might have changed and affected the precision. It is interesting to note that for all loading arrangements, the traction is close to zero at separation value of 80 microns (Figure 3.10). Therefore, this value is adopted as the maximum separation δ_C and used as a threshold for the crack length measurement.

The characteristic length, which is the separation corresponding to the maximum traction (peak stress) σ_{MAX}, is equal to $\delta_0 = 0.004$ mm regardless of the loading arrangement (see the right-hand side of Figure 3.10). Values of the peak stress were lower for piano hinges than for the other two loading arrangements. This may be attributed to the lower stress triaxiality (or T-stress) of piano hinges loading arrangement [88] since an increase in the stress triaxiality elevates the strength of most polymeric materials, including epoxy adhesive layers [62]. Given that the geometry of the specimens is the same for all loading arrangements, it can be assumed that any 3D effects that might occur have the same influence on all specimens regardless of the loading arrangement once the crack tip is sufficiently distant from the load-application point. Obviously, this is not the case at the initial crack tip where the TSL is typically identified. A comparison of the extracted TSLs for each loading arrangement is given in Figure 3.11.

Because the presented procedure for direct identification of the TSL takes into account only

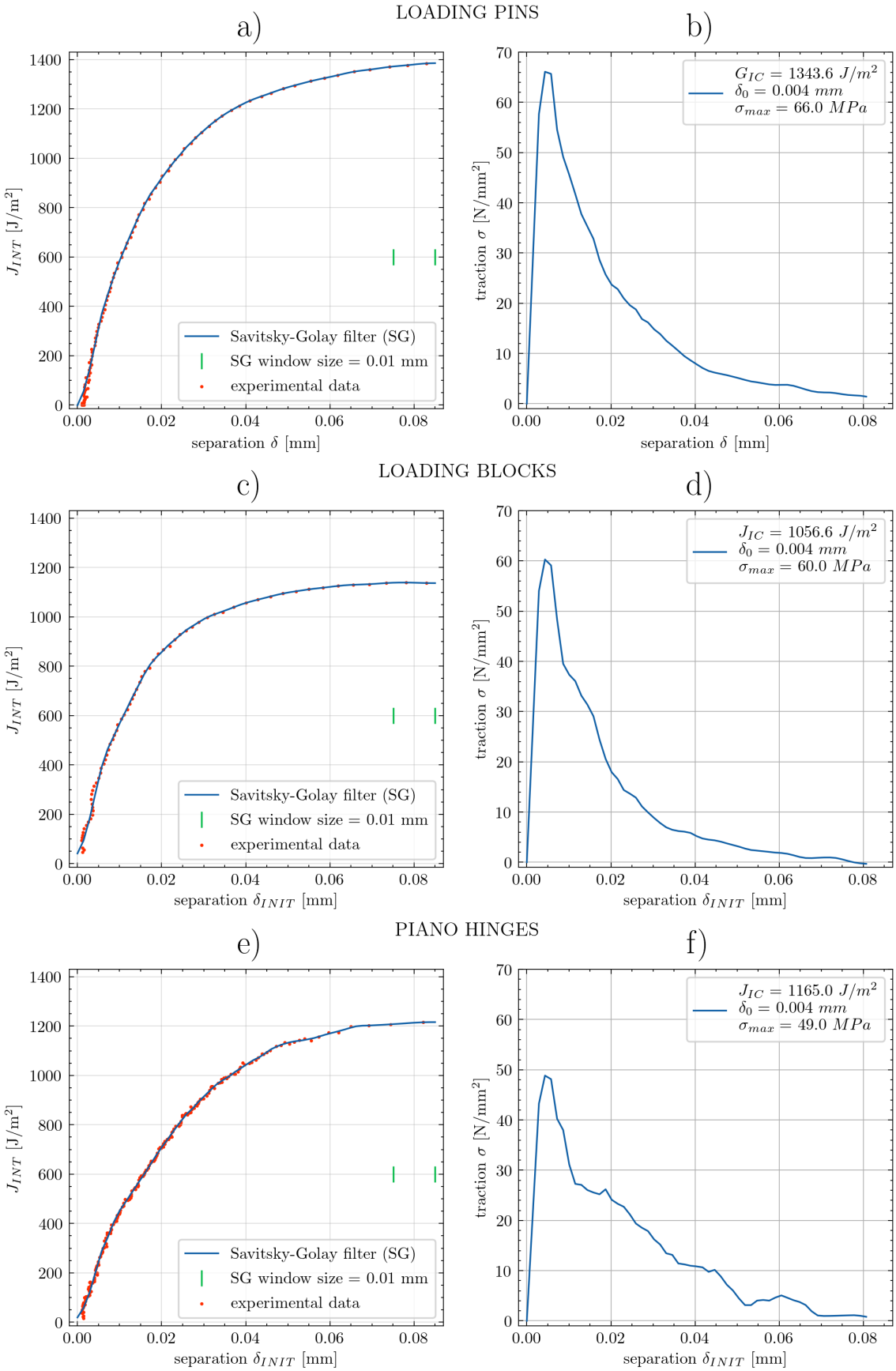

Figure 3.10: Direct identification of the TSL: loading pins a) - b), loading blocks c) - d) and piano hinges e) – f)

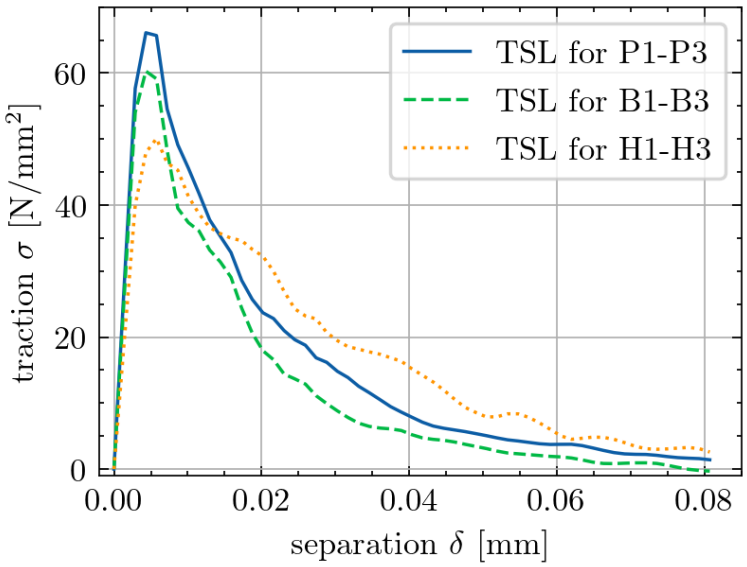

Figure 3.11: A comparison of the identified TSLs for different loading arrangements.

the fracture resistance at the initial crack tip, it is questionable whether the extracted TSLs are representative for the rest of the interface. For example, for the loading blocks and piano hinges, the evaluated values of fracture resistance at the initial crack tip were lower than the average, while for the piano hinges, it is the opposite. This can be observed in Figure 3.7.d). Consequently, the average values of the fracture resistance obtained from the R-curves are more representative and reliable.

3.5 Plate-like specimens

In addition to the investigation of different loading arrangements, an investigation of the influence of the specimen width has been performed. For that purpose, specimens of three different widths were considered, namely 120, 60 and 30 mm specimens. Accordingly, designations A120, A60 and A30 were introduced. Again, all specimens had equal length $L = 250$ mm and thickness of the plates $h = 8$ mm. Specimens of different widths were manufactured in parallel with the intention of distributing the potential influence of cartridge open time across all specimens evenly.

Following the discussion presented in Section 3.2 about the influence of load application system it was decided that the loading blocks were the most suitable for the current analysis. Loading system was designed so that the rotation is enabled in all directions, i.e. around all three coordinate axes. Figures 3.12 and 3.13 depicts the design of different specimen geometries.

Preliminary tests on specimens made of 6060 grade aluminium alloy with the same adhesive revealed problems with aluminium substrates that exhibited permanent plastic deformation.

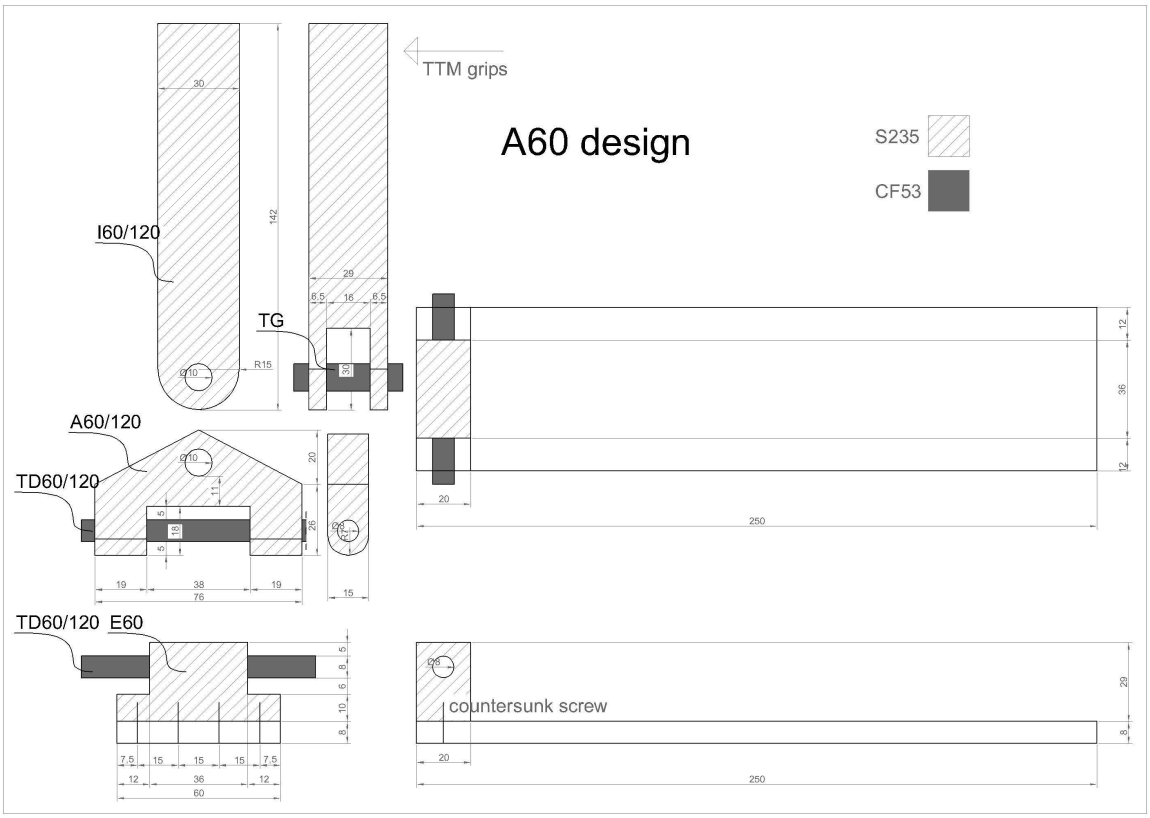

Figure 3.12: Load application system for A60 specimens

Experimental data collected from such experiments would be unusable as all relevant analyses of the adhesive's fracture resistance are based on the assumption that behaviour of the DCB arms is linear elastic. Therefore, a new set of aluminium plates with a higher yield strength was required in the experimental design. In terms of yield strength, the best available option at the local market was 7075 grade aluminium alloy. After testing a dog-bone shaped specimen, the yield strength $R_{0.2} = 533$ MPa and modulus of elasticity $E = 70$ GPa were obtained, which was satisfactory. In fact, no plastic deformations were noticed in the DCB arms after testing specimens made of 7075 grade aluminium alloy.

The adhesive thickness was initially controlled by guide rails during the application on each plate. Afterwards the assembled DCB specimens were manually pressed together with thickness controlled by 0.5 mm plastic wires. Subsequently, the specimens were loaded with weights during the curing phase. Narrow specimens A30 were loaded with 1 kg, A60 specimens with 3 kg and wide specimen A120 with 8 kg. See Table 3.1 with the average thickness for each specimen determined as the difference of the total thickness of the DCB specimen after and before applying the adhesive. A mean value of the measurements on each side near the initial notch and near the mid-length was used. The final thickness of the adhesive ended being thicker in case of

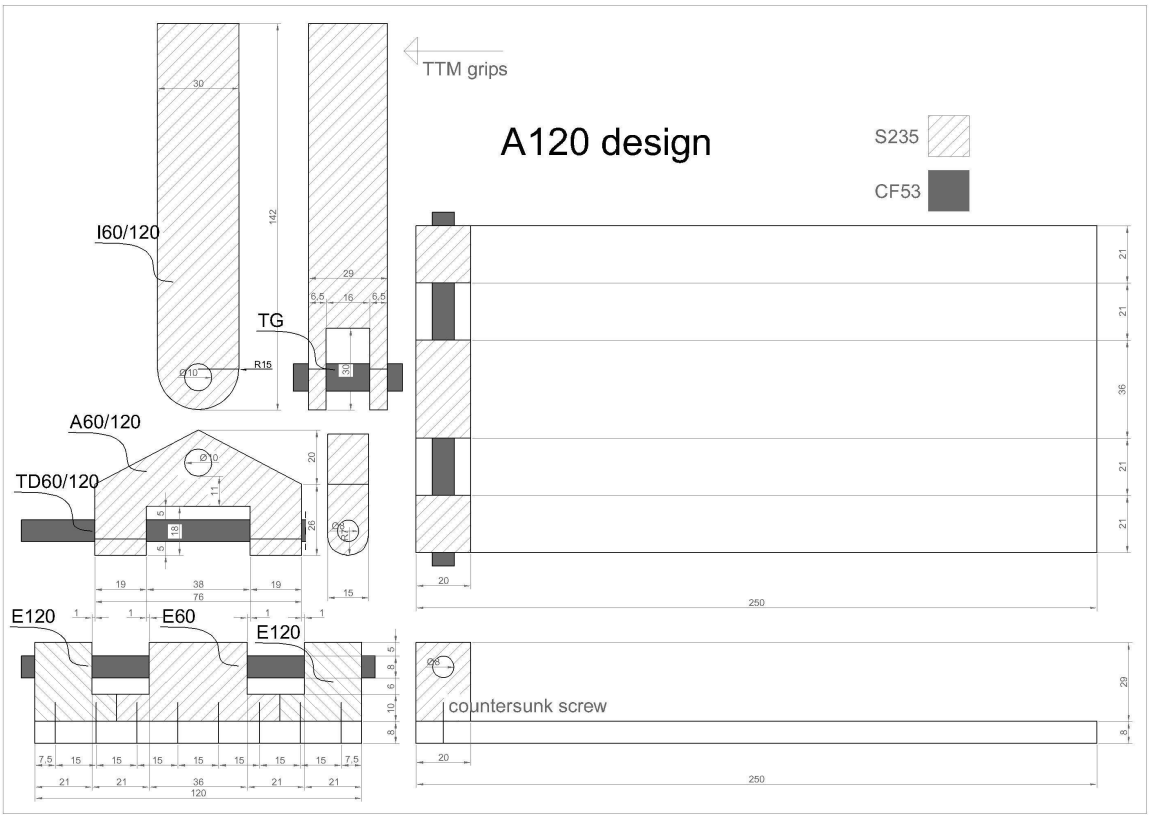

Figure 3.13: Load application system for A120 specimens

wider specimens. Although during the phase of curing of the adhesive the specimens were loaded with weights in a way that the average pressure at the edges is approximately constant for each geometry, with the increase of the width it apparently became more difficult to squeeze out the excess adhesive.

Moreover, as shown in Table 3.1, significant differences in the average adhesive thickness were also noticed among individual specimens with the same width. However, by analysing individual specimens, no correlation between the adhesive thickness and the fracture resistance was observed. It is therefore reasonable to deduce that for the tested set of specimens, the increase of the adhesive thickness with the width of the specimen will not have a dominant influence on the computed values of the fracture resistance.

Interesting to note is how some specimens exhibited unstable crack growth at one point. Instead of a relatively common stick-slip crack propagation [8], in some of the present cases the crack propagated suddenly without arrest before specimen failure. As depicted in Figure 3.14 for specimen A120-1, the onset of unstable crack propagation is visible on the fracture surface as the location where the fracture surface topography changed from rough to smooth surface. The position of this change left a marked crack front, thus suggesting that the crack has a

specimen	plates w/o adhesive 2h [mm]	glued plates 2h+t [mm]	adhesive thickness t [mm]
A30-1	16.46	17.03	0.57
A30-2	16.42	17.08	0.64
A30-3	16.50	17.10	0.60
A30-4	16.45	16.83	0.38
A30-mean	16.46	17.01	0.53
A60-1	16.51	17.51	1.00
A60-2	16.53	17.29	0.76
A60-3	16.47	17.42	0.95
A60-4	16.51	17.33	0.82
A60-mean	16.51	17.39	0.88
A120-1	16.35	17.97	1.63
A120-2	16.40	17.92	1.28
A120-3	16.45	17.55	1.03
A120-4	16.52	17.37	0.85
A120-mean	16.43	17.70	1.20

Table 3.1: Average thickness for each specimen

curved shape. The behaviour with a sudden failure was noticeable for A30-3, A60-3 and all A120 specimens, although it was most pronounced for specimens A30-3, A120-02 and A120-03.

As evident from the Table 3.1, those specimens generally had a relatively thick bond, which seems to be in line with the explanation given in [57] about the higher thickness being correlated with the unstable manner of crack propagation. However, this correlation is debatable since the thickest A30 and A60 specimens, namely A30-2 and A60-1, had a perfectly steady state propagation.

As an alternative explanation, unstable crack growth could be simply due to specimen preparation. The adhesive was more carefully applied near the initial crack than at the specimen's tail where the excess adhesive that remained from the previous application was purposely reused to reduce waste. At the position of specimen's tail, the crack propagation is seldom monitored [8] while the tractions are inconsiderable [11] for the majority of experiment, which means that in this way the specimen is not weakened. However, for specimen A120-01 in particular (see Figure 3.14), when the crack approached the tail it came very close to the weaker part containing the air pocket. Unjoined part with the air pocket was probably a result of reusing the excess adhesive. Therefore, inferior specimen preparation at the specimen tail in conjunction with higher thickness could result in the abrupt failure of certain DCB specimens. There will be more mention of the abrupt failure at the end of this chapter, along with depictions of the crack propagation for the individual specimens.

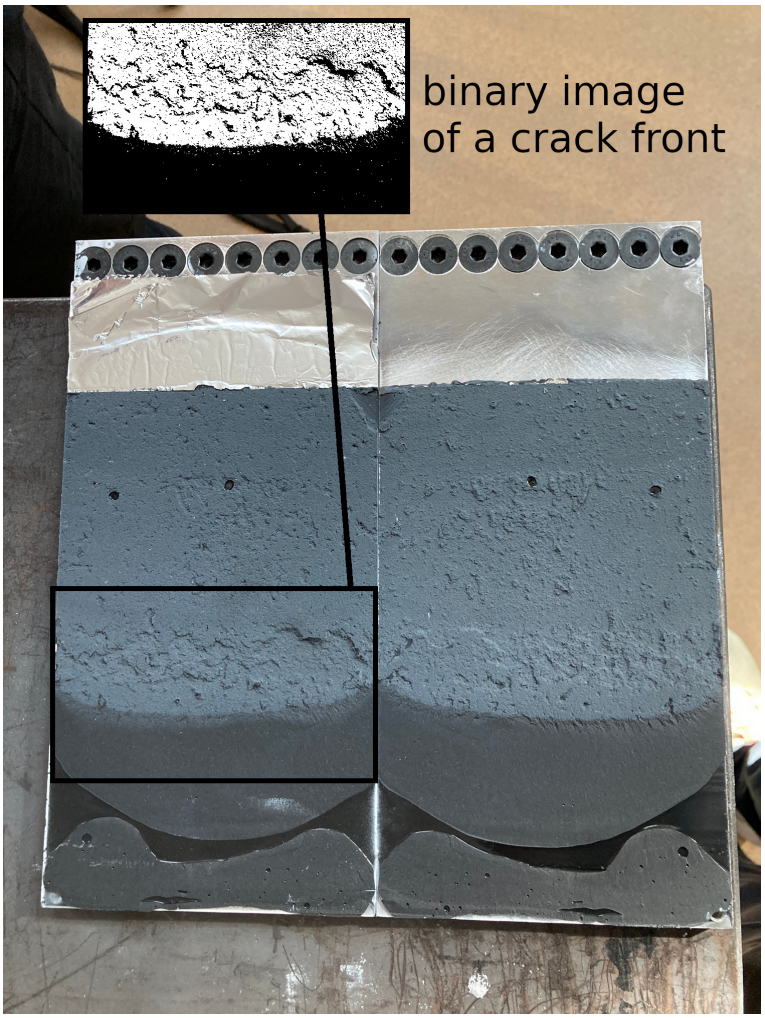

Figure 3.14: Inspection of fracture surfaces for specimen 120-1 with enlarged crack front marks shown in binary pixel values

3.5.1 Symmetry Based Top Surface Analysis

There are few available methods to determine the fracture resistance of wide specimens, i.e. specimens in which the width is comparable to the length. In this scenario the beam theory does not apply because the crack front is not a straight line i.e. $dA \neq B \cdot da$ as assumed in Irwin-Kies Equation (2.7) is no longer valid. The experimental analysis of the double cantilever beam test generally relies on the beam theory, hence the applicability of determined material properties to plate-like geometries is questionable. Experimental findings [63] show that the crack front is curved and that the crack length at the specimen's edges is shorter than at its center. Earlier research [63, 66] reported that curved crack front has a parabolic shape and this is also verified by the present thesis in Section 5.2.

International standards [8, 9] give instruction on how to measure the crack length along the edge of the specimen assuming that the crack front does not vary along the width of the specimen.

However, this assumption becomes very questionable for relatively wide specimens. With digital image correlation it is possible to measure the crack along the entire width, not only at the edges. This is done by using a measurement method that takes advantage of the experiment symmetry, as will be presented hereafter.

Measuring volume of the DIC system is basically an imaginary cube (see Figure 3.15) that is observed in sharp detail by the cameras. Its size depends on the camera lens, aperture opening and working distance to the observed object. GOM Aramis system provides guideline tables with expected measuring volume size for the chosen setup. For experiments presented in this section, setup with the measuring distance of about 480 mm leads to a measuring volume of 285x220x220 mm^3.

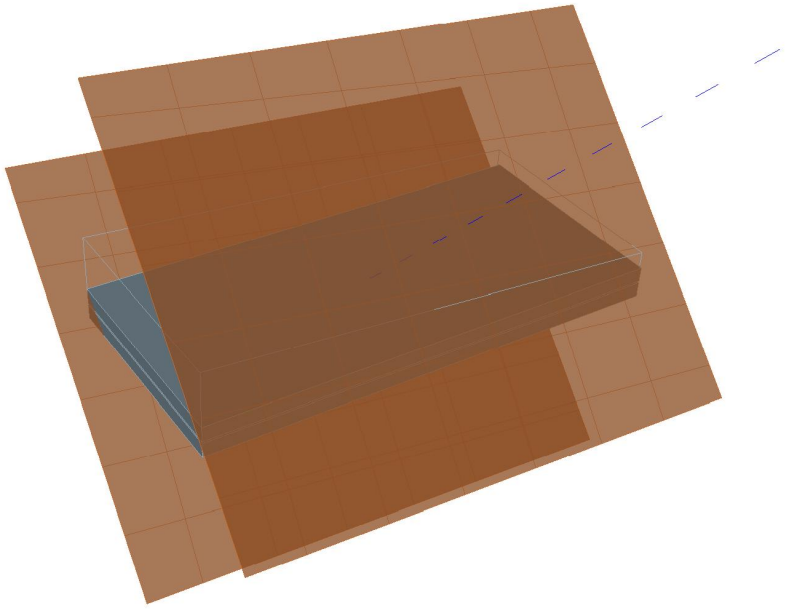

Figure 3.15: Measuring volume with the mid-line of stereo DIC rays, note how the edge of the specimen on the right is just slightly outside of the DIC measuring volume

The largest DCB specimen A120 is the hardest to fit into a measuring volume, ultimately defining the size of it. The optimal position of the cameras is the one that achieves the best image quality of the observed regions. The aim is to have a good image quality of both specimen's top and side surfaces. Given that a large angle of incidence may lead to a poor image quality, cameras should be observing both surfaces at about 45 degree with respect to their normals. Furthermore, camera's sight of observed surface should not be obstructed by obstacles such as loading blocks. For this reason, both cameras were slightly shifted horizontally in the direction

of specimen's tail (away from the blocks) and oriented towards the specimen, while keeping the desired measuring distance. After a few trial and error positioning attempts in CAD software, the above-mentioned measuring volume was found to be suitable since, even after accounting for separating motion of the DCB arms, observed surfaces were found to be inside the measuring volume throughout the experiment.

DIC technique is useful for monitoring the displacements of a specimen. Primary area of interest is the relative displacement between the adherends, although the displacements will be measured for each subset, with about 4000 subsets in total for the largest specimen A120. Cameras can observe displacements only on the visible surfaces of the specimens (see Figure 3.16). This limitation was overcome by assuming the symmetrical behaviour of the specimen and measuring the top side relative displacements with respect to the plane of symmetry. Interface separation or opening is then double of the measured relative displacement. Presented approach is based on a methodology similar to the so-called Top Surface Analysis (TSA) [97]. The main difference is that **in [97] the separation data is extracted for a limited number of sections while herein presented approach is applicable to the full-field data**. Furthermore, instead of using linear regression to reconstruct the central axis by extrapolation (as done in [97]), it may be preferable to utilise symmetry, which is explained below in detail. Therefore, presented approach can be named Symmetry Based Top Surface Analysis (SBTSA).

First, a global Cartesian coordinate system is constructed so that the x-axis, y-axis and z-axis are aligned parallel to the length, width and height of the specimen, respectively. This is done manually at the initial stage by the so-called 3-2-1 locating principle. This basically means creating and selecting the six (3+2+1) points located at the specimen's visible side near the load-line. Figure 3.16 shows these points denoted only as LLT,LLB,LL0,S1 since some of them are reoccuring. Three points required to define the x-z plane are LLT,LLB and S1, points LLT,LLB are reused to construct the z-axis, and consequently the remaining two directions, while the last point LL0 is needed for the origin of global coordinate system.

Knowing the geometry of the specimen is useful for repositioning the global coordinate system. In fact, centre point of the top surface marked as SC can be constructed post-experiment as the intersection of top surface's diagonals and, according to Figure 3.16, should have the coordinates ($x = L/2 = 125$, $y = B/2 = 60$, $z = H + t/2 = 9$). It is useful to check whether the centre point coordinates coincide with its beforehand known position. If necessary, the chosen six construction points can be redefined so that the centre point lies at the desired position within the global

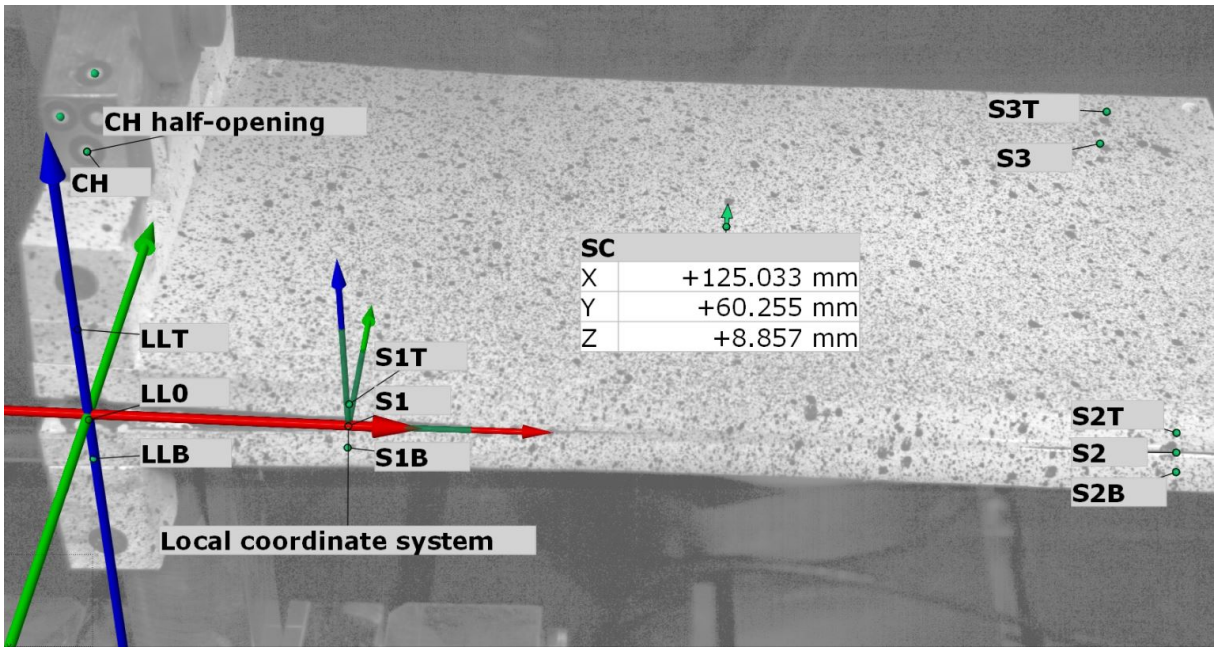

Figure 3.16: GOM Aramis screenshot of coordinate systems construction with the points needed for SBTSA denoted as LLT, LLB, LL0, S1T, S1B, S1, S2T, S2B, S2, S3T, S3, SC

coordinate system. A few iterations are usually sufficient to achieve millimetre precision of the centre point (SC) position. This step is a potential source of error for the later analysis since it defines the vertical z-axis, i.e. direction in which the relative displacement will be measured. It seems challenging to perfectly position the specimen horizontally because a slight tilt is often present (and acceptable). For example, top surface slope can be about 1 degree due to different elevation of opposing top surface vertices (corners).

The next step is to define the plane of symmetry using three points S1,S2 and S3 so that the rigid body motion compensation of all displacement measurements could be performed. Two of these three points lie at the specimen's side (S1,S2), and are constructed as midpoints of manually selected points near the initial crack (S1T,S1B) and near the specimen' tail (S2T,S2B), respectively. The third one (S3) is constructed from an vertical offset of the top surface point (S3T) that is far away from the visible specimen side. Furthermore, it is desirable to select the top surface point S3T near the specimen's tail since it will be free of deformation for the most part of the experiment. In order to select a point that is located at the plane of symmetry, the vertical offset distance should be the thickness of the plate plus the half-thickness of the adhesive. Obviously, the earlier definition of the vertical direction (global z-axis) is here of a considerable importance.

Finally, the plane of symmetry can be used to define a x-y plane of the local Cartesian

coordinate system, which is a basis for the rigid body motion control. Recalculation of local coordinate system in each time step ensures that the ensuing specimen's rotation will not affect the measurements. The measured vertical relative displacement of the top surface can now be assumed equal to the interface separation. Furthermore, temporal and spatial interpolation filter is applied to reduce the noise. The filter takes into account data of the two nearest stages, and nearest 4 facet points, respectively.

As an alternative to this approach, the identified surface may be attached to the previously imported CAD model of the specimen, and it may even be improved using the iterative closest point algorithm [98]. However, top surface analysis was not checked against this alternative approach but compared to a numerical model. An additional and more robust check would be to use X-ray tomographic imaging.

According to the technical data for SikaPower-4720, maximum elongation at break equals 3 percent which for an adhesive thickness of 0,60 mm will result in 0.02 mm elongation/separation, which is significantly higher value than extracted by direct identification. However, this value could be influenced by the stress triaxiality, as the maximum elongation is retrieved for predominantly plane-stress conditions while the current DCB setup is predominantly in plane-strain conditions, regardless of the varying geometry.

In order to define the damage process zone (DPZ), also known as the fracture process zone, limit displacement values must be defined in order to create a contour plot of DPZ, as the one shown in Figure 3.17. These **DPZ threshold values** are the characteristic separation δ_0 and the critical separation δ_C, i.e. the separation that corresponds to maximum traction σ_{MAX} and the critical separation value δ_C that corresponds to interface fracture. Values $\delta_0 = 0.004$ mm and $\delta_C = 0.080$ mm, obtained from a direct identification of traction-separation law from the previous set of experiments, presented in Section 3.4, are for now adopted also for the wide specimens. After considering the fact that only half-separation is measured with respect to plane of symmetry, and after accounting for measurement noise simply by rounding to higher value, limit values of DPZ are adopted for the purpose of contour plot in Figure 3.17 as 0.01 and 0.05 mm, for damage onset and fracture, respectively. For the sake of simplicity, the influence of stress triaxiality on the DPZ limit values is neglected in this analysis, i.e. the transition from plane-stress to plane-strain conditions across the width of the specimen is not taken into account.

By observing the contour plot in Figure 3.17, one can trace the shape and movement of the crack front. Blue color represents intact interface while the red color indicates that the interface

is broken. It is obvious that crack is not a straight line across width but rather a parabola-like curve. In fact, the crack is longer in the middle of specimen than at its ends. This is known in literature as crack-front tunnelling [60] and it is mostly caused by anticlastic bending of plates. In fact, by analysing the shear force distribution at the cantilever clamped support according to the plate theory higher traction are obtained in the middle of the width, as described in Section 5.2 in more detail.

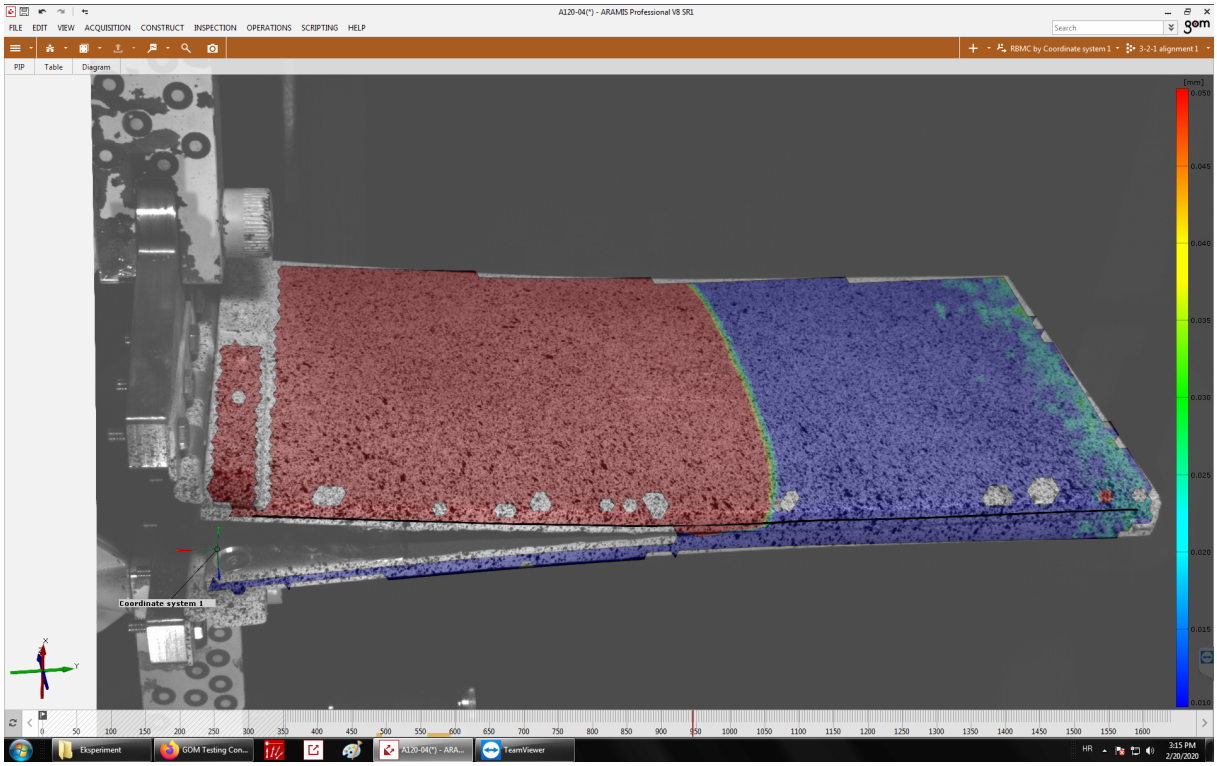

Figure 3.17: Contour plot of A120 specimen opening separation with red and blue contour limits representing the edges of the DPZ (δ_0 and δ_C)

As earlier in Section 3.2, a substantial difference of about 0.3 mm was registered between the cross-head and load-line displacement. For the sake of simplicity, cross-head displacement was corrected by deducting the average value of the aforementioned difference for each specimen geometry (instead of the exact approach depicted in Figure 3.5). The value of this correction substantially increased with the increase in the specimen width, yielding 0.2, 0.3 and 0.4 mm, for the specimens A30, A60 and A120, respectively. Second digit precision was purposely omitted for the sake of brevity and consistency with displacement readings that are interpolated in 0.1 mm steps. As an alternative, the best-fit approach presented in BS ISO 25217: 2009 [8], which would result in average correction of 0.1 mm regardless of the specimen geometry, could be used. The best-fit approach may be questionable since there is no distinct linear part of force-

displacement curve in case of loading blocks since they exhibit high non-linearity due to the stiffening effect. The stiffening effect of end blocks exerts a negative moment with direction as if the end were fixed and the reduction of the lever arm occurs as the arms deform. Regardless of the approach, it is highly recommended that the displacement used for data reduction scheme and comparison against numerical simulations are as accurate as possible and appropriately corrected. An illustration of the importance of this correction, especially on the initiation value of the fracture toughness, can be found in [80].

3.5.2 Area method

To the best of author's knowledge, fracture resistance tests are performed exclusively for beam-like specimens. This is done by monitoring the applied force, displacement, and crack length. The latter is usually assumed to be uniform across the specimen's width throughout the DCB test. Data-reduction schemes are used to compute the fracture toughness using the specimen's compliance computed from the beam theory. As an alternative, the area method [24] can be used to compute the energy release rate for different test setups, including the DCB test. This method is quite straightforward since it follows from the original definition of the fracture toughness (2.3), written as a finite difference, i.e.

$$G_C = \frac{\Delta U}{\Delta A} \tag{3.5}$$

In literature [24] this formula is often expressed under the assumption that the crack front is a straight line ($\Delta A = B\Delta a$) and solving for area between the two considered data points

$$G_{IC} = \frac{1}{2B\Delta a}\left(P_1\delta_2 - P_2\delta_1\right) \tag{3.6}$$

where the values P_1, δ_1 are from the load-displacement data for the first point, while the values P_2, δ_2 is the same data for the second considered point. Standard BS EN 6033:2015 [99] for testing interlaminar fracture toughness of CFRP composites presents this approach as a data-reduction scheme that allows for a simple determination of the average value of fracture toughness. In particular, load-displacement data is recorded at the beginning of crack propagation as P_1, δ_1 and then as P_2, δ_2 when the crack has propagated for approximately $\Delta a = 100$ mm, i.e. it considers only two points. On the other hand, by considering all points during crack propagation in the load-displacement curve to compute the fracture toughness according to Equation 3.5 can

yield a typical R-curve, similar as provided by other data-reduction schemes. In this work, the combination of the two mentioned approaches is used by computing the average value of the cumulative fracture toughness for each subsequent crack area increment. Therefore, the R-curve shows the fracture toughness computed for the currently fractured part of interface.

The numerator in Equation (3.5) is calculated as a trapezoidal rule integral of the area enclosed by the two considered points in the force-displacement curve and the origin of the coordinate system. The area is always measured starting from the point corresponding to the onset of crack propagation and ending with the point corresponding to the considered crack area extension. Crack onset typically occurs slightly after the peak force [85], and in this work it is determined as a moment in time when the relative opening of the initial crack with regards to the plane of symmetry exceeds the critical separation value $\delta_C/2 \approx 0.05$ mm. As depicted in Figure 3.18, the green colored curve (labeled as data w/o NL) excludes the area of the elastic part of the load-displacement curve that usually exhibits a non-linear behaviour caused by stiffening effect of loading blocks [88] and by softening that is happening at the centre of the crack front before the peak force [100].

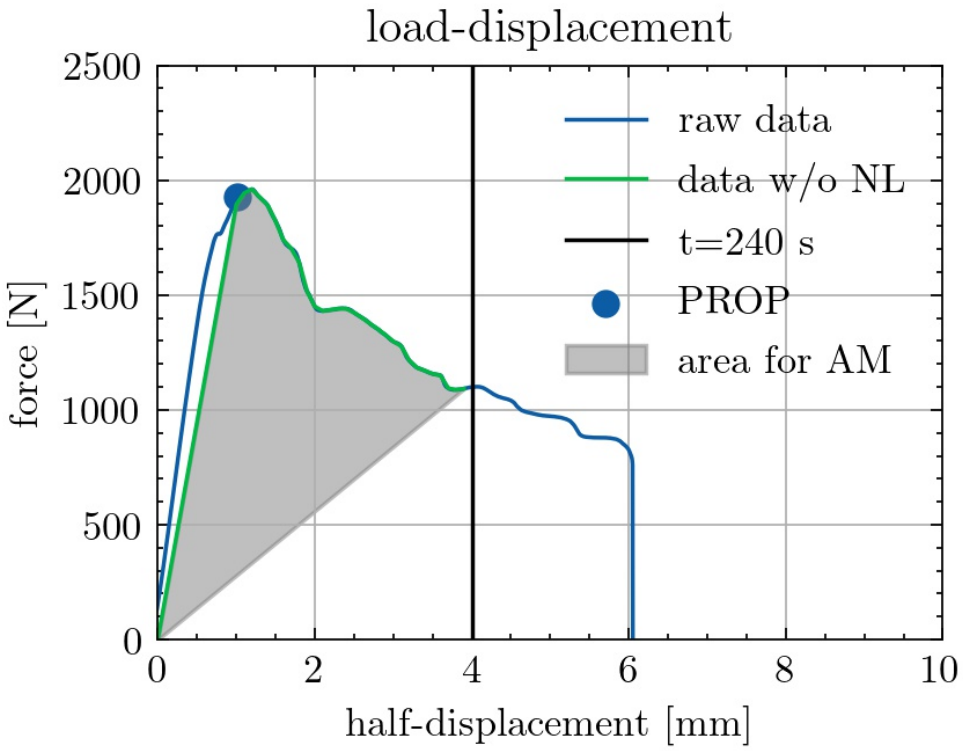

Figure 3.18: Area method (AM, Eq. 3.5) procedure for excluding area prior to crack propagation (data w/o NL - data without nonlinearity, PROP - onset of crack propagation)

The denominator in Equation 3.5 is the propagated crack area which is extracted using the

DIC measurements by tracking the position along length at which the relative separation with respect to the plane of symmetry is **sufficiently close to the critical separation** $\delta_C/2 \approx 0.05$ mm. This procedure may be prone to erroneous readings if DIC data has a significant amount of noise. This often happens near the edges of the specimen since here there is no adjacent area needed for image correlation. However, this difficulty may be dealt with by limiting the permissible crack area extension in each step and also by simply removing the suspect outliers by a statistical method. Note that crack area data is required not only for plotting the R-curves, but also for comparison of experimental and numerical crack front, which will be shown in Section 5.2. Furthermore, to define the onset of crack propagation, the initial crack length was rounded to either $a_0 = 52.5$ mm or $a_0 = 50.0$ mm (in order to conform with FEM mesh). This simplification may lead to errors but mostly for small crack lengths and not much for the final results.

Previous research by Laffan et al. [101] indicated two main drawbacks of the area method. First, the initiation value of the fracture toughness cannot be reliably determined since dividing small values of experimental data will invariably lead to high variance of the results. Secondly, the sensitivity of the area method to Δa indicates that it is not well suited for optical measurements.

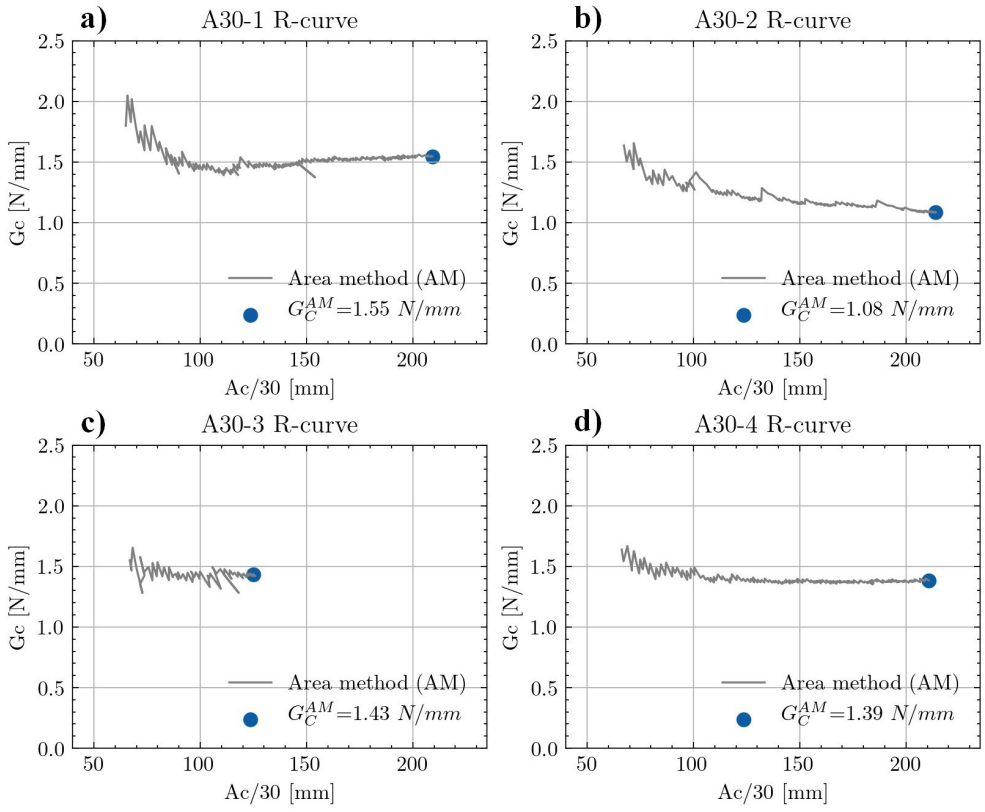

Figure 3.19: R-curve computed by Area method for A30 specimens (Note that the first 12 seconds of crack propagation show large scatter so they are not plotted to keep the the graph uncluttered)

However, in this thesis it is shown that with the procedure presented herein it is possible to determine convincing fracture toughness results, regardless of the specimen geometry. The comparison of data-reduction scheme results is first made for narrow specimens (A30). In this case it is reasonable to assume that the crack front is a straight line and that the beam theory holds. Earlier result of average fracture toughness of 1.30 N/mm (see Section 3.3) is comparable to the value 1.37 N/mm calculated using the area method (see Figure 3.19).

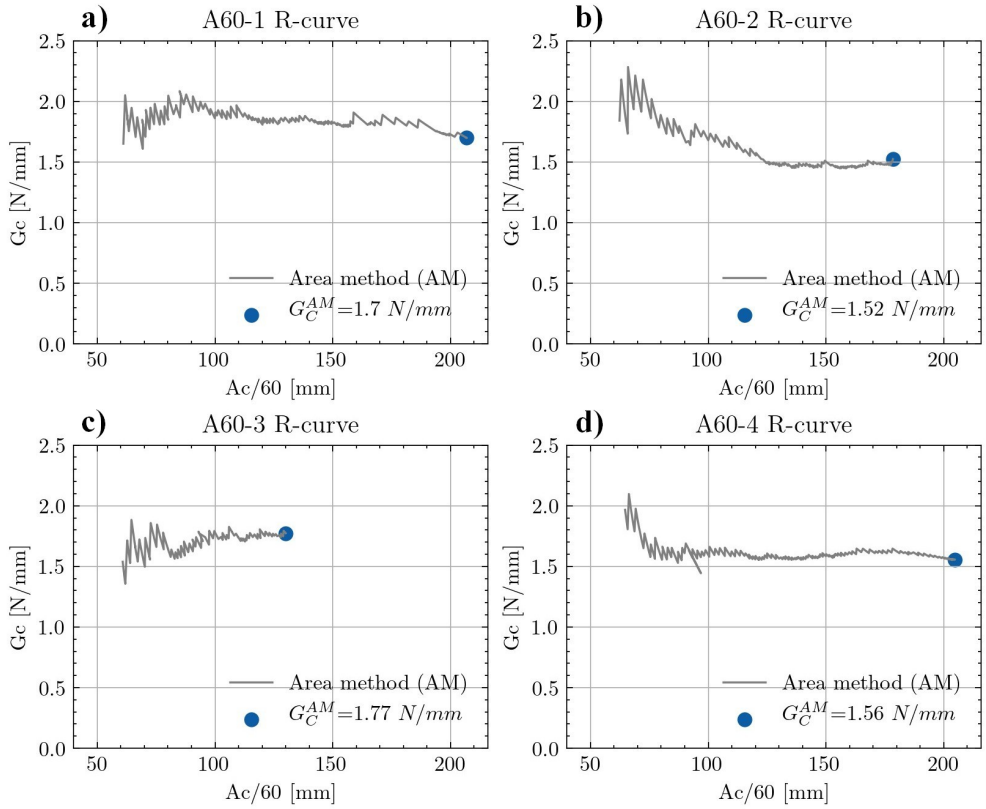

Figure 3.20: R-curve computed by Area method for A60 specimens (Note that the first 12 seconds of crack propagation show large scatter so they are not plotted to keep the the graph uncluttered)

Specimens A60 and A120 (see Figures 3.20, 3.21) show higher fracture toughness with respect to A30. According to numerical model, increase in the width will not lead to higher but lower peak force per width for the same displacement. This means that the change in layer mechanical behaviour with an increased width does not lead to an apparently higher fracture toughness, and, therefore, can not explain this result.

Analysing the average length of DPZ across the width does not imply any change with variation of the specimen width. There are different versions of analytical predictions of the cohesive zone. For example, equation given by Cox and Yang [102] for slender laminates reads

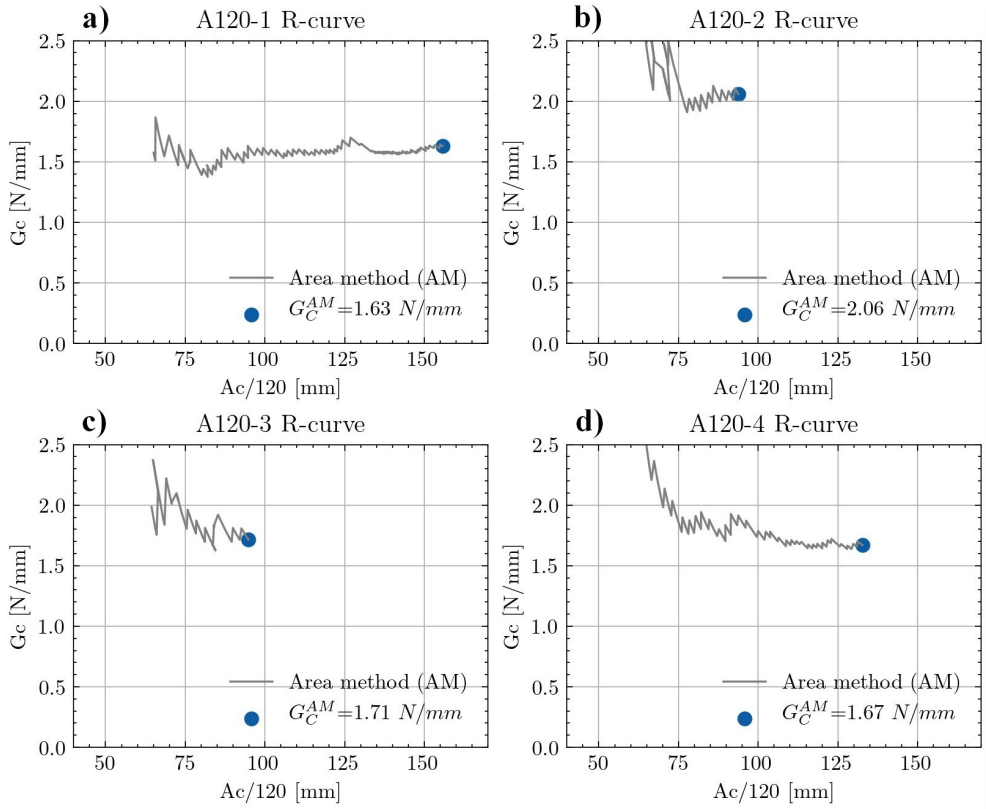

Figure 3.21: R-curve computed by Area method for A120 specimens (Note that the first 12 seconds of crack propagation show large scatter so they are not plotted to keep the the graph uncluttered)

$$l_{DPZ} = \left(E' \frac{G_{IC}}{\sigma_{MAX}^2} \right)^{\frac{1}{4}} h^{\frac{3}{4}} = 7.2mm \tag{3.7}$$

In Figures 3.22, 3.23, 3.24 experimentally measured cohesive zone length was found to be around 7 mm. Interesting to note is, however, that specimens with unrealistically long cohesive zone were actually the few without steady-state propagation (see Figure 3.14) throughout the experiment. This indicates that a significant damage had ensued over a large area before the sudden fracture. Crack front propagation was otherwise comparable to other specimens in terms of position and speed. Likewise, the fracture toughness was comparable to other specimens. Based on the available data and the presented results, it is very difficult to conclude why the fracture toughness changed with the specimen's width without additional experimental analyses. It is also difficult to explain why the unstable crack propagation corresponds with a large DPZ.

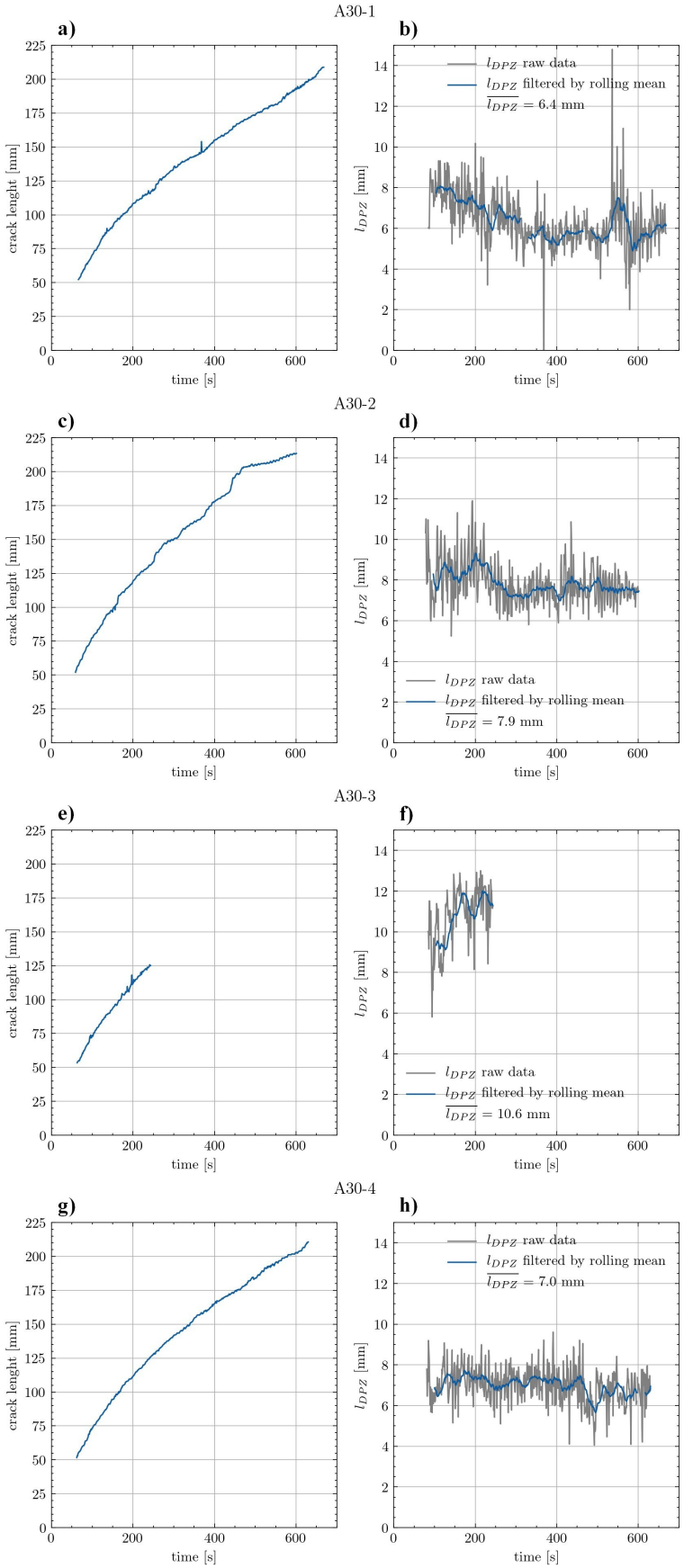

Figure 3.22: Crack propagation with average crack length A_C/B (a,c,e,g) and damage process zone length (b,d,f,h) for A30 specimens

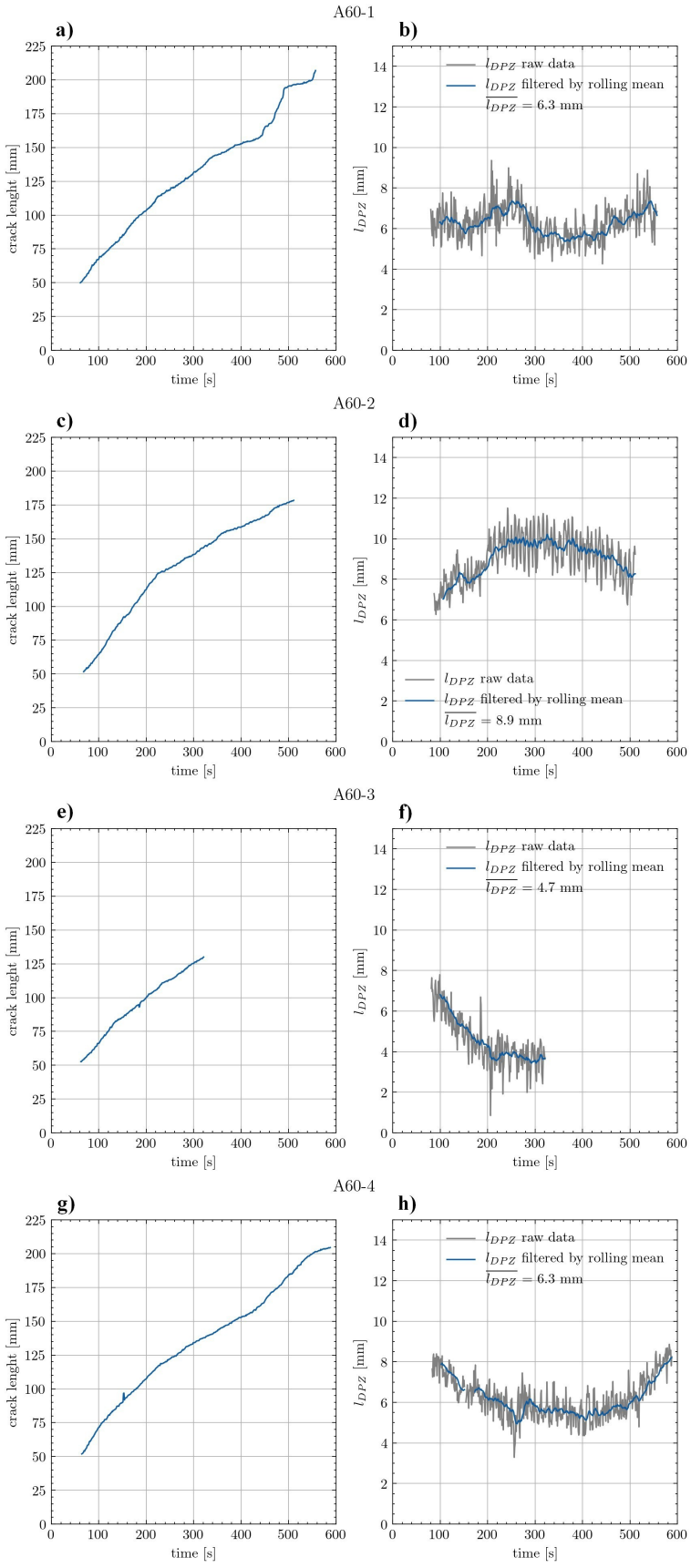

Figure 3.23: Crack propagation with average crack length A_C/B (a,c,e,g) and damage process zone length (b,d,f,h) for A60 specimens

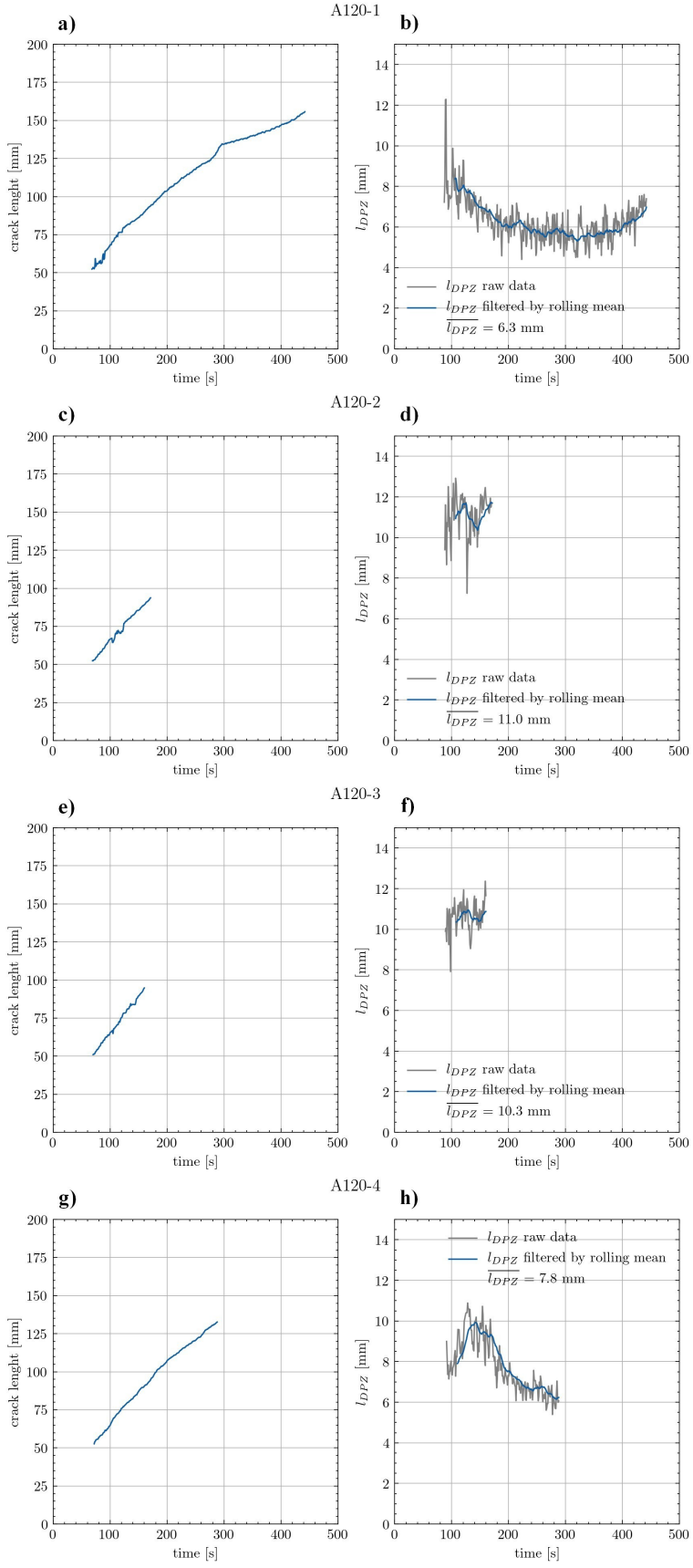

Figure 3.24: Crack propagation with average crack length A_C/B (a,c,e,g) and damage process zone length (b,d,f,h) for A120 specimens

Chapter 4

Numerical Model

In this chapter, a numerical model for debonding of a plate-like DCB specimen is presented. The considered DCB experiment consists of two aluminium plates mutually connected by a adhesive layer through which an initial crack propagates when the opening load is applied. In the first section, the plate finite elements used to model the aluminium substrates E=70 GPa are presented, while the second section focuses on the adhesive that is modelled using the interface elements with a previously identified constitutive law (see Section 3.4). Although the thickness can play an important role in the overall behaviour of an adhesive joint, this is typically not modelled numerically. In fact, the common approach is to embed constitutive laws of the adhesive in the so-called zero thickness interface elements. Moreover, after analysing the average adhesive thickness and the average computed fracture toughness for each tested specimen of the same width, no correlation between these two parameters was noticed (see Section 3.5.2 for details). Accordingly, the constitutive model of the adhesive is here described by a traction-separation law (TSL) whose original derivation is presented in the second section of this chapter.

Initially, the assembled numerical model is studied in terms of efficiency and robustness by comparing it with alternative models. Even though the efficiency and robustness may not have a significant influence on the simulated structural response, they are essential for delamination model to be viable outside of academic purposes. At the end of this chapter, virtual experiments are performed with the aim of validating the data-reduction method presented in the Section 3.5.

All of pre-processing and post-processing code was written in Python, while all FEM calculations were implemented in FEAP [103] finite element software using in-house code.

4.1 Plate Finite Elements

In general, a plate-like DCB experiment with two glued metal substrates can be described using a three-dimensional numerical model. For a typical geometry of a DCB problem [9], beam width to crack length ratio (B/a) suggest that a beam is an inappropriate model for small crack lengths, which is even more pronounced in case of plate-like specimens. Therefore, the following two approaches to modelling the DCB in the finite element analysis framework are presented hereafter.

In the first one, metal substrates can be modelled with one or multiple layers of solid (brick) elements. Usually with more layers of solid elements across height, only the three displacement components are used as the nodal degrees of freedom. If only one layer of solids is modelled across thickness, having more than 8 nodes per element is appropriate. The adhesive layer between the metal substrates is modelled with be means of zero-thickness interface elements with 8 nodes that correspond to nodes of the top and the bottom side of the adjacent brick elements. The three nodal degrees of freedom of the adjacent brick elements are used to compute the normal separation and two tangential sliding separations at the interface, which depends on the adopted TSL. The normal separations are related to mode I while the tangential components are related to delamination in modes II and III.

In the second approach, metal substrates are modelled with flat shell elements with six degrees of freedom per node, three nodal displacements, two cross-sectional rotations and possibly one drilling rotational degree of freedom. The number of nodes per element can vary from at least 3 for triangles, or at least 4 for quadrilaterals. More nodes are included if higher order elements are used. Usually, the number of nodes is chosen to correspond with the shared nodes of an interface element. The reference plane of shell elements is positioned at the mid-surface of each metal substrate. The zero-thickness interface element again has 8 nodes that now correspond to nodes of the adjacent shell elements. Note that the interface between two adjacent shell elements does not correspond to their reference planes. This is why for computing the relative displacements at the interface, besides the nodal displacements, nodal cross-sectional rotations and the distance from the interface and the reference plane have to be taken into account. The separation in mode I is calculated only as the difference in between transversal displacements of adjacent shell elements' nodes, as it does not depend on the nodal rotations and the distance between the reference plane and the interface [104]. On the other hand, the separation in mode

II is computed using shell nodal displacements in the horizontal directions, as well as nodal rotations and distances from the reference planes and the interface..

In a DCB experiment, the separation in mode I is dominant, while the presence of modes II and III is negligible and therefore neglected. This allows for simplifications in the numerical models. The general 3D numerical model can be reduced to a single plane and shell elements can be replaced with plate elements that have just three degrees of freedom per node. Only displacement transversal to the reference plane is required, along with two cross-sectional rotations per node. The interface element can be positioned in the same plane since plate transversal displacement is sufficient to compute the separation in mode I.

In conclusion, the first approach with solid (brick) elements will not be considered in this thesis since these elements require significantly more degrees of freedom in total compared to plate elements. For example, a layer modelled with 4-node quadrilateral plate element has 4 nodes and 12 degrees of freedom, while the solid element has 8 nodes and 24 degrees of freedom per each layer across thickness. This difference can increase even more if multiple layers of solid elements are used to model each layer, which can be required in some cases to maintain an acceptable aspect ratio of the elements. Therefore, it is self-evident that the second approach with the plate elements will be computationally more efficient [53].

The DCB experiment is symmetric with respect to the plane of the interface since in the experiments both metal substrates have the same thickness and material properties. Therefore, only half of the domain can be analysed in the numerical model. Further simplifications stemming from the regularity and uniformity of the nodal mesh lead to less computational time. This is due to constant Jacobian determinant and the lack of need for geometrical transformation matrices on the individual element in a model.

The moderately thick plate model according to the Mindlin plate theory (see Figure 4.1) is used to model the substrates. Mindlin plate finite elements have a certain advantage over Kirchhoff plate finite elements. Not only can they add shear strain energy with bending deformations to the total strain energy to form the total element stiffness matrix, but their lateral displacement and cross-sectional rotations can now be interpolated independently, while only the first derivatives of the interpolation functions are needed for strain expressions.

In this thesis, the plate finite element Q4U3 presented in [105] will be mainly used. In short, it involves cubic interpolation for transverse displacement and quadratic interpolation for the cross-sectional rotations (commonly called linked interpolation) resulting in constant shear along

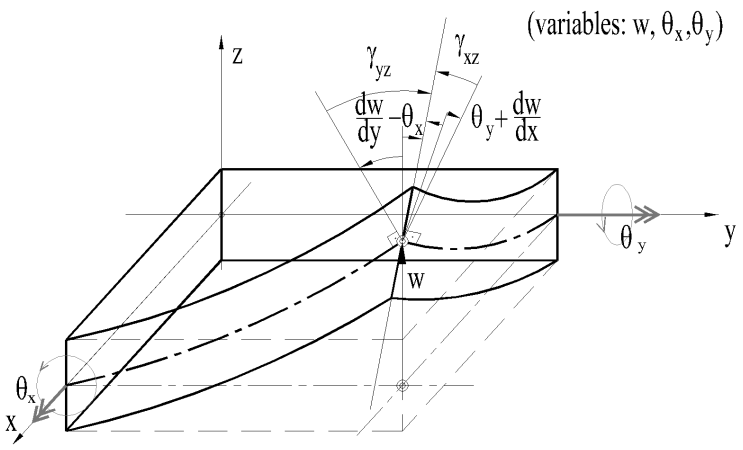

Figure 4.1: Mindlin plate element displacements, section rotations and shear strains (figure is adopted from [48])

the element edges. Such plate elements are displacement based elements, involving only nodal displacement and nodal cross-section rotations as the unknown parameters. The interpolation used in the plate elements is actually a 2D expansion of the formulation that gives an exact solution for the bending of shear deformable Timoshenko beam element exposed to concentrated force.

Furthermore, the Q4U3 finite element is problem dependent which means that material parameters are involved in its highest order terms of the interpolation functions. If the highest order terms are omitted, a quadratic form of the linked interpolation is obtained.

The governing equations for Kirchhoff and Mindlin plate theories are skipped here for the sake of brevity, but their kinematic, constitutive and equilibrium equations can be found in Appendix C.

4.1.1 Interpolation Functions

The displacement fields of Q4U3 plate element are interpolated by expanding the two node beam element interpolations that satisfy the Timoshenko beam differential equations. However, this formulation is not also an exact solution of the Midlin plate differential equations. The transverse displacement is interpolated by a cubic polynomial, which in the case of regular mesh reads

$$
\begin{aligned}
w = &\sum_{i=1}^{4} N_i w_i + \\
&\frac{1-\eta^2}{4}\frac{1-\eta}{2}\frac{1}{2}(\theta_{y2}-\theta_{y1})L_{12} - \frac{1+\xi}{2}\frac{1-\eta^2}{4}\frac{1}{2}(\theta_{x3}-\theta_{x2})L_{32} - \\
&\frac{1-\xi^2}{4}\frac{1+\eta}{2}\frac{1}{2}(\theta_{y3}-\theta_{y4})L_{34} + \frac{1-\xi}{2}\frac{1-\eta^2}{4}\frac{1}{2}(\theta_{x4}-\theta_{x1})L_{41} + \\
&\frac{1-\xi^2}{4}\frac{1-\eta^2}{4}w_{B,0} - \frac{\xi-\xi^3}{4}\frac{1-\eta}{2}\Delta\kappa_{12}\frac{L_{12}^2}{6} - \\
&\frac{1+\xi}{2}\frac{\eta-\eta^3}{4}\Delta\kappa_{23}\frac{L_{23}^2}{6} + \frac{\xi-\xi^3}{4}\frac{1+\eta}{2}\Delta\kappa_{34}\frac{L_{34}^2}{6} + \\
&\frac{\xi-\xi^3}{4}\frac{1+\eta}{2}\Delta\kappa_{14}\frac{L_{14}^2}{6} + \frac{\xi-\xi^3}{4}\frac{1-\eta^2}{4}\frac{1}{3}w_{B,3} + \\
&\frac{1-\xi^2}{4}\frac{\eta-\eta^3}{4}\frac{1}{3}w_{B,4} + \frac{\xi-\xi^3}{4}\frac{\eta-\eta^3}{4}\frac{1}{3}w_{B,5}
\end{aligned}
\tag{4.1}
$$

where element side curvatures between the nodes can be expressed using nodal unknowns, transversal displacement w_i and the two rotations of the plate sections $\theta_{x,i}, \theta_{y,i}$ around the local in plane coordinates, with $i = 1, 2, 3, 4$, as well as the plate material parameters as follows

$$
\Delta\kappa_{12} = -\left(w_2 - w_1 + \frac{\theta_{y1}+\theta_{y2}}{2}L_{12}\right)\frac{1}{1+\frac{12D}{L_{12}^2 Ghk}}\frac{6}{L_{12}^2} \tag{4.2}
$$

$$
\Delta\kappa_{23} = -\left(w_3 - w_2 + \frac{\theta_{y2}+\theta_{y3}}{2}L_{23}\right)\frac{1}{1+\frac{12D}{L_{23}^2 Ghk}}\frac{6}{L_{23}^2} \tag{4.3}
$$

$$
\Delta\kappa_{34} = -\left(w_4 - w_3 + \frac{\theta_{y3}+\theta_{y4}}{2}L_{34}\right)\frac{1}{1+\frac{12D}{L_{34}^2 Ghk}}\frac{6}{L_{34}^2} \tag{4.4}
$$

$$
\Delta\kappa_{41} = -\left(w_1 - w_4 + \frac{\theta_{y4}+\theta_{y1}}{2}L_{41}\right)\frac{1}{1+\frac{12D}{L_{41}^2 Ghk}}\frac{6}{L_{41}^2} \tag{4.5}
$$

where L_{ij} are the lengths of the element sides between the neighbouring nodes $i = 1, j = 2$. The material parameters are the plate bending rigidity $D = Eh^3/12(1-\nu^2)$, plate thickness h, shear modulus G, modulus of elasticity E, Poisson ratio ν and shear correction coefficient k.

The internal bubble degrees of freedom $w_{B,i}$ complete the cubic coefficients for transversal displacement in the 2D form of the Pascal's triangle of combinations of variables ξ, η. In particular, internal bubble parameters for displacement field $w_{Bb,0}, w_{Bb,3}, w_{Bb,4}, w_{Bb,5}$ complete the cubic interpolation polynomials. Interesting to note is that they do not have any effect on the displacement field on the element sides and the internal degrees of freedom are statically

condensed in the process of element stiffness matrix formation. This means that only four displacements w_i and eight nodal rotations θ_{xi} and θ_{yi} are the external degrees of freedom for each plate element. The Q4U3 passes the constant bending stress condition on the standard patch test of five elements [105].

The rotations of plate sections are interpolated with the quadratic polynomials in the following manner

$$\begin{aligned}\theta_x = &\sum_{i=1}^{4} N_i \theta_{xi} \\ &- \frac{1-\xi^2}{4}\frac{1-\eta}{2}\Delta\kappa_{12}(y_2-y_1) - \frac{1+\xi}{2}\frac{1-\eta^2}{4}\Delta\kappa_{23}(y_3-y_2) \\ &- \frac{1-\xi^2}{4}\frac{1+\eta}{2}\Delta\kappa_{34}(y_4-y_3) - \frac{1-\xi}{2}\frac{1-\eta^2}{4}\Delta\kappa_{41}(y_1-y_4) \\ &- \frac{1-\xi^2}{4}\frac{1-\eta^2}{4}\theta_{Bb,1}\end{aligned} \tag{4.6}$$

$$\begin{aligned}\theta_y = &\sum_{i=1}^{4} N_i \theta_{yi} \\ &- \frac{1-\xi^2}{4}\frac{1-\eta}{2}\Delta\kappa_{12}(x_2-x_1) - \frac{1+\xi}{2}\frac{1-\eta^2}{4}\Delta\kappa_{23}(x_3-x_2) \\ &- \frac{1-\xi^2}{4}\frac{1+\eta}{2}\Delta\kappa_{34}(x_4-x_3) - \frac{1-\xi}{2}\frac{1-\eta^2}{4}\Delta\kappa_{41}(x_1-x_4) \\ &- \frac{1-\xi^2}{4}\frac{1-\eta^2}{4}\theta_{Bb,2}\end{aligned} \tag{4.7}$$

Internal bubble parameters in the rotation fields $\theta_{Bb,1}, \theta_{Bb,2}$ complete the quadratic interpolation polynomials. Once more, these bubble parameters satisfy the conformity of the element and they can be statically condensed on the element stiffness matrix level.

Formulation of the element stiffness matrix follows the standard principles given in textbooks [46]. Total energy of the system and the stationarity condition for the total potential energy leads to the global stiffness matrix, which must also include the contribution from the interface elements.

4.2 Interface Elements

In a cohesive zone model, a non-linear relationship is introduced between the relative displacements at the interface and the corresponding tractions. Interface surfaces are able to lose co-

hesion and separate from one another as the interface traction approaches zero. At first, the material behaves elastically, as it would in a linear calculation, but after reaching the maximum traction it can sustain, softening at the interface takes place. A slightly modified approach, known as damage mechanics, is needed to realistically simulate reloading. This requires the use of secant stiffness (green line in Figure 4.2) instead of tangent stiffness, which means that the material damage is irreversible, as well as the damage history variable that saves the value of maximum separation. The relationship between interface traction and separation is called traction-separation law (TSL).

The area under the curve of TSL (see Figure 4.2) is by definition equivalent to the critical energy release rate G_C. Other TSL parameters such as initial stiffness, maximum traction (maximum stress) and maximum elongation might be adopted from mechanical experiments on bulk specimens but this is for the most part neither practical nor reliable. Size effect and change of stress state result in different behaviour of the material in bulk specimen and thin layered interface. The choice of initial stiffness is unclear as well, although its influence on simulation has been well studied. When the initial (penalty) stiffness tends to infinity, the model will reproduce the results of LEFM. The pre-crack behaviour is mainly governed by this parameter, with higher values of initial stiffness corresponding to the higher values of the peak force. After the crack propagation, high value of initial stiffness will be particularly detrimental to the computational efficiency [30, 55] of the finite element simulation.

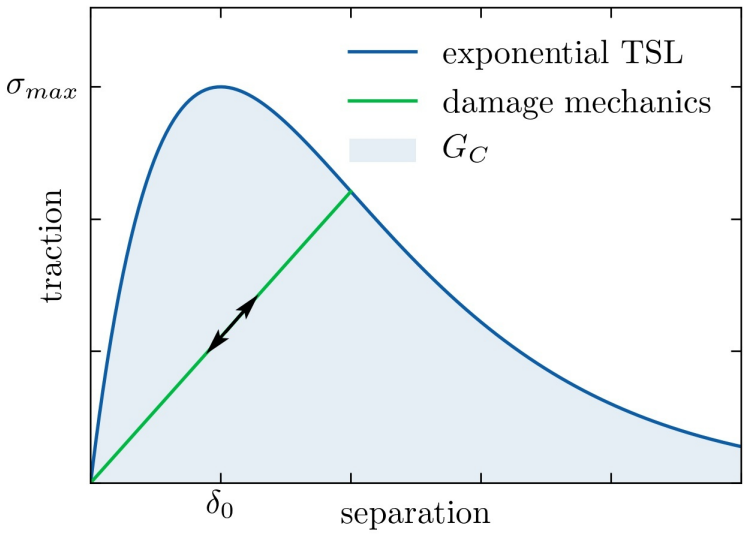

Figure 4.2: Exponential traction-separation law

Similar to real experiments, numerical simulation uses the displacement control to capture the drop of the applied load during crack propagation caused by a continuous opening of the

DCB arms. Applied displacement is incrementally increased and for each increment the solver iterates until the problem converges, i.e. residual approaches zero. Delamination simulations often suffer from spurious oscillations [30] in the form of sharp snap-throughs and snap-backs in the structural response (the latter cannot be captured using the displacement control). Those are key indicators of computational issues in terms of the convergence rate of a particular mesh and interface parameters. Higher ductility [55] of the interface parameters and mesh refinements are the simplest ways to improve convergence.

Large variation of interface stiffness often occurs between the two iterations of the solution procedure which leads to problems with convergence. This can be due to the inherent material properties of the brittle interface. Even the relatively ductile interfaces can have issues when the damage mechanics approach is applied since the secant stiffness is substantially smaller than tangent stiffness. Change between the two regularly happens during the iterations within a single increment. Obviously, having a smaller displacement increment will improve the solution robustness but at the cost of computational time.

Mesh refinement near the crack front will lead to a smoother structural response in the load-displacement results. However, given that the crack front is moving throughout the simulation, mesh density has to be high enough throughout the expected path of crack propagation. According to the literature [55], in order to properly model the delamination, the damage process zone should have a few [106] or several [102] elements along the cohesive zone length. Therefore, it is challenging to have a relatively sparse mesh while achieving a convergence of the solution procedure.

The described procedure uses iterative minimization of the global vector of residual forces. First it checks the energy norm and then the residual force norm. In addition, the numerical integration rule (Gauss or Simpson [47]) may also influence the robustness and convergence rate of the solution.

Furthermore, the type of chosen finite element to model the substrates influences the result, as reported in [49]. Advanced solution procedures, such as the arc-length method [30], can significantly improve convergence of the delamination simulation. It has been found that the choice of interface TSL [49] can have a strong influence on the convergence, which will be evident from the results in the section 4.3.

Consider a thin interface connecting two adjacent layers. Its thickness is so small that it can be neglected in comparison to the dimensions of the entire problem. These are called zero-

thickness interface elements since two neighbouring nodes coincide before the deformation takes place. To model the mode I delamination, TSL should be defined in both the opening and closing separation. The latter corresponds to compression and is needed to avoid penetration. Even though the DCB test does not suffer from numerical problems with penetration, compressional forces are also needed for equilibrium, i.e. producing the force couple in front of the crack tip.

4.2.1 Interpolation Functions

To model delamination in mode I, interface separation with only one component is sufficient. The direction of this separation corresponds to that of the transversal displacements of the plates used to model the substrates. Since the transversal displacement of the Q4U3 plate element is interpolated with the fully populated 2D cubic field, it is physically correct to replicate this field on the connected interface element. If the plate displacement is expressed with a quadratic interpolation, the interface interpolation should replicate it too. The quadratic interpolation for interface element is continuously conformed with the plate element that has quadratic interpolation, or conformed only at the element nodes if the cubic interpolation for the plate element is used.

However, the cubic interpolation has not delivered significant improvement in accuracy over the quadratic interpolation [104] in the preliminary case study with beam substrates. In the examples considered in this thesis, quadratic interpolation still performs better than the standard linear one. Therefore, the quadratic expression is used in this thesis exclusively. The displacement field of eight-node interface (INT8) is interpolated by a quadratic expression in a kinematically compatible way

$$\begin{aligned}\delta_I =& \frac{1-\xi}{2}\frac{1-\eta}{2}(w_5-w_1)+\frac{1+\xi}{2}\frac{1-\eta}{2}(w_6-w_2)+\\ &\frac{1+\xi}{2}\frac{1+\eta}{2}(w_7-w_3)+\frac{1-\xi}{2}\frac{1+\eta}{2}(w_8-w_4)+\\ &\frac{1-\xi^2}{4}\frac{1-\eta}{2}\frac{(\theta_{y6}-\theta_{y5})-(\theta_{y2}-\theta_{y1})}{2}L_x-\\ &\frac{1+\xi}{2}\frac{1-\eta^2}{4}\frac{(\theta_{x7}-\theta_{x6})-(\theta_{x3}-\theta_{x2})}{2}L_y+\\ &\frac{1-\xi^2}{4}\frac{1+\eta}{2}\frac{(\theta_{y8}-\theta_{y7})-(\theta_{y4}-\theta_{y3})}{2}L_x-\\ &\frac{1-\eta}{2}\frac{1-\eta^2}{4}\frac{(\theta_{x5}-\theta_{x8})-(\theta_{x1}-\theta_{x4})}{2}L_y\end{aligned} \tag{4.8}$$

where $L_x = L_{12} = L_{34}$ and $L_y = L_{23} = L_{41}$ in the present case of regular mesh. Nodes of the

plate finite elements are typically located at the midplane and accordingly the interface element shares these nodal position, as depicted in Figure 4.3. The quadratic interpolation depends not only on the transversal displacement of $4 + 4$ adjacent plate nodes, but also on two rotations around the plate's in-plane coordinate axes. This linked interpolation ensures the kinematic compatibility at shared nodes [53]. Note that no bubble degrees of freedom are used in Equation (4.8).

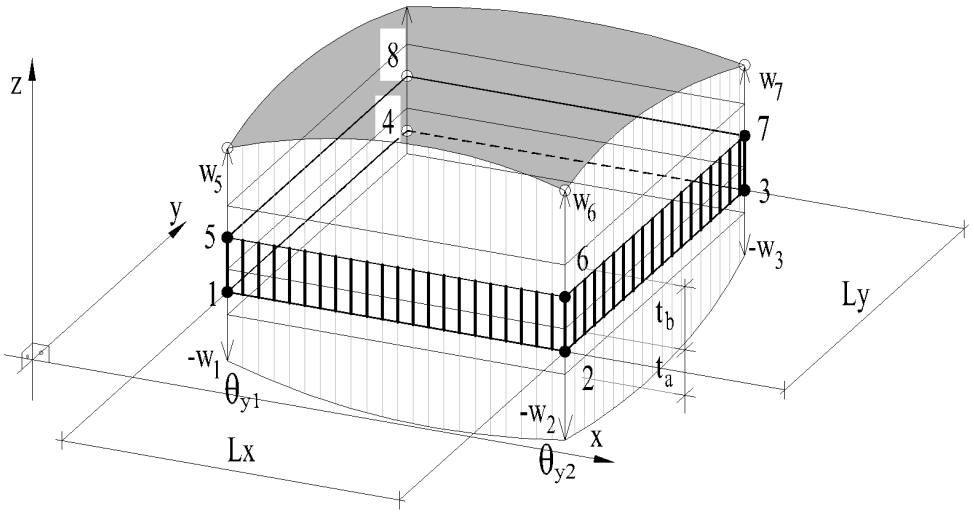

Figure 4.3: Interface INT8 degrees of freedom

To derive the stiffness matrix of the interface, the internal virtual work of every element is defined by the integral

$$V_{int} = \int_A \bar{\delta_I} \sigma_I dA = \int_{-1}^{+1} \int_{-1}^{+1} \bar{\delta_I} \sigma \frac{L_x L_y}{4} d\xi d\eta \tag{4.9}$$

with virtual relative displacements (separations) at the interface denoted as $\bar{\delta_I}$, while the corresponding stress (traction) is denoted as σ_I. The virtual displacements are interpolated in the same way as the real ones, that is in terms of 8 nodal virtual displacement $\bar{w_i}$ and 16 nodal virtual rotations $\bar{\theta_{xi}}, \bar{\theta_{yi}}$ (i=1,2,...8).

From (4.8), δ_I is expressed in terms of the nodal degrees of freedom,

$$\delta_I = \bar{\delta_I} = \sum_{i=1}^{24} N_i \cdot \delta_{I,i} = \boldsymbol{N^T} \cdot \boldsymbol{\delta_I} \tag{4.10}$$

where $\boldsymbol{N}$ is a vector of all individual interpolation functions derived from (4.8) and $\boldsymbol{\delta_I^T}$ is equal to

$$\boldsymbol{\delta_I^T} = \{w_1, \theta_{x1}, \theta_{y1}, w_2, \theta_{x2}, \theta_{y2}, ...w_8, \theta_{x8}, \theta_{y8}\} \tag{4.11}$$

which leads to internal virtual work

$$V_{int} = \boldsymbol{\delta_I^T} \cdot \int_A \boldsymbol{N^T} \cdot \boldsymbol{\sigma}(\delta_I) \cdot dA \cdot \boldsymbol{\delta_I} = \boldsymbol{\delta_I^T} \cdot \boldsymbol{K}(\delta_I) \cdot \boldsymbol{\delta_I} \tag{4.12}$$

and stiffness matrix of the interface

$$\boldsymbol{K}(\delta_I) = \int_{-1}^{+1} \int_{-1}^{+1} \boldsymbol{N^T} \cdot \boldsymbol{\sigma}(\delta_I) \cdot \frac{L_x L_y}{4} \cdot d\xi d\eta = \sum_{N_{GP}} \boldsymbol{N^T}(GP) \cdot \boldsymbol{\sigma}(\delta_I(GP)) \cdot w_{GP} \cdot \frac{L_x L_y}{4} \tag{4.13}$$

Integration is performed through the chosen number of Gauss points (N_{GP}), with w_{GP} denoting the weight value at GP and L_x, L_y denoting the lengths of the rectangular element sides. It turns out that 3 by 3 Gauss points are sufficient for the numerical stiffness calculation.

The tangent stiffness matrix of the interface element can be obtained and computed for every displacement control increment in a DCB experiment simulation. Since the relation between σ_I and δ_I is not linear, the residual forces have to be calculated during each increment step by multiplying the stiffness matrix with the actual separation value δ_I. Traction is calculated for a given separation according to the chosen TSL law described hereafter.

4.2.2 Traction-Separation Law

Traction-separation law can have various shapes, such as bi-linear, trapezoidal, exponential, etc. This thesis will describe the constitutive law of the INT8 interface element by either exponential [32] or bi-linear [104] TSL. General comparison between the two is shown on Figure 4.4. For the sake of simplicity, the subscript "$_I$" denoting mode I direction shall be omitted so that $\delta_I = \delta$ and $\sigma_I = \sigma$, while the $G_{IC} = G_C$.

The required parameters of a **bilinear** mode-I TSL are $\sigma_{MAX}, \delta_0, \delta_C$, with the area under the curve equal to fracture toughness G_C. Stiffness (or penalty stiffness) is simply

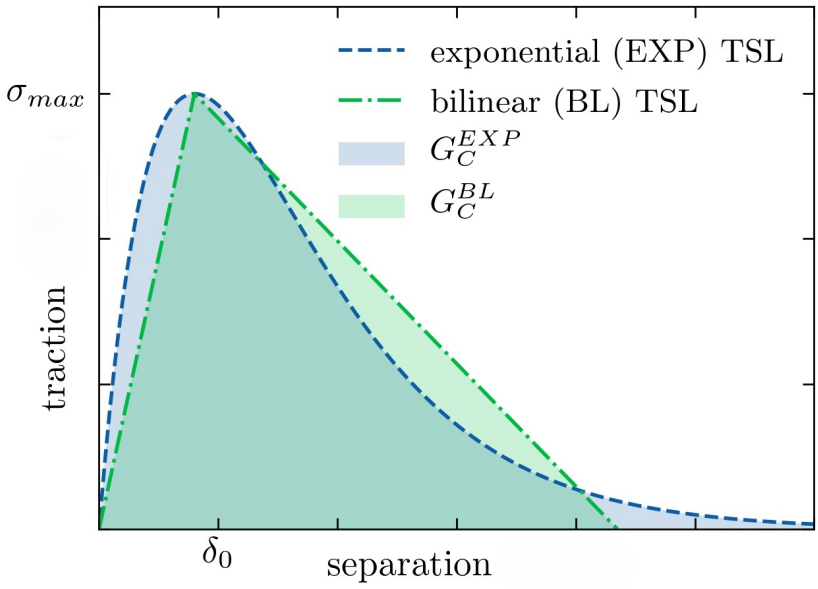

Figure 4.4: Exponential vs bilinear TSL

$$K = \frac{\sigma_{MAX}}{\delta_0} \tag{4.14}$$

which is used to describe the the linear behaviour of the interface. After reaching the peak traction, softening will ensue and stiffness will be reduced to a negative value

$$K_S = -\frac{\sigma_{MAX}}{\delta_C - \delta_0} \tag{4.15}$$

This happens after separation surpasses the characteristic length δ_0. Going further, separation will at one point exceed the critical separation δ_C after which the traction completely vanishes. Therefore, the bilinear TSL can be expressed in the following manner

$$\sigma = \begin{cases} K\delta & 0 < \delta < \delta_0 \\ K\delta_0 + K_S(\delta - \delta_0) & \delta_0 < \delta < \delta_C \\ 0 & \delta_C < \delta \end{cases} \tag{4.16}$$

where K and K_S represent the initial and softening stiffness, respectively.

TSL parameters were retrieved from experiments performed on narrow DCB tests (see Section 3.4). Exponential and bilinear laws depicted in Figure 4.4 have a matching fracture toughness G_C so that the comparison between the two can be as fair as possible. However, the characteristic length δ_0 also matches, which lowers the initial (penalty) stiffness K of bilinear law compared to

exponential TSL, consequently increasing the ductility (and convergence capabilities) of bilinear TSL. In fact, the bilinear TSL maximum traction σ_{MAX} and the corresponding displacement δ_0 matches with those of the exponential TSL.

4.2.3 Derivation of Exponential TSL

Exponential law used here is equivalent to Xu and Needleman's mixed mode law [31] but for present application, where only mode I is sufficient, TSL can be defined as

$$\sigma(\delta) = \frac{G_C}{\delta_0^2} \cdot \delta \cdot e^{-\frac{\delta}{\delta_0}} \tag{4.17}$$

$$K(\delta) = \frac{G_C}{\delta_0^2} \cdot e^{-\frac{\delta}{\delta_0}} \cdot (1 - \frac{\delta}{\delta_0}) \tag{4.18}$$

where the latter equation (4.18) is an expression for TSL stiffness. A detailed derivation of the above expressions is given hereafter. The general form of exponential TSL in mode I can be assumed as follows

$$\sigma(\delta) = a\delta \cdot e^{-b\delta} \tag{4.19}$$

where the traction is denoted as σ and the separation as δ, while a and b are parameters to be determined. Maximum value of traction σ_{MAX} will occur at separation value δ_0, also known as the characteristic length. This condition can be written as

$$\sigma'(\delta = \delta_0) = ae^{-b\delta} \cdot (1 - b\delta) = 0 \tag{4.20}$$

where the right-hand part in parenthesis leads to a solution for the second parameter

$$b = \frac{1}{\delta_0} \tag{4.21}$$

First parameter is found by substituting now determined second parameter b in the expression for traction

$$\sigma_{MAX} = \sigma(\delta_0) = \frac{a}{b \cdot e} \tag{4.22}$$

$$a = \frac{\sigma_{MAX}}{\delta_0} \cdot e \tag{4.23}$$

In cases where it is more appropriate, the parameter a can also be expressed in terms of initial

slope (stiffness) K_0 of the traction-separation curve

$$K_0 = \sigma'(\delta = 0) = a \cdot e^{-b\delta} \cdot (1 - b\delta) \tag{4.24}$$

$$a = K_0 \tag{4.25}$$

This gives two TSL expression, one with the maximum traction and the corresponding separation, and the second with initial stiffness and characteristic separation, respectively

$$\sigma(\delta) = \sigma_{MAX} \cdot \frac{\delta}{\delta_0} \cdot e^{1-\frac{\delta}{\delta_0}} \tag{4.26}$$

$$\sigma(\delta) = K_0 \cdot \delta \cdot e^{-\frac{\delta}{\delta_0}} \tag{4.27}$$

After the onset of crack propagation, the J integral is typically [11] equivalent to the fracture toughness G_C,. At this point, the integral of the area under the TSL curve can be expressed to introduce the principal material parameter, namely the fracture toughness

$$\begin{aligned}
G_C &= \int_0^\infty \sigma(\delta) d\delta \\
&= \int_0^\infty a\delta e^{-b\delta} d\delta \\
&= -\frac{a}{b} \int_0^\infty \delta d\left(e^{-b\delta}\right) \\
&= -\frac{a}{b} \left(\delta e^{-b\delta} \Big|_0^\infty - \int_0^\infty e^{-b\delta} d\delta \right) \\
&= -\frac{a}{b} \left(0 - 0 + \frac{1}{b} e^{-b\delta} \Big|_0^\infty \right) \\
&= -\frac{a}{b} \left(-0 - \frac{1}{b} \right) \\
&= \frac{a}{b^2} \\
&= e\sigma_{MAX}\delta_0
\end{aligned} \tag{4.28}$$

which when substituted in Eq.(4.26) leads to the definition of TSL and the corresponding J integral using the fracture toughness and characteristic length in the following way

$$\sigma(\delta) = \frac{G_C}{\delta_0 e} \cdot \frac{\delta}{\delta_0} \cdot e^{1-\frac{\delta}{\delta_0}} = \frac{G_C}{\delta_0^2} \delta e^{-\frac{\delta}{\delta_0}} \tag{4.29}$$

$$J_{INT} = \int \sigma(\delta) d\delta = \frac{G_C}{e}[e - e^{1-\frac{\delta}{\delta_0}} \cdot (\frac{\delta}{\delta_0} + 1)] = G_C[1 - e^{-\frac{\delta}{\delta_0}}(\frac{\delta}{\delta_0} + 1)] \tag{4.30}$$

Equation (4.29) is actually equivalent to the coupled exponential cohesive zone law of Xu and Needleman [31] either with their coupling parameters $r = q = 1$ or separation in mode II $\delta_{II} = 0$. Their solution was derived using an energy based approach. For the purpose of coding the material law in the framework of finite elements, the additional requirement may be the stiffness (penalty) function obtained from derivation of Equation (4.29)

$$K(\delta) = \frac{G_C}{\delta_0^2} e^{-\frac{\delta}{\delta_0}} \left(1 - \frac{\delta}{\delta_0}\right) \tag{4.31}$$

Presented derivation was able to reproduce well-known TSL [31,32]. Even though this thesis only considers the opening mode I, in a similar manner the mode II expression should have been derived since even the improved expression from the literature [32] is slightly inelegant with characteristic length in mode II defined as $\delta_0^{II}/\sqrt{2}$ instead of simply δ_0^{II}.

4.2.4 Simple Identification of Exponential TSL Parameters

The first parameter needed for the exponential TSL is obtained from the R-curve, i.e. values of the fracture variation not only at the initial crack but across the entire interface, by considering the average value. The other parameter required for the exponential TSL is the characteristic length, i.e. interface separation δ_0 at maximum traction. This section considers the dependency of characteristic length might on the thickness of adhesive thin layer.

The underlying assumption made in the numerical simulations that the exponential curve can describe real behaviour of the interface is also adopted for parameter identification. Furthermore, one can assume **stiffness** K up to $\sigma(\delta_0) = \sigma_{MAX}$ as completely linear with the **secant modulus** of elasticity. Size effects on material properties are typically explained statistically as a higher chance of a defect when the size of a body is larger. In the case of elastic modulus, the size effect influence has been reported both with stiffening and softening effect, implying that the influence is minor [107] and that shape effects may be as much important. In any case, of all the TSL material properties, stiffness is the one that is most comparable for bulk and thin layer material [44]. The newly proposed simple identification assumes the applicability of the Hooke's law to thin adhesive layer

$$\sigma_{MAX} = E\frac{\Delta l}{l} = E'_A\frac{\delta_0}{t_A} \tag{4.32}$$

where the effective stiffness of the adhesive reads

$$E'_A = \frac{E_A}{1-\nu^2} \tag{4.33}$$

Recall Equation (4.28) derived for the exponential TSL, in which Equation (4.32) can be inserted

$$G_C = \sigma_{MAX} \cdot \delta_0 \cdot e = \frac{E'_A}{t_A} \cdot \delta_0^2 \cdot e \tag{4.34}$$

Rearranging the above equation leads to the following characteristic separation definition

$$\delta_0 = \sqrt{\frac{G_C \cdot t_A}{e \cdot E'_A}} \tag{4.35}$$

This simple approach (4.35) to TSL prediction may be a useful approximation in cases when direct identification or inverse methods are not available or desirable. Since the second parameter of exponential TSL (δ_0 or σ_{MAX}) significantly affects structural force-displacement response only near the peak force, it is more appropriate to test the validity of the proposed approach only in the terms of error in the σ_{MAX}. The approach will be tested against direct identification approach, either with the Savitzky-Golay approach from Section 3.4 or with the nonlinear exponential best fit from Appendix B. Recall how the experimental precision of displacement measurements was of the order of 1 micron. Given how the identified characteristic length is about 4 microns in the presented case of direct identification (see 3.4), the reasonable precision of simple identification approach is also 25 percent. The margin of error for peak traction is harder to estimate, but can be assumed the same.

The peak traction σ_{MAX} can be estimated from the same assumptions (Equations 4.32 and 4.35). It will depend on the same parameters as the characteristic length in Equation 4.35, namely modulus of elasticity, (average) fracture toughness and adhesive layer (average) thickness.

$$\sigma_{MAX} = \sqrt{\frac{G_C \cdot E'_A}{e \cdot t_A}} \tag{4.36}$$

The validity of the proposed approach is tested using the data from experiments presented

in Section 3.4, which is shown in Figure 4.5. It can be noticed that the predictions and the experimentally determined values of the peak traction show a rather good agreement. This seems quite surprising given the simplicity of the presented approach. The prediction underestimates the peak traction by 28 % on average. An additional validity check is performed using data from literature [108], which is presented separately in Appendix D with the purpose of verifying the proposed method of identification.

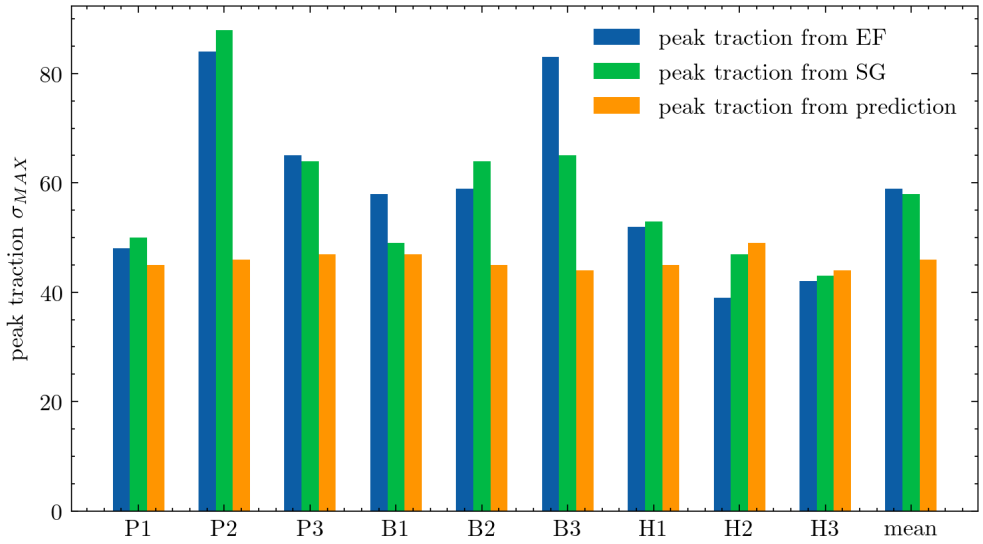

Figure 4.5: Validity test of Simple Identification by comparison with direct identification (abbreviations: EF - exponential fit, SG - Savitsky-Golay)

The above-presented case studies may be a mere coincidence, instead of a general rule, and not replicable for a different interface material. For example, actual TSL may have an arbitrary shape that is not well described by the exponential law. However, an increase in adhesive thickness causes a decrease in peak traction [108], and this trend is adequately modelled by Equation (4.36), as depicted in Figure 6.8 of Appendix D.

For present thesis, expression (4.36) will be utilised exclusively for predicting the second parameter of plate-like specimens since their geometry is inappropriate for direct identification that relies on edge measurements. Wider specimens described in section 3.5 had a thicker layer of adhesive which, according to Equation (4.36), translates to lower peak traction. Likewise, if the layer adhesive thicknesses of specimens S1 and S2 are related as $t_A^1 < t_A^2$, TSL correction based on Equation (4.35) suggest that $\delta_0^{S1} < \delta_0^{S2}$, or in general

$$\delta_0^{S2} = \delta_0^{S1} \cdot \sqrt{\frac{t_A^{S2}}{t_A^{S1}}} \tag{4.37}$$

With the above correction, better simulation of numerical load-displacement response near the peak load (see Section 5.1) will be achieved for specimens A60 and A120 with their characteristic lengths corrected via Equation (4.37) to δ_0^{A60}= 0.0065 mm and δ_0^{A120}= 0.0075 mm. In a similar manner, the critical separation is corrected for analysiss in Section 5.2 by expression

$$\delta_C^{S2} = \delta_C^{S1} \cdot \sqrt{\frac{t_A^{S2}}{t_A^{S1}}} \tag{4.38}$$

which leads to critical separations δ_C^{A60}= 0.010 mm for specimens A60 and δ_C^{A120}=0.012 mm for specimens A120. Note that these values were not previously used in Figures 3.22-3.24.

4.3 Numerical Studies

The numerical convergence on DCB test is studied for both the exponential (4.29) and bilinear (4.16) TSL, as well as linked (quadratic) and linear interpolation functions for the displacement and rotations used in the interface elements. The geometrical and material properties used match those of the specimen A (see Table 4.1) but with the characteristic length $\delta_0 = 0.005$ mm (value before applying corrections from section 4.2.4). The numerical simulations were performed utilising symmetry by modelling only the upper half of the DCB test, while the displacement control increments were 0.1 mm up to ultimate 10.0 mm half-displacement.

length/width/height $L/B/h$	TSL parameters $\delta_0/\sigma_{MAX}/G_{IC}$
250/120/8 mm	0.005 mm/ 122 MPa/ 1.66 N/mm2

Table 4.1: Geometrical and material properties used for numerical studies

Mesh density was varied to find the computationally least demanding mesh size for every combination of TSLs and interpolation functions. Plate finite element Q4U3 is used in the present analysis to model the aluminium (E=70 GPa, ν=1/3). Results for considered combinations in terms of computational cost and convergence ability are presented in Table 4.2. Abbreviation N/A (not available) signals that the computation did not converge in all prescribed increments. The present study suggests that the combination of the exponential TSL and quadratic (linked) interpolation is the most robust since convergence was achieved even for the two coarsest meshes considered, namely 5.00 x 5.00 mm and 6.25 x 6.00 mm. Significant spurious oscillations were observed at these meshes, which may be interpreted as a sign of robustness (it converges although the mesh is obviously too coarse to give a smooth numerical response).

FE size # **of FE**	**6.25x6.00 mm** **1440 elements**	**5.00x5.00 mm** **2160 elements**	**2.50x2.50 mm** **8640 elements**	**1.25x1.25 mm** **34560 elements**
EXP TSL **QUAD int.**	56 s (1 min) 2036 iterations	113 s (2 min) 2294 iterations	297 s (5 min) 707 iterations	3089 s (51 min) 690 iterations
EXP TSL **LIN int.**	N/A	N/A	300 s (5 min) 716 iterations	3125 s (52 min) 703 iterations
BL TSL **QUAD int.**	N/A	N/A	N/A	3257 s (54 min) 684 iterations
BL TSL **LIN int.**	N/A	N/A	293 s (5 min) 716 iterations	3576 s (60 min) 703 iterations

Table 4.2: Computational cost of different TSL variants (abbreviations: EXP - exponential, BL - bilinear, QUAD - quadratic, LIN - linear, FE- finite element, int. - interpolation)

Interesting to note is how the quadratic (linked) interpolation, unlike the linear one, lost convergence for bilinear law at 2.50x2.50 mm mesh (see Figure 4.6). Specifically, convergence was lost at 1.2 mm prescribed displacement, which roughly corresponded to the beginning of crack propagation at 12% of simulation. This is an unexpected result since the bilinear TSL with quadratic (linked) interpolation generally displayed better convergence in the previous study with Timoshenko beam elements [104], along with the lower computational cost (as is replicated by the present study). Therefore, an inferior performance of the quadratic interpolation in the case of bilinear law shown in Table 4.2 may only be a numerical coincidence. In terms of computational cost, the required simulation time is comparable for specific mesh regardless of the considered interface, although the total number of iterations favours the linked quadratic interpolation formulation by a small margin, as shown in Table 4.2.

The most robust combination, that is exponential TSL with linked quadratic interpolation, requires a lower number of total iterations for mesh size 6.25x6.00 mm than for 5.00 x 5.00 mm, which arguably may be attributed to element length 6.25 mm that roughly matches the DPZ size. Furthermore, for these two demanding meshes, the increment cutting scheme embedded in the FEAP program [103] was utilised. However, when other considered combinations of TSLs and interpolation functions encountered too many retries, reducing the increment size did not help with convergence. This procedure of automatic pseudo-time cutting decreases or increases the step size as follows, respectively

$$\Delta t_{new} = min\left(\Delta t_{max}, 10^{\log((\Delta t_{old})+0.2}\right) \tag{4.39}$$

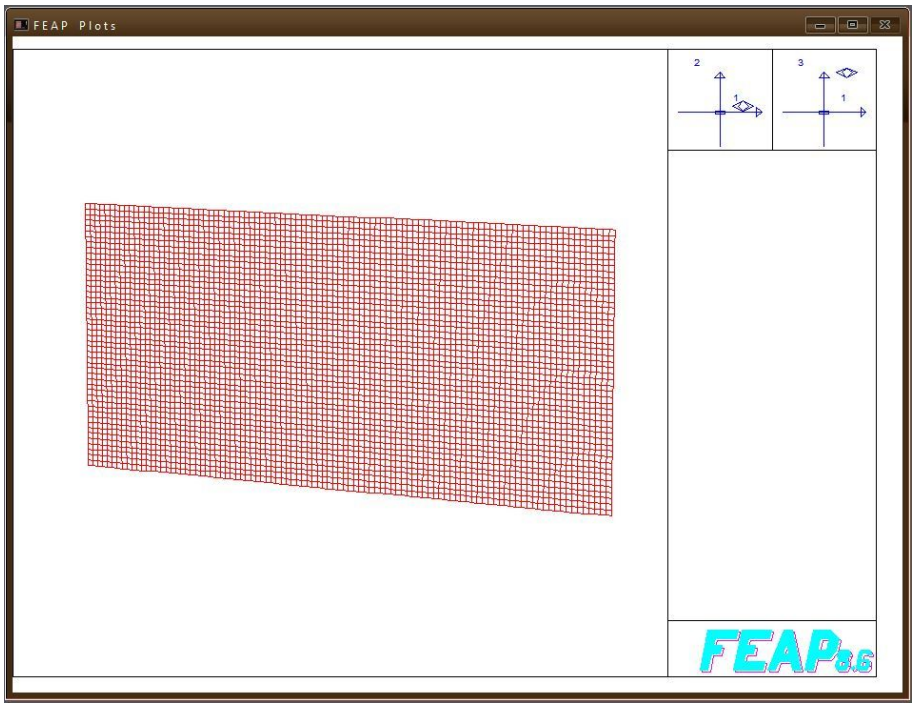

Figure 4.6: DCB test rectangular 2.50 x 2.50 mm mesh (Note that actual mesh is indeed regularly rectangular and any deviation from it is caused by FEAP's lack of antialiasing implementation)

$$\Delta t_{new} = max\left(\Delta t_{min}, 10^{\log((\Delta t_{old})-0.2}\right) \tag{4.40}$$

where Δt_{old} is the pseudo-time increment before the cutting scheme, Δt_{new} is the pseudo-time increment after the cutting scheme, and $\Delta t_{max}, \Delta t_{min}$ are the defined minimum and maximum pseudo-time increments. The simulation is started with a pseudo-time increment Δt that increases the displacement by 0.1 mm in each pseudo-time step.

The smoothness of the structural force-displacement response is shown in Figure 4.7. As mentioned earlier, spurious oscillations are present only for demanding meshes at which the bilinear law is not suitable. Therefore, the smoothness of the curve is not a distinct factor for given (undemanding) meshes and scale of magnification in Figure 4.7. The previous study [49] points to a slightly smoother response in the case of exponential law, which was also reproduced in preliminary numerical tests made for this thesis.

The following examples will be performed with previously best performing interface, namely the exponential TSL with linked quadratic interpolation. The plate finite element used in the previous examples, namely Q4U3, is now compared to FEAP's [103] original mixed formulation element named Q4-LIM [109]. The element Q4-LIM uses a quadratic level of linked interpolation for transversal displacements but has a mixed formulation with linear interpolation of shear

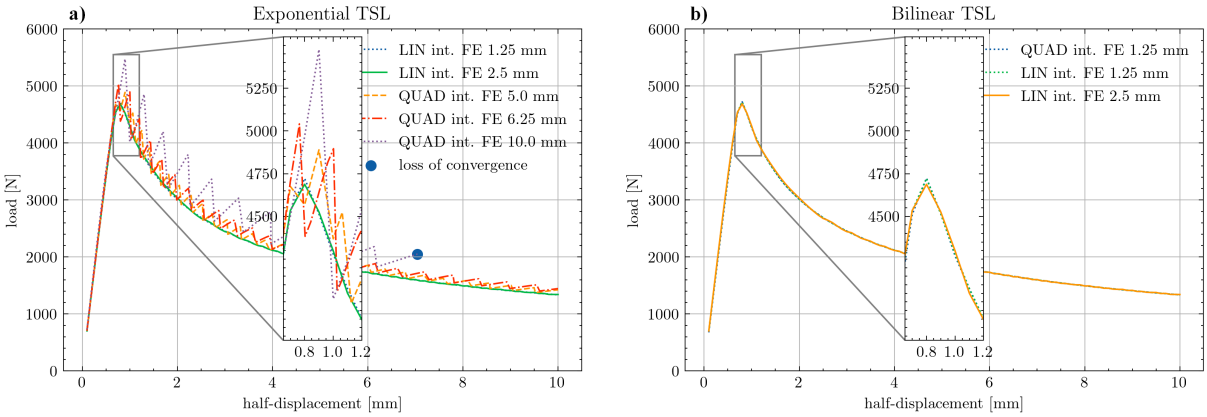

Figure 4.7: Smoothness of force-displacement response for various interfaces: a) exponential TSL, b) bilinear TSL (abbreviations: QUAD - quadratic, LIN - linear, FE- finite element, int. - interpolation)

strain. Comparison was made in terms of efficiency, either by examining computational time or the required number of iterations. Even though both elements are originally derived for the Mindlin theory, it is convenient to test them in the limit case, i.e. when they approach the Kirchhoff theory, by assigning a very high value of the shear stiffness. Reason for the introduction of Kirchhoff's limit case is evident after examining the numerical results in Table 4.3 that are made for mesh 2.50 x 2.50 mm.

Plate FE	Computational time	No. of iterations	Peak force
Q4U3 (Mindlin)	293 sec	707	4690.7 N
Q4-LIM (Mindlin)	267 sec	704	4690.6 N
Q4U3 (Kirchhoff)	251 sec	606	4811.5 N
Q4-LIM Kirchhoff)	218 sec	566	4823.7 N

Table 4.3: Computational cost of different plate formulations

Accounting for the shear strain significantly increased computational cost in both cases, and for more demanding meshes may introduce problems with oscillations or even loss of convergence. Actually, this was also noticed for other configurations, for example in the preliminary numerical model with nonlinear spring interface elements attached to a plate [110].

Russo and Chen [54] reported deflection of the substrate having high compression-tension oscillations ahead of the cohesive zone. They suggested accounting for the shear strain as a possible solution to these inaccuracies. This behaviour is indeed fixed by the inclusion of shear strain [104], but unfortunately new problems with convergence arise since this inclusion also introduces a discontinuity in cross-sectional rotations ahead of the cohesive zone, which may be the cause of higher computational cost.

Computational cost show the benefits of Q4-LIM element over the Q4U3 on the considered mesh in Table 4.3. However, the reduction of mesh density reveals the robustness of the Q4U3 in comparison with the **Q4-LIM**. The latter **does not converge** at more demanding meshes 5.00x5.00 mm and 6.25x6.00 mm, reaching only 39 % and 37 % of prescribed displacement, respectively. In conclusion, the Q4U3 plate elements in conjunction with interface exponential TSL with quadratic (linked) interpolation seems to be the best choice among all considered combinations. The model is almost able to converge in all prescribed increments at mesh 10.00x10.00 mm (see Figure 4.7), which is larger than the DPZ, and in this way overcome the cohesive zone limit [54].

4.4 Virtual Experiments

In order to validate the Symmetry Based Top Surface Analysis (SBTSA) method along with the Area method (see Section 3.5.2), virtual experiments were performed, in which the output from the numerical model (synthetic data) was used to test the proposed method. Input data for the finite element (FE) simulation was chosen to match the actual geometrical and material properties of the tested specimens. Using properties given in Section 5.1 as an input, the finite element simulation is able to create virtual experiments with the curved crack front using plate elements and quadratic interface elements INT8 with exponential TSL. A comprehensive analysis of the crack front shape will be presented in the following chapter. A regular finite element mesh was created using element size 2.5 x 2.5 mm, which is appropriate since this size matches the general recommendation from the literature [55] and since the experimental measurements use DIC facets of roughly the same size. By conducting the same measuring principles (see section 3.5) for virtually created experimental output, the Area method data-reduction scheme should be able to identify the fracture toughness that corresponds to the original input of the FE model. Therefore, the expected result of this procedure is a flat R-curve since the virtual experiments do not suffer from experimental noise and scatter.

Results of the performed virtual experiments for different specimens of different dimension are shown in Figures 4.8, 4.9 and 4.10 with input value for fracture toughness computed in section 3.5.2. The adopted area method data-reduction scheme yields predictions of the fracture toughness that are ultimately within 1 % with respect to the FE model input. This confirms that the proposed procedure is valid for specimens of different geometries and, and in contrast

to other data-reduction methods, is able to account for crack front curvature. It can be noticed that the procedure is not very accurate for short cracks, but approaches the exact solution as the crack propagates further. In fact, the value of the fracture resistance obtained at the end of the simulation represents the average for all crack lengths, which follows from the definition of the method explained in Section 3.5.2.

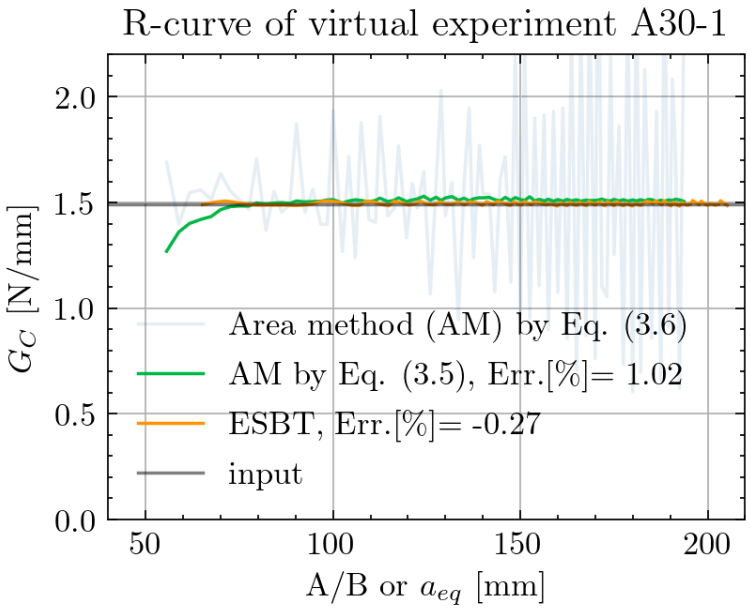

Figure 4.8: R-curves from A30-1 virtual experiment, note that the errors (Err.) are calculated for last considered point in the R-curve

The standard area method formula (3.6) shows large scatter around the FE model input, so it is presented by a slightly transparent line in Figures 4.8, 4.9 and 4.10. On the other hand, using the ESBT data-reduction scheme, based on the beam theory, leads to accurate prediction of the fracture toughness. This result indicates that data-reduction schemes based on the equivalent crack length could be used also on specimens with lower length-to-width ratio to produce accurate predictions of the fracture resistance. The fact that in such specimens the crack front is curved does not significantly influence the accuracy of the method, since it is based exclusively on the measurement of the applied load and the load-line displacement, which is done the same way independently from the specimens' dimensions. It is expected that the CBT method from [8] would also show a similar behaviour since it accounts for a crack-length correction based on the measured compliance. Although the crack length measured at the edge of the specimen might be not representative for specimens with a curved crack front, after correcting it, the CBT method will yield accurate predictions of the fracture resistance. The main advantage of the ESBT data-reduction scheme with respect to CBT is that it completely bypasses the measurement and

correction of the crack length, which could significantly simplify the experimental setup since the optical measuring tools for the crack length are not required.

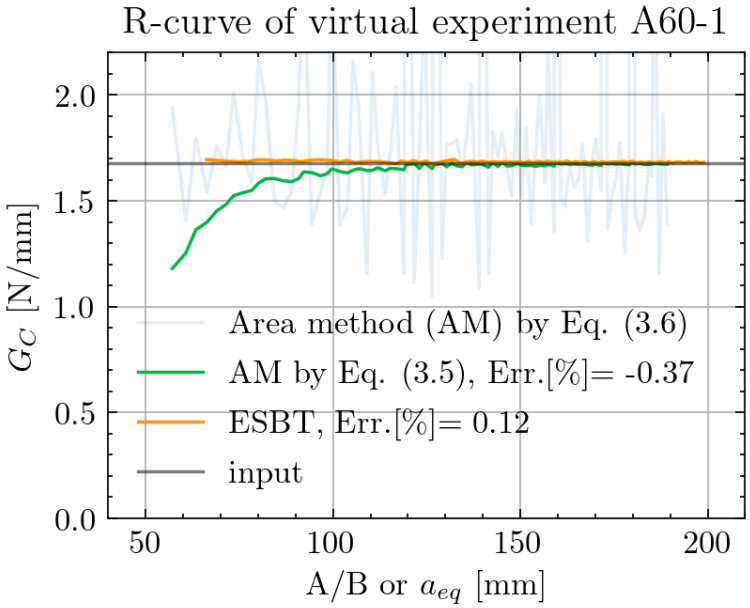

Figure 4.9: R-curves for A60-1 virtual experiment, note that the errors (Err.) are calculated for last considered point in the R-curve

The variation in specimen width does not indicate any change in the computed fracture toughness due to anticlastic bending of the substrates. An additional numerical study of the virtual experiments with variable widths is presented in Appendix E to confirm this conclusion.

Synthetic data from the virtual experiments can be further utilised to analyse the cohesive zone length. The cohesive length δ_0 of the TSL was adopted from the experiments on narrow specimens (A30) with different load application arrangement (see section 3.4). This value is then slightly modified by Equation (4.35), yielding 0.0050-0.0075 mm characteristic length depending on the thickness of adhesive layer. It is possible that the characteristic length has changed between two sets of experiments from sections 3.2 and 3.5. Note that experiments from Section 3.5 are used in the analyses in this and the following chapter. Given that the direct identification relies on the edge measurements of cross-sectional rotation at the load line and on the crack tip separation, the direct identification approach is not well suited for specimens with low length-to-width ratio (i.e. plate-like specimens). However, assuming that the cohesive zone length is dependent on material parameters in a following manner [102],

$$l_{cz} = \left(E'_A \frac{G_C}{\sigma^2_{MAX}} \right)^{1/4} h^{3/4} \tag{4.41}$$

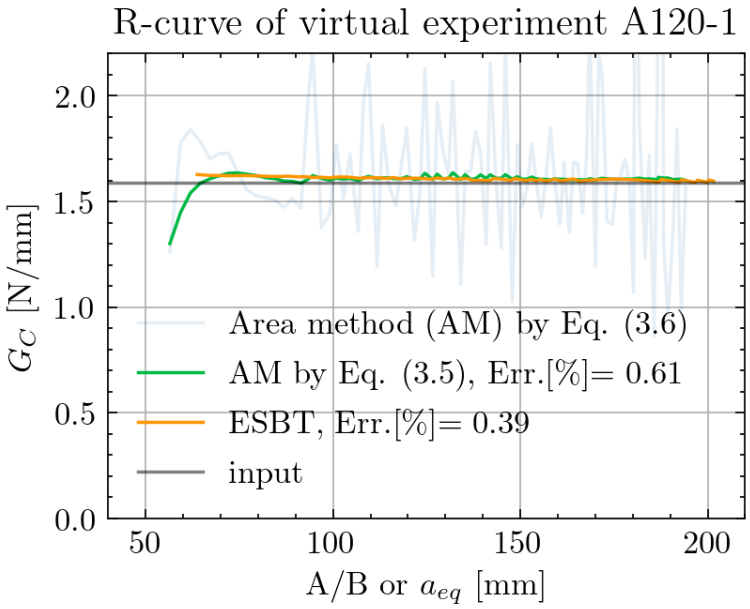

Figure 4.10: R-curves for A120-1 virtual experiment, note that the errors (Err.) are calculated for last considered point in the R-curve

one may conclude that any error in fracture parameters of the interface will result in an inconsistent cohesive zone length of real and virtual experiments. Inserting the required parameters in the above expression gives a cohesive zone length approximation of 8 mm, slightly higher than the experimentally measured 7 mm. Cohesive zone length measured from the virtual experiments, depicted in Figure 4.11, is about 6 mm which is slightly smaller than the length from the real experiments. The mentioned differences in this parameter are either a slight overestimate or underestimate of the real cohesive zone length, suggesting that the simply identified second TSL parameter (see section 4.2.4) is not too far from the actual value.

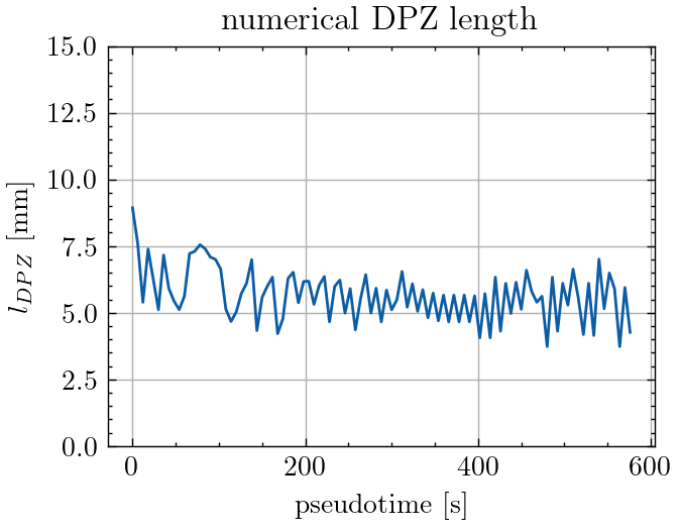

Figure 4.11: DPZ for A60-01 virtual experiment (pseudotime 60 s match 1 mm of displacement)

4.4.1 R-curves by ESBT Method

As demonstrated earlier, the R-curves obtained by ESBT data-reduction scheme can provide accurate predictions of the fracture toughness regardless of the specimen geometry. Area method data-reduction scheme with SBTSA method, can accurately predict only the average fracture resistance during crack propagation, but cannot provide a standard (non-cumulative) R-curve. Therefore, the ESBT method will be used to obtain the R-curves for all tested specimens (described in section 3.5), which is depicted in Figure 4.12.

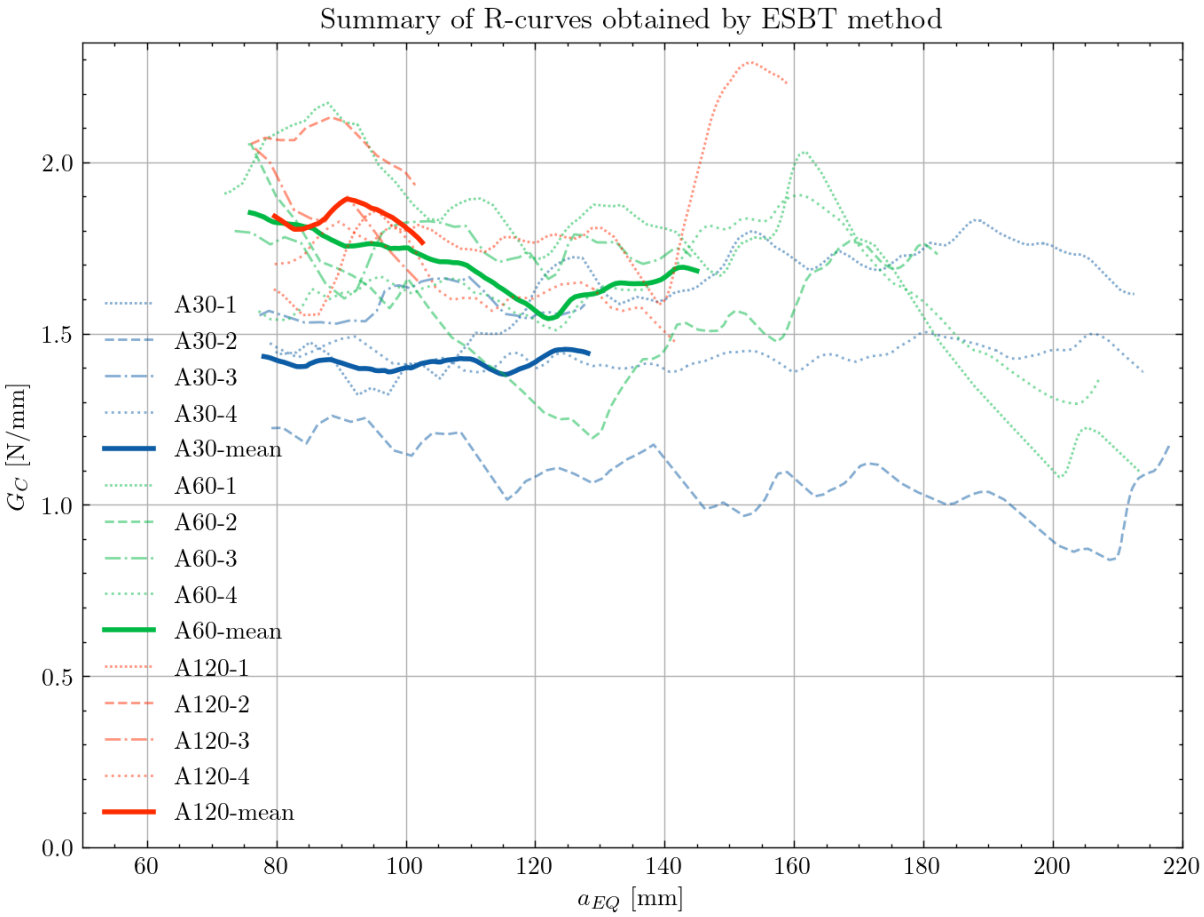

Figure 4.12: R-curves summary by ESBT method

Although this graphical representation might seem unclear, it can be noticed that within the range of the fracture resistance between 1.5 and 2.0 N/mm results, two of tested widths of the specimen, namely A60 and A120) almost entirely fit. If only R-curves up to a_{EQ}=100 mm are considered, no significant difference between A60 and A120 specimens can be noted, which is even more evident when considering the mean values of these curves over the relevant domain. In fact, even for some individual specimens of different widths such as A30-3, A60-3 and A120-1 there are parts of the R-curves where the differences in the fracture resistance are very small.

However, when the average fracture resistance is computed for each specimen and each width (see Table 4.4), the difference between different widths becomes more evident.

specimen	fracture toughness G_C^{ESBT} [N/mm]
A30-1	1.65
A30-2	1.07
A30-3	1.57
A30-4	1.44
A30-mean	(1.43)
A60-1	1.74
A60-2	1.59
A60-3	1.73
A60-4	1.62
A60-mean	(1.67)
A120-1	1.86
A120-2	2.04
A120-3	1.85
A120-4	1.66
A120-mean	(1.85)

Table 4.4: Fracture toughness obtained with ESBT data-reduction schemes

It seems that specimens A30 have a more stable crack propagation, but in average have lower fracture resistance compared to that of specimens A120, for which unstable crack propagation occurred in each test. In terms of the value of the mean fracture resistance and stability of the crack propagation, specimens A60 are indeed positioned between A30 and A120.

Chapter 5

Comparison of Experimental and Numerical Results

In the first section of this chapter, a comparison between the experimental and numerical load-displacement data is given. An additional comparison is made between the experimental and numerical results, this time with an objective of studying the crack front shape and size, as well as the DPZ size. This comparison reveals whether the selected numerical model is capable of reproducing the experimentally observed crack front shape. Obtained results validate both the experimental and numerical methods proposed in the present work. Finally, an analysis of the fracture toughness variation with varying width of the specimen indicate the geometrical dependency of this material parameter.

5.1 Comparison of Load-Displacement Curves

Following the discussion about the load-line displacement measurement presented in Section 3.5, the data from the TTM might be unreliable. The standard procedure [8] is to shift the force-displacement plot so that the linear part of the curve passes through the origin. It is questionable whether this criterion is appropriate for loading blocks that exhibit significant nonlinearity even before crack propagation since the stiffening effect [88] prevents rotation for small load-line opening. Furthermore, due to the anticlastic bending of plate-like specimens, softening occurs in the structural force-displacement response prior to peak force since the middle section might be damaged while the edge part is still intact [100]. Therefore, an objectively linear-elastic part of the measured force-displacement curve is hard to define.

Edge measurements of real load-line displacement with DIC is attempted with limited success. During the assembly of wider specimens, loading block parts at the edges (denoted as E120 in Figure 3.13) were loosely screwed when necessary to allow free rotation around the axis. Consequently, the rigidity of loading blocks was occasionally compromised which means that the edge measurements of load-line displacement might not be representative in those cases. Because of the aforementioned unreliability in the second method, its correction was rounded to 0.1 mm, which ultimately led to a good agreement of the experimental and numerical load-displacement elastic response (before crack propagation).

Data used for comparison of experimental and numerical results is summarised in the Table 5.1. As a reminder, fracture toughness was computed for each specimen in section 3.5, while the characteristic length was identified on previous set of experiments in section 3.4 and then corrected using the method presented in Section 4.2.4 via Equation (4.37) to account for the adhesive thickness variation. Peak traction σ_{MAX} for exponential CZM depends on the previous two values, while the actual initial crack is measured after specimen failure and rounded to 2.5 mm to comply with the FEM mesh (see the last column in Table 5.1).

specimen	fracture tougness G_C [N/mm]	characteristic length δ_0 [mm]	peak traction σ_{MAX} [MPa]	initial crack a_0 [mm]
A30-1	1.55	0.0050	114	52.5
A30-2	1.09	0.0050	80	52.5
A30-3	1.43	0.0050	105	52.5
A30-4	1.39	0.0050	102	52.5
A30-mean	(1.37)	(0.0050)	(100)	(52.5)
A60-1	1.70	0.0065	96	52.5
A60-2	1.52	0.0065	86	52.5
A60-3	1.77	0.0065	100	52.5
A60-4	1.55	0.0065	87	52.5
A60-mean	(1.63)	(0.0065)	(92)	(52.5)
A120-1	1.63	0.0075	80	50.0
A120-2	2.06	0.0075	101	50.0
A120-3	1.71	0.0075	84	52.5
A120-4	1.67	0.0075	82	52.5
A120-mean	(1.77)	(0.0075)	(87)	(51.25)

Table 5.1: Material properties of the interface

For specimens A30, an excellent agreement between the experimental and numerical force-displacement curves is obtained, which is shown in Figure 5.1. In general, small differences may be attributed to experimental uncertainty or material property deviations across the crack length. However, numerical simulation of specimen A30-3 underestimates the experimental load-

displacement response in Figure 5.1.c).

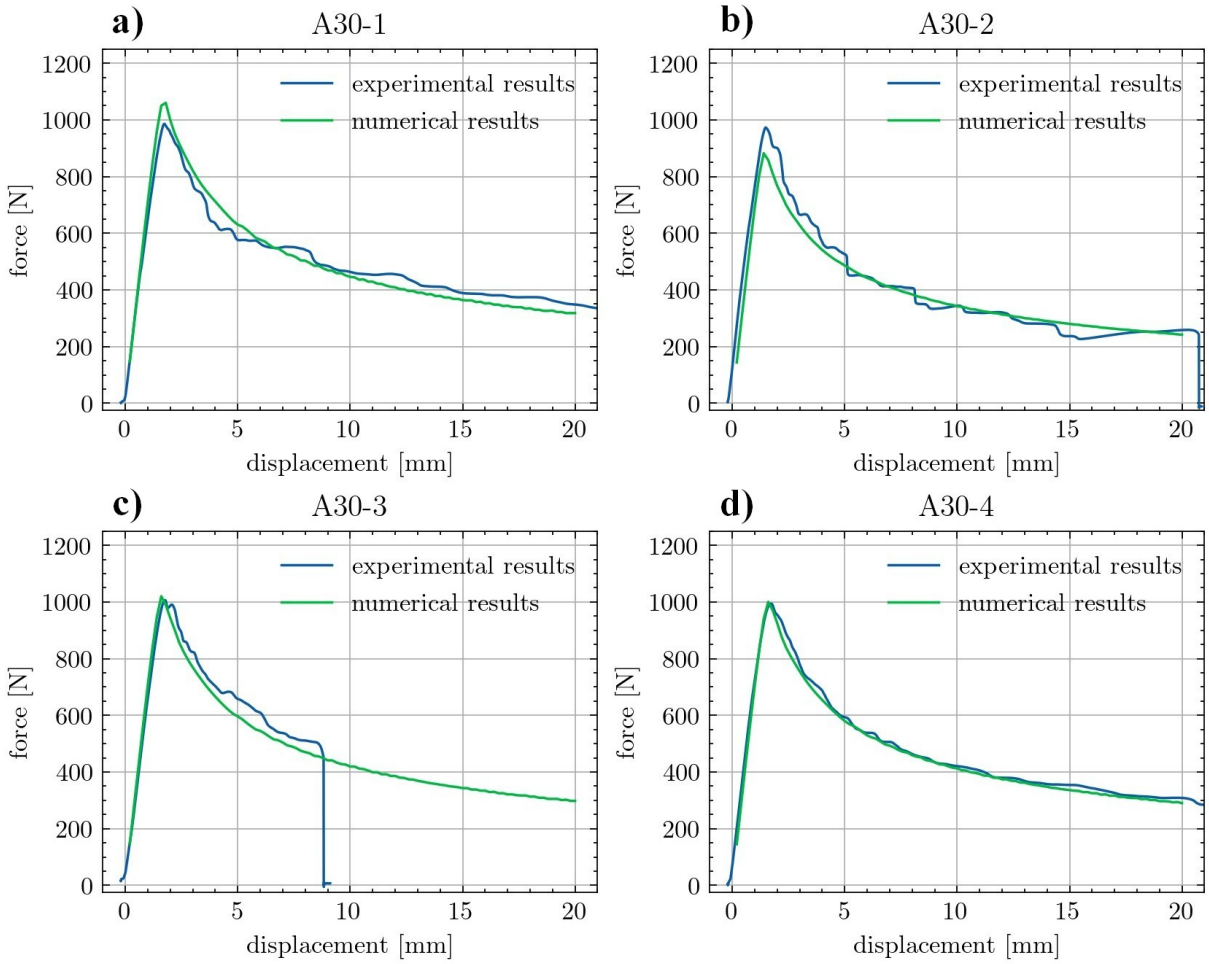

Figure 5.1: Comparison of experimental and numerical load-displacement response for specimens A30

Next set of results is for specimens A60, presented in Figure 5.2, where more experimental scatter is present, making the comparison between the model and the experiment more difficult. The most pronounced discrepancy is visible for specimen A60-3 near the peak force in Figure 5.2.c). This may be attributed to a material defect near the initial crack tip.

Finally, a comparison of the curves for widest specimens A120 is depicted in Figure 5.3, where some experimental scatter can be again observed. This time the issue seems to be with specimen A120-01 where experimental and numerical curve disagree near the specimen failure, with numerical estimation slightly underestimating the structural response. This may be due to method of data-reduction, namely the area method which does not properly account for tougher experimental response near the end of crack propagation. This is due to the area calculation depicted in Figure 3.18, where increase in force will not enclose significant portion of area before the subsequent force decrease.

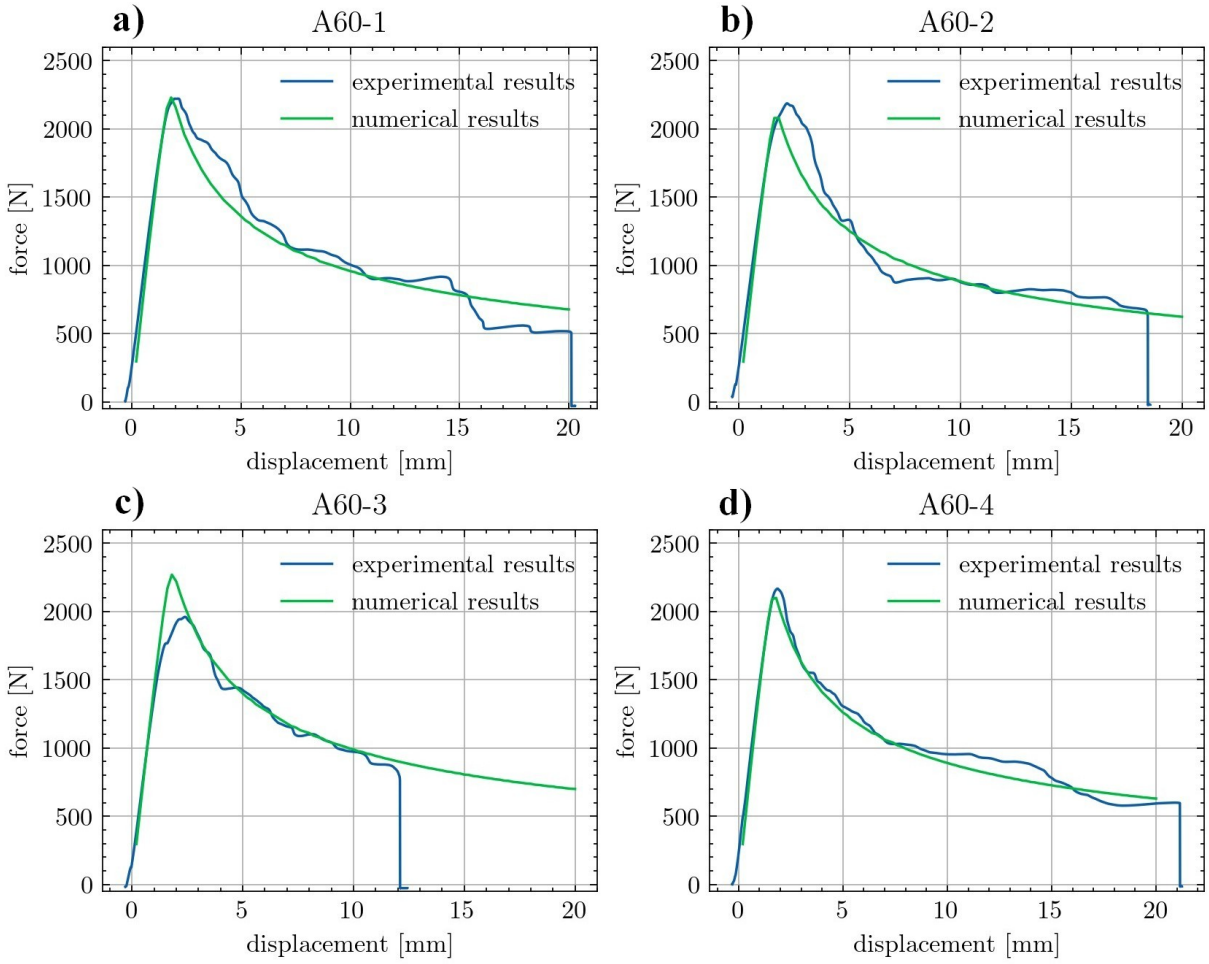

Figure 5.2: Comparison of experimental and numerical load-displacement response for specimens A60

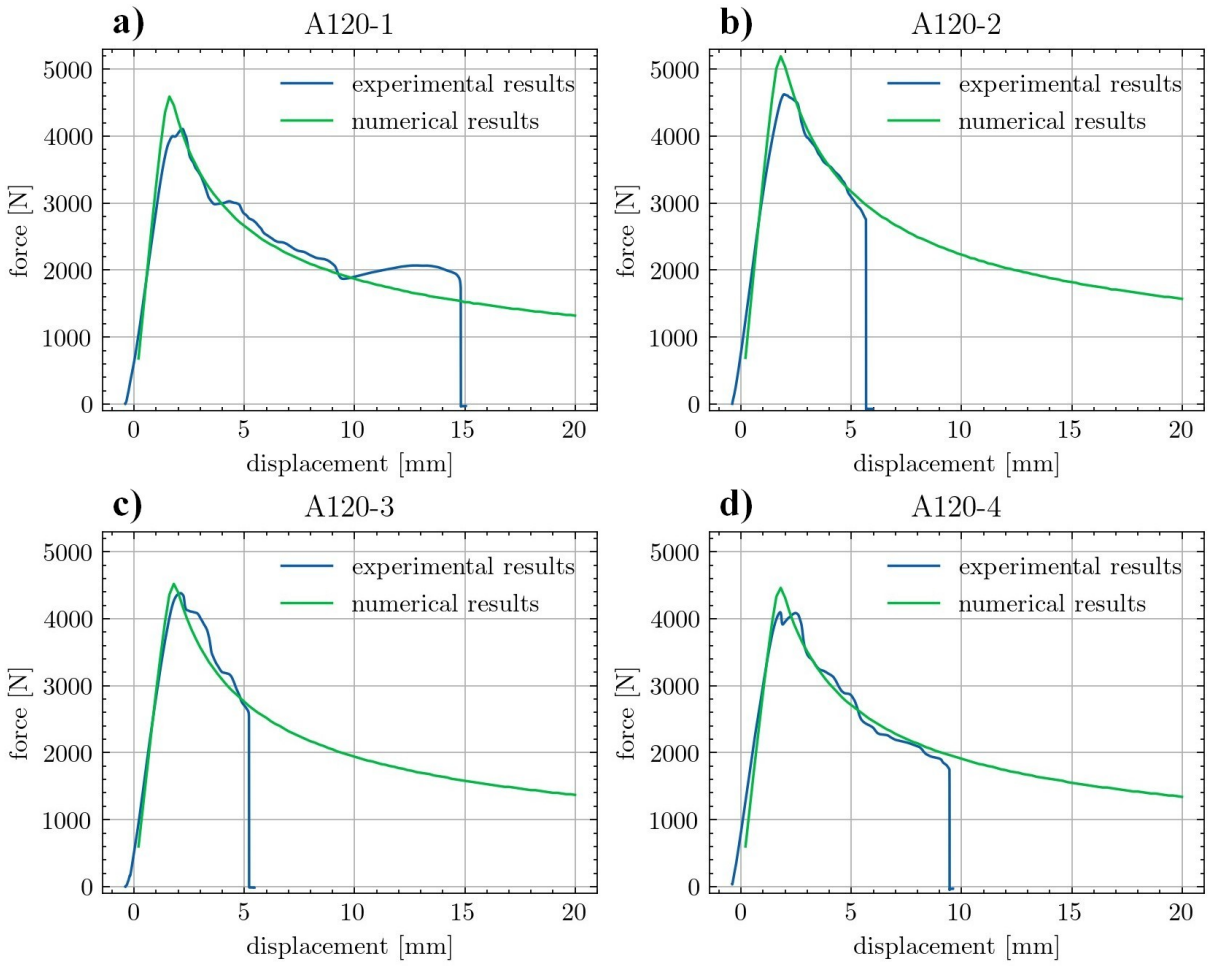

Figure 5.3: Comparison of experimental and numerical load-displacement response for specimens A120

Even though the agreement between the experimental and numerical load-displacement response is for the most part satisfactory, the area under the load-displacement curve obtained from the numerical simulation for specimen A30-3 is smaller than that under the experimental load-displacement curve. This implies a possibility of an inaccuracy in the computation of the fracture toughness for specimen A30-3 that in fact had a very long DPZ prior to abrupt failure (see Figure 3.22.f)). As an additional check, the present comparison is repeated in Appendix F with the fracture toughness for individual specimens computed using the ESBT data-reduction scheme. This issue is indeed fixed when using the ESBT method, however, differences between the results of this two methods are not significant (about 4 % on average). Therefore, further analysis will be made primarily using the data obtained by the Area method.

5.2 Crack Front Shape

At the beginning of the DCB test, the crack will tend to propagate in the middle of the width prior to propagating at the edges, which is known as the crack tunnelling. Before the onset of crack propagation, the plate edges will even compress one another due to anticlastic bending.As explained in Section 3.4, this behaviour presents a difficulty when measuring the initial crack opening separation at the edges [26]. In addition to the mentioned anticlastic effects, which are external constraint effects [58], there are also effects concerning the adhesive (internal constraint effects). Those are primarily geometrical influences such as thickness and width, which lead to different stress states in the adhesive layer. This is an additional explanation for crack tunneling since lower stiffness caused by lower triaxiality at the edges distribute more load to the middle (load shedding) [60]. However, a good estimate of crack front shape that is presented hereafter would suggests that accounting for spatially varying interface properties, due to stress triaxiality, is unnecessary for a good agreement of experimental and numerical data.

The experimental and numerical crack front shape analysis is presented in Figures 5.4, 5.5, 5.6 for specimen A60-1, and Figures 5.7, 5.8, 5.9 for specimen A120-1. At the left-hand side of each figure the enlarged region of interest (ROI) is shown, while on the right hand side of these figures load-displacement response and the location of the region of interest (ROI) on the specimen are shown. Particular specimens and prescribed displacement were picked with consistency in mind. The narrowest specimen was intentionally omitted due to a larger portion of edge areas relative to the total area of the interface since DIC measurements at the edges are typically lost, which becomes less important when the specimen is wide.

Experimental reading of threshold opening ($\delta_C^{A60}/2$=0.050 mm, $\delta_C^{A120}/2$=0.060 mm) defining the crack tip is shown with a red curve, while the white curve defined at ($\delta_0^{A60}/2$=0.003 mm, $\delta_0^{A120}/2$=0.004 mm) represents the experimental measurement of other edge of the DPZ. Numerical readings of the DPZ are depicted by the limiting colours of the contour plot, i.e. yellow border is the isoline corresponding to the opening ($\delta_C^{A60}/2$=0.050 mm, $\delta_C^{A120}/2$=0.060 mm) and the purple border is at ($\delta_0^{A60}/2$=0.003 mm, $\delta_0^{A120}/2$=0.004 mm) opening. For the presented numerical and experimental analysis, the agreement of crack front shape and magnitude is satisfactory. Differences between the experimental and numerical average crack length are around few millimeters, while its shape is especially well modelled.

When considering the force-displacement response in conjunction with crack front shape

analysis, it is clear how the underestimate of numerically predicted force coincides with the overestimate of crack length. This conclusion is in accordance with fundamental theory, since less force is required to achieve the same displacement at a longer span. However, when the numerical and experimental load-displacement response overlap, e.g. in Figure 5.7, the model might still not be able to accurately predict the crack front position. This can be attributed simply to experimental scatter of crack front readings, which is more evident when observing the crack propagation as an animated series of graphs presented on the left-hand side of Figures 5.4-5.9.

Although the presented numerical results tend to underestimate the crack length by a small margin, this is not always the case. Recall how the coordinate system origin definition, described in Section 3.5, was made by hand picking the auxiliary points on the screen. The mentioned check of top plate intersection of diagonals did in fact yield errors in position of up to 1 mm. It is likely that this error was transferred to the measured crack length and partly contributed to the observed error of few millimeters. Furthermore, data processing for the presented analysis can impact the reliability of the results so a brief explanation is necessary.

First of all, contour plots on the left hand side of Figures 5.4-5.9 use interpolation to present the numerical data as smooth contour lines. Numerical data is given on a grid with 2.5x2.5 mm raster, which corresponds to the size of both the numerical finite elements used in simulations and to the size of experimental facets. In case of experimental data, facets are not stationary throughout the experiment, so the grid data had to be interpolated twice. Cubic interpolation is an appropriate choice since the beam theory uses it to exactly describe DCB deflection. Obviously, the data without cubic interpolation is not as smooth and it would reveal less information about the crack front shape.

Interesting to notice is how the DPZ shape, e.g. in Figure 5.4, does not resemble the over-the-width (through-width) distribution of the plastic zone according to elementary EPFM (Figure 2.5), in which the size of the plastic zone is larger when closer to free edges than at the inside. Unfortunately, the experimental evidence about the size of the plastic zone at the very edges of the specimen is lost since a row of DIC facets is missing. This happens because for DIC correlation neighbouring facets on all sides are required. Furthermore, data for the next few rows across the width may be altered by the cubic interpolation, where once more the neighbouring data is required to perform the interpolation. Therefore, an additional check of DPZ shape at the edges was performed by analysing experimental data that was now interpolated linearly throughout the

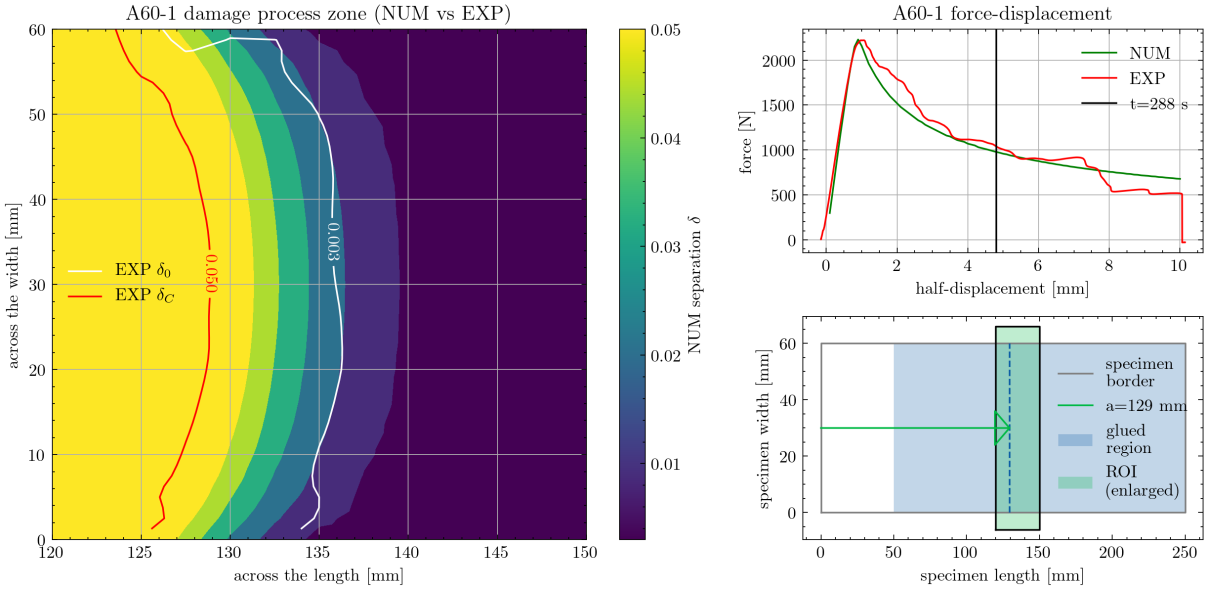

Figure 5.4: Crack front shape analysis for specimen A60-1 and 4.8 mm prescribed half-displacement (stage A)

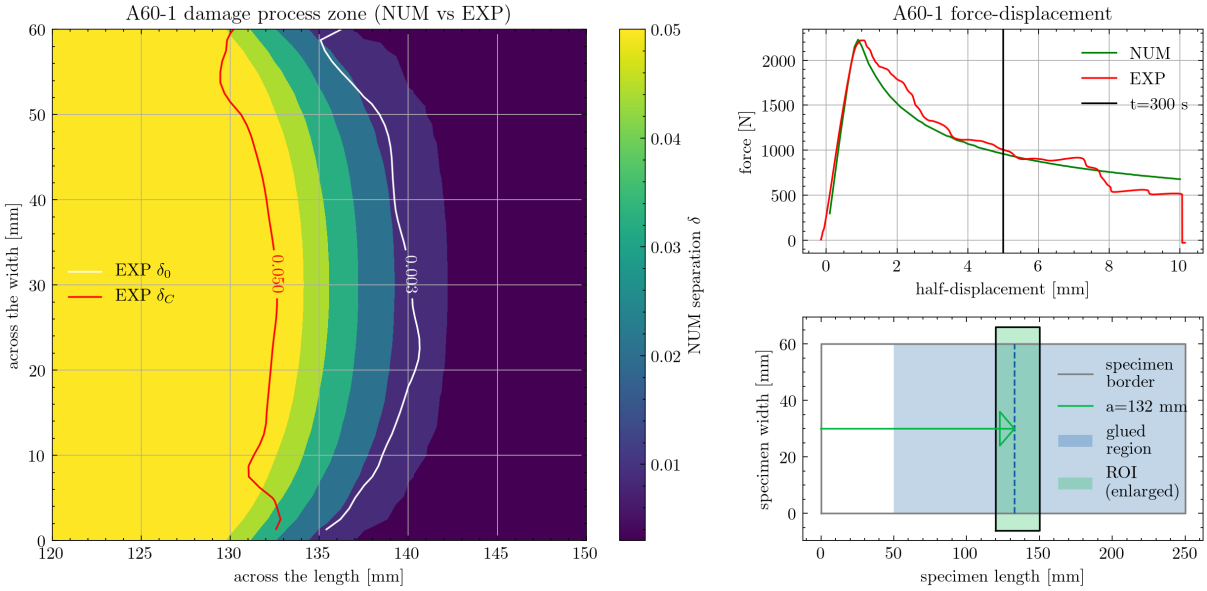

Figure 5.5: Crack front shape analysis for specimen A60-1 and 5.0 mm prescribed half-displacement (stage B)

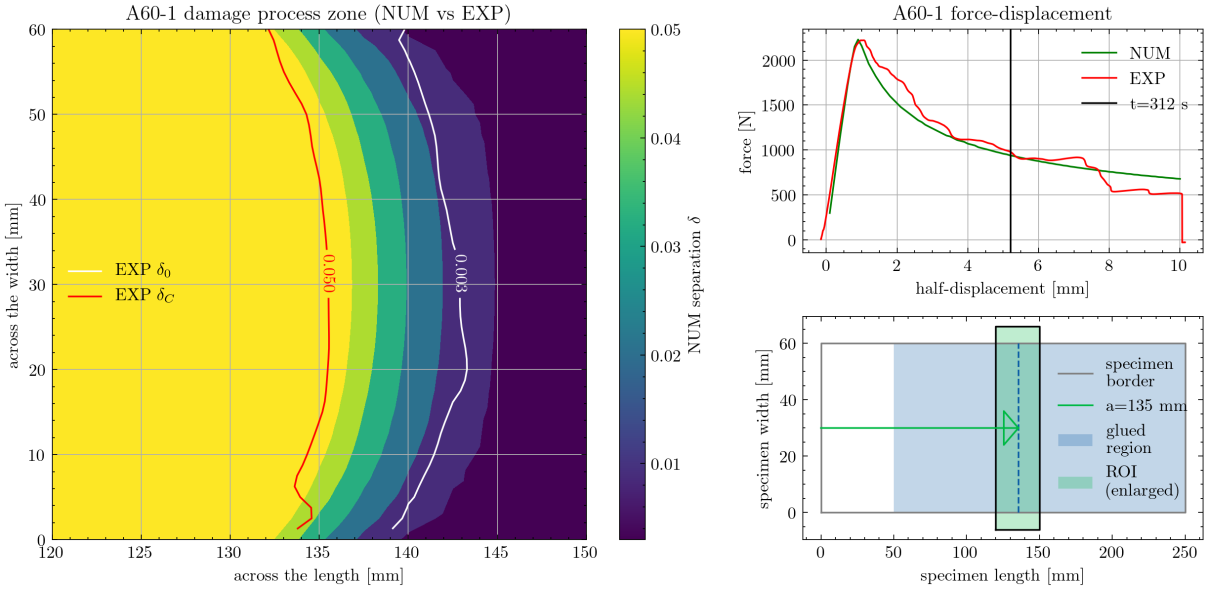

Figure 5.6: Crack front shape analysis for specimen A60-1 and 5.2 mm prescribed half-displacement (stage C)

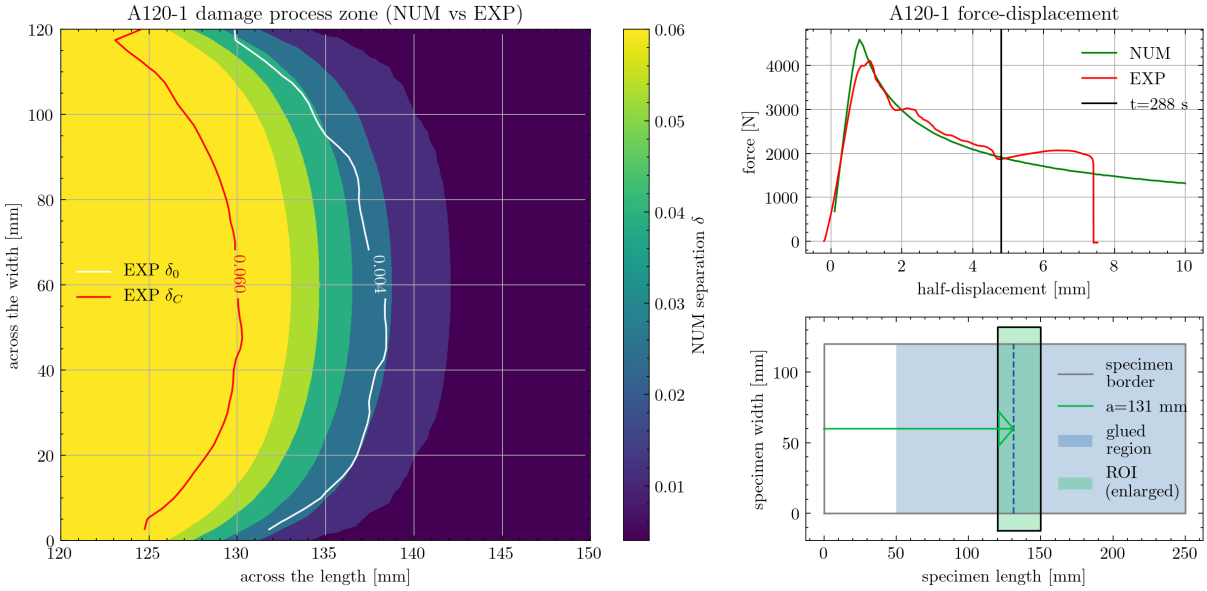

Figure 5.7: Crack front shape analysis for specimen A120-1 and 4.8 mm prescribed half-displacement (stage A)

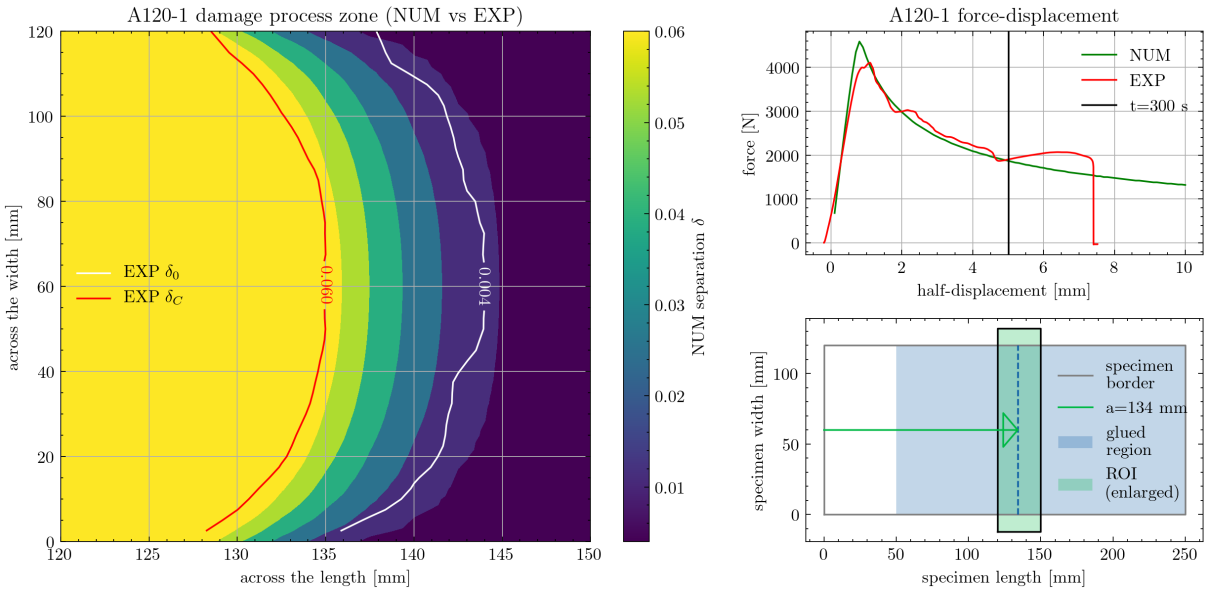

Figure 5.8: Crack front shape analysis for specimen A120-1 and 5.0 mm prescribed half-displacement (stage B)

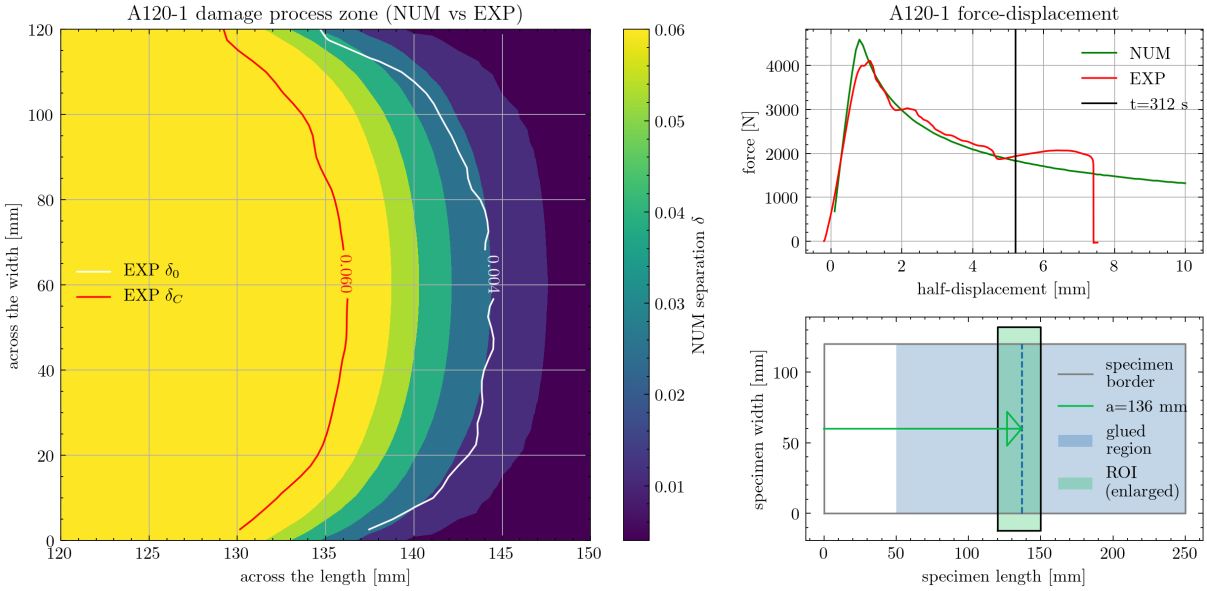

Figure 5.9: Crack front shape analysis for specimen A120-1 and 5.2 mm prescribed half-displacement (stage C)

rectangular grid. This attempt is shown in Figure 5.10 for the same experimental data already depicted in Figure 5.8, which does not reveal that FPZ is to any extent longer at the edges of the specimen. Note how experimental separation in Figure 5.10 is presented as full-field data instead of only contours of threshold opening as done earlier in Figures 5.4-5.9. Furthermore, even if the DIC facets at the edge were available, it is not straightforward how to differently define DPZ threshold δ_0 and δ_C depending on the stress state.

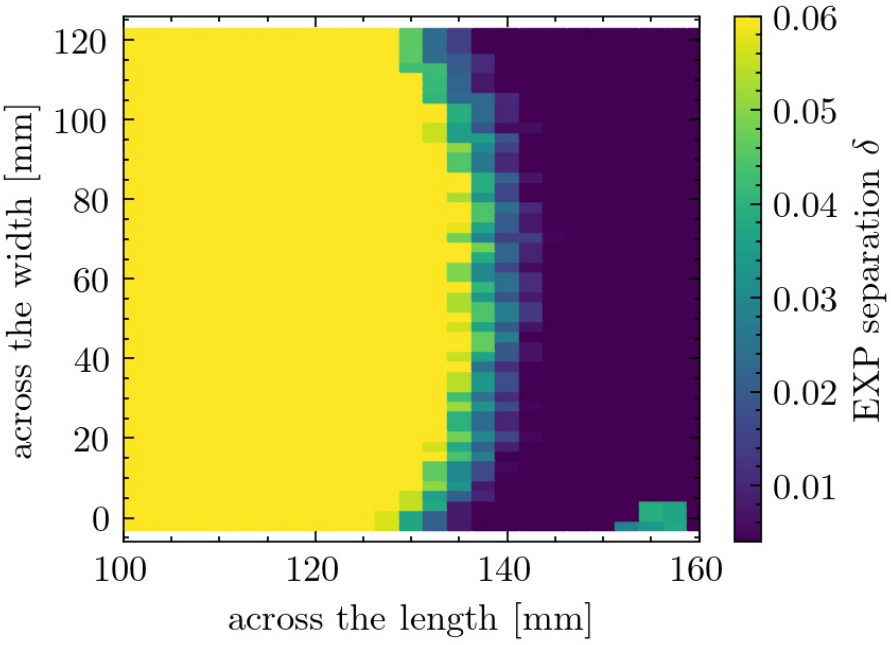

Figure 5.10: Crack front shape analysis with linear instead of cubic interpolation of experimentally measured separation

5.3 Discussion on Increase of Toughness with Width

The influence of the specimen width on the computed fracture toughness is depicted in Figure 5.11.a), which suggests the correlation of the increased adhesive layer's fracture toughness with the increase in specimen width. The average fracture toughness of the plate-like specimens (A120) is 29 % higher than that of the narrow specimens (A30) and only 8 % higher than that of the specimens A60. The widths considered in the current experimental programme are not extensive enough to draw much further conclusions. In a similar manner, the correlation between the fracture toughness and the adhesive thickness is noticeable in Figure 5.11.b), especially for the thickness ranging between 0.75 and 1.05 mm where specimens with considerably different widths, namely A60 and A120, give similar values of the fracture toughness. Given the correlation of specimens' width and thickness, it is hard to fully distinguish (uncouple) the influence of these two internal constraint effects. Finally, in the Figure 5.11.c), the correlation of the width-to-thickness ratio of the adhesive layer and the computed fracture resistance is given for reasons discussed below.

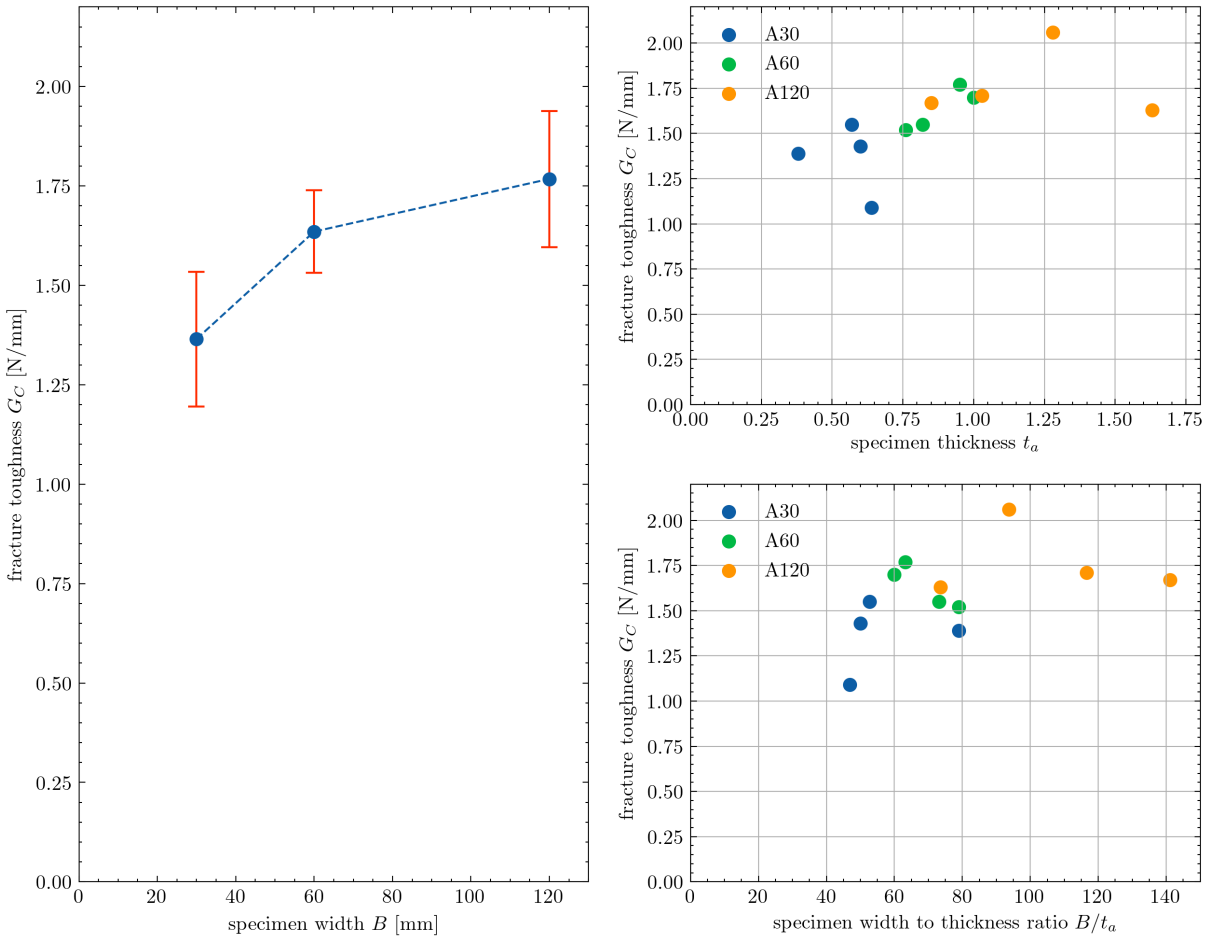

Figure 5.11: Fracture toughness vs a) specimen width or b) specimen width-to-thickness ratio

As already discussed in the introduction, Kinloch and Shaw [57] were among the first to recognise the fracture toughness dependence on the specimen width. One of their key finding is depicted in Figure 5.12. They described the bulk fracture toughness dependency on specimen width by employing stress triaxiality explanations. Higher degree of stress triaxiality and plane stress conditions, present near the sides of the specimen, are more dominant for narrow specimen. This in turn, leads to larger plastic zone [60] and higher values of the fracture toughness. However, an open question was left unaddressed about the opposite trend when same epoxy adhesive is used as a thin layer in a joint. Although the explanation that higher fracture toughness is due to a larger area of the plastic zone may seem reasonable, it is not obvious why would there be a larger area of the plastic zone for wider specimens. Part of the graph in Figure 5.12 referencing joint (thin layer) behaviour is actually a qualitative verification of the present results in Figure 5.11.a).

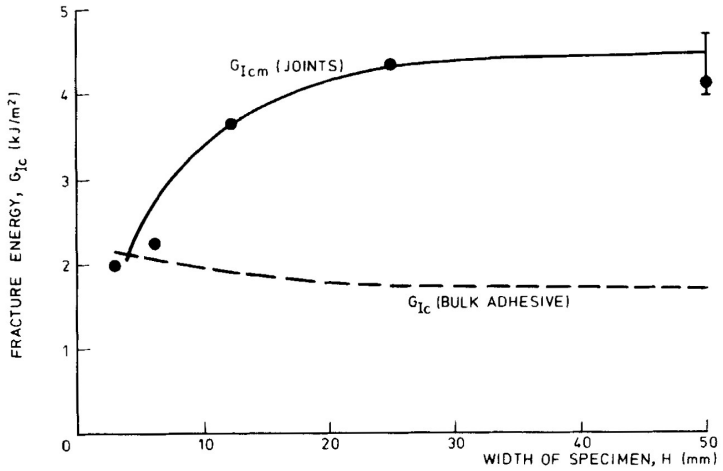

FIGURE 10 Fracture energy v. specimen width, H. (Temperature = 20°C; $\dot{y} = 1.67 \times 10^{-5}$ m/s.)

Figure 5.12: Fracture toughness vs specimen width, Figure is copied from Ref. [57]

Manterola et al. [71] explained width dependency of the adhesive thin layer with lateral contractions and stretch-shortening phenomenon that will decrease the effective area for narrow specimens. With their method, fracture toughness for specific B/t_A ratio can be used to compute the corresponding fracture resistance for any B/t_A ratio. However, this method was not able to replicate the dependency of the fracture resistance on the width of the specimen that was observed in the present work, which is possibly due to the fact that their model was verified only for flexible, but not for rigid adhesive. Even though the trend of increase in toughness with higher B/t_A may qualitatively explains the results shown in Figure 5.11.c), stretch-shortening

phenomenon is not a convincing argument for geometrical and material properties of the rigid adhesive tested in the present work. The computed fracture toughness for the narrow specimens (A30) was over 20 % lower than for the wide (A120) specimens. According to the method proposed in [71], this difference would be due to the reduction of the effective area of the narrow specimen by more than 20 % percent, or over 3 mm at each side, which obviously cannot be true for the rigid adhesive used in the experiments.

When analysing the different adhesive thicknesses for **identical specimen width** and the measured fracture toughness, either via Area method or ESBT data-reduction scheme presented in Table 5.2, no clear correlation is noticeable. For specimens A30, it appears that the specimen with the thickest adhesive (A30-2) gives fracture toughness that is considerably lower compared to those computed for other A30 specimens and especially to specimen A30-3 whose adhesive thickness is very similar. The results for specimens A120 indicate that there might be a maximum of the fracture toughness between adhesive thicknesses 1.29 and 1.63 mm, but there is not sufficient experimental data to support such a conclusion. According to [57], an optimal adhesive layer thickness corresponds to the plastic zone diameter, while thinner or thicker layers both result in a lower fracture toughness. Former was explained by the plastic zone suppression, while some authors explain the latter by higher chance of a defect for thicker adhesive or by a numerical analysis of maximum stress in an adhesive layer [94,111]. Additional experimental studies [58,112] confirm finding in [57] with optimal epoxy adhesive thickness, although some studies found no significant influence [93] of (epoxy) adhesive thickness on the measured fractured toughness, while in other studies [113] an almost linear increase of the fracture toughness with an increased (polyurethane) adhesive thickness was observed. Conflicting conclusions from the literature [57, 81, 93, 113] and small variations of the adhesive thickness for each separately considered width in present work does not facilitate the removal of adhesive thickness influence from the presented analysis.

It is worth mentioning that a considerable scatter in the individual R-curves (see Figure 4.12) occurs with no or very little variation of the adhesive thickness along the interface. It is still unclear why such big jumps/drops in the computed fracture toughness occur in the R-curve given that the failure of the adhesive is perfectly cohesive and no significant defects were noticed at the interface. Such oscillations in the R-curve are not necessarily symmetrical around the mean value and, therefore, can strongly influence the computed average values of the fracture resistance presented in Table 5.2 that were used in numerical simulations.

specimen	fracture toughness G_C^{AM} [N/mm]	fracture toughness G_C^{ESBT} [N/mm]	adhesive thickness t [mm]
A30-1	1.55	1.65	0.57
A30-2	1.09	1.07	0.64
A30-3	1.43	1.57	0.60
A30-4	1.39	1.44	0.38
A30-mean	(1.37)	(1.43)	(0.55)
A60-1	1.70	1.74	1.00
A60-2	1.52	1.59	0.76
A60-3	1.77	1.73	0.95
A60-4	1.55	1.62	0.82
A60-mean	(1.63)	(1.67)	(0.88)
A120-1	1.63	1.86	1.63
A120-2	2.06	2.04	1.29
A120-3	1.71	1.85	1.03
A120-4	1.67	1.66	0.85
A120-mean	(1.77)	(1.85)	(1.20)

Table 5.2: Fracture toughness obtained with Area method (AM) and ESBT data-reduction schemes

Chapter 6

Conclusions

Principal aim of this thesis was to test whether the adhesive material properties experimentally measured on standard beam-like DCB specimens can be used to adequately describe specimens of different geometries, namely plate-like specimens. To conduct this study:

- an extensive experimental programme was conducted and the results were comprehensively analysed,
- new methods for identifying material properties of the adhesive were developed and validated against the existing methods,
- and an effective numerical model was developed and validated against the experimental data.

Each of these points will be explained in more detail in the following paragraphs.

Experimental tests of DCB specimens of various widths were performed on a standard tensile-testing machine while the DIC technique was employed for measuring the following quantities: crack position and shape of the crack front, normal separation at the interface along the length, crosshead displacement, as well as the displacement and cross-sectional rotation at the load line. All the mentioned experimental data was collected from 21 DCB experiments in total, which is, not only extremely rare and unavailable, but in some aspects even unexisting to the best of author's knowledge. Prior to varying width of the DCB specimens, an extensive study of load arrangement influence was performed in order to eliminate it (in case it exists) from the experimental data that will be later acquired on specimens with varying width, but also to select the most appropriate loading arrangement for the plate-like specimens.

The acquired experimental data was used to compare the fracture toughness predictions in terms of R-curves obtained using different data-reduction schemes. It was demonstrated that the accuracy of both ESBT and CBT data-reduction schemes is comparable to that of the J integral. Thus, all three methods can be considered as accurate and reliable, although there are some differences when it comes to the practical application. The J integral approach requires the measurement of the cross-sectional rotation at the load line, while the CBT method requires the crack-length measurement. On the other hand, ESBT data-reduction scheme does not require any measurements other than force and displacement, but, unlike the CBT method, requires an accurate value of Young's modulus of the substrates. It was concluded that obtaining high-accuracy predictions of the fracture toughness in DCB tests can be hardly done without adding the DIC measurements. Although the analysed fracture surfaces on the broken specimens revealed that the failure of the adhesive was almost exclusively cohesive, the computed R-curves revealed some unpredictable bumps and oscillations. The source of such behaviour was not further examined, but this will be certainly done in the future. For now, it was just assumed that this might be possibly caused by crack path variations along the thickness of the adhesive layer and plastic zone suppression in contact with the substrates. Furthermore, a direct identification of the traction-separation law was performed for narrow specimens yielding high precision results of 1 micron resolution. This method, however, is not applicable to wide specimens and some adjustments had to be derived before using the extracted parameters for the plate-like specimens. Finally, the limitation of existing delamination test methods relying on the beam theory was overcome by developing the so-called Symmetry Based Top Surface Analysis (SBTSA) and implementing the Area Method to calculate the fracture toughness of wide specimens. This novel approach was later validated by means of virtual experiments performed using the novel numerical model. In addition, virtual experiments revealed that the ESBT data-reduction scheme can provide accurate predictions of the fracture toughness regardless of the specimen geometry (i.e. width).

As a final contribution of this thesis, a novel numerical model for simulating delamination/debonding in DCB test was developed and compared to similar models from the literature. The substrates were modelled using Q4U3 plate finite elements with cubic linked interpolation, while the adhesive was modelled using novel interface elements with an embedded exponential traction-separation law. Besides being significantly more computationally efficient compared to 3D solid FE models, it was demonstrated that the proposed FE formulation is capable of obtain-

ing converged solutions on meshes with elements of size comparable to that of the cohesive zone without using advanced numerical techniques. This is an important feature of the proposed FE model since the requirement of a sufficient number of rows of elements in the DPZ is a well-known limitation when it comes to numerical modeling of adhesive debonding.

Comparison of experimental and numerical data was made in terms of force-displacement response, as well as the crack and cohesive zone length and shape. The results show a very good agreement between the numerical and experimental data. External constraint effect regarding the anticlastic bending of plates is sufficient to properly model the crack front tunnelling. However, the performed virtual experiments did not suggest any increase in the identified fracture toughness with the width of the specimen. On the other hand, internal constraint effects such as stress state variation in the adhesive layer were not taken into account in the numerical model. This simplification did not lead to any significant inaccuracies in the crack front shape, suggesting that introducing such complexities in the numerical model is not required for the present analysis. Although this aspect is in accordance with the starting hypothesis, some fundamental questions were raised about the fracture toughness increase with the specimen's width. In particular, the computed fracture toughness for the narrow specimens (A30) is found to be almost 23 % lower compared to wider specimens (A60) and (A120), while the difference between specimens A60 and A120 is smaller. Although this phenomenon is known in literature, the provided explanations do not convincingly explain why this happened in the present study. Finally, the coincidental increase of specimen thickness that in the present work occurred in parallel with the increase of specimen width would require uncoupling of these two influences on the measured fracture resistance to draw stronger and more general conclusions. Future work includes the following:

- (a) detailed analysis of the broken specimen topography to correlate it with observed oscillations in the R-curve,
- (b) further development of the SBSTA method on irregular geometries for which the standard data-reduction schemes are not applicable,
- (c) test the FE model for different geometrical and material parameters, especially for different ductility and/or rigidity of the adhesive layer,
- (d) extend the FE model to debonding in modes II and III along with the higher-order facet shell elements for the substrates obtained by adding the membrane degrees of freedom and accounting for non-rectangular (curved in-plane) geometry when necessary, which can

ultimately be utilised to model mode mixity and to position facet shell elements along the curved crack front.

Appendices

Appendix A: Crack Reading Sensitivity of SBT and ECM Data-Reduction Methods

As discussed earlier in section 3.4, an automatic method for determining the crack tip position using the DIC, based on the value of the maximum separation of the interface δ_C, is used in this thesis.

Therefore, by adopting different values of δ_C, different crack lengths are obtained from the DIC measurements. The two unmentioned data-reduction schemes from the standard BS 25217:2009 [8], namely SBT and ECM, are sensitive to inaccuracies in the measurement of the crack length. This is shown in Figures 6.1 6.2, 6.3, where the R-curves calculated by SBT and ECM [22] method are clearly affected by different values of the maximum interface (critical) separation δ_C used in the DIC post-processing.

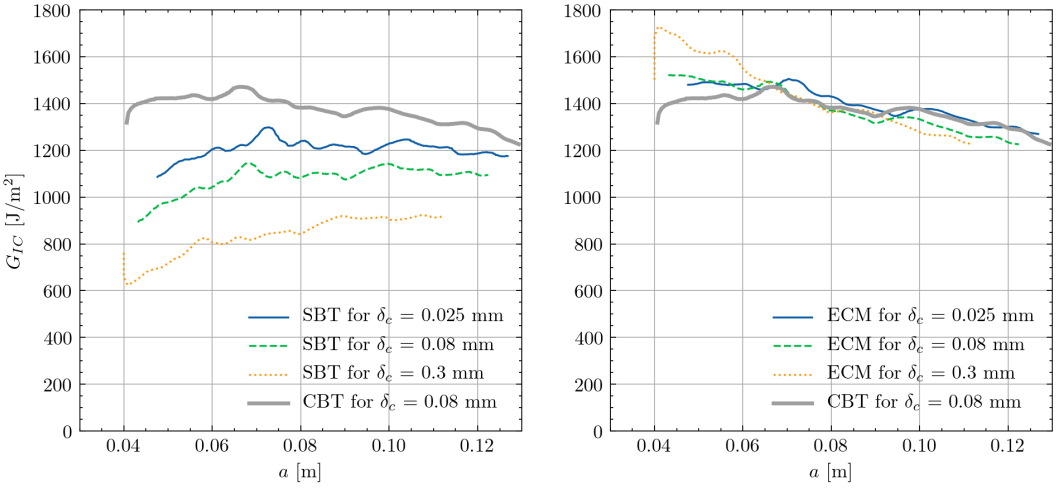

Figure 6.1: Sensitivity analysis of crack length defining critical separation (P1-P3)

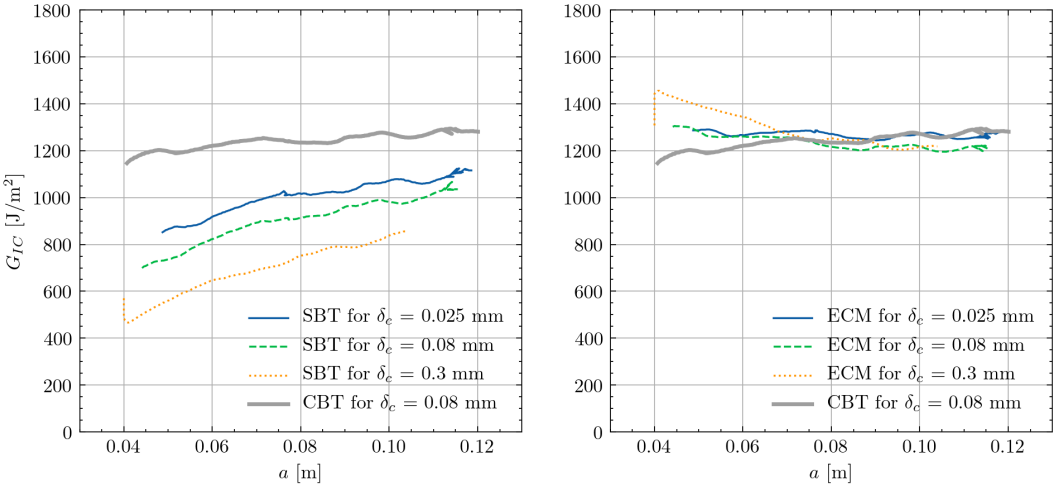

Figure 6.2: Sensitivity analysis of crack length defining critical separation (B1-B3)

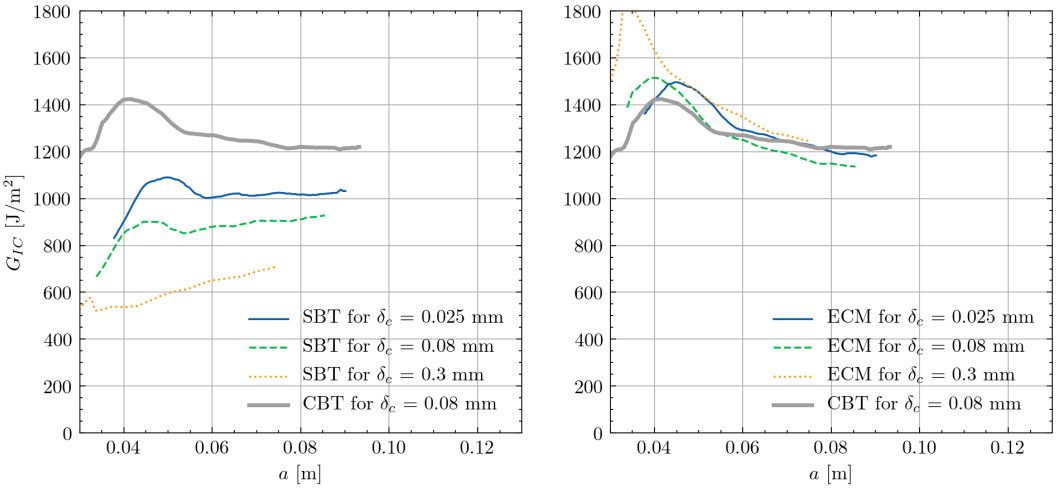

Figure 6.3: Sensitivity analysis of crack length defining critical separation (H1-H3)

Appendix B: Direct Identification of TSL using the Exponential Best Fit

Instead of Savitsky-Golay (SG) filter used in section 3.4, the non-linear least square method exponential fitting (EF) can be used, as depicted in Figures 6.4, 6.5, 6.6.

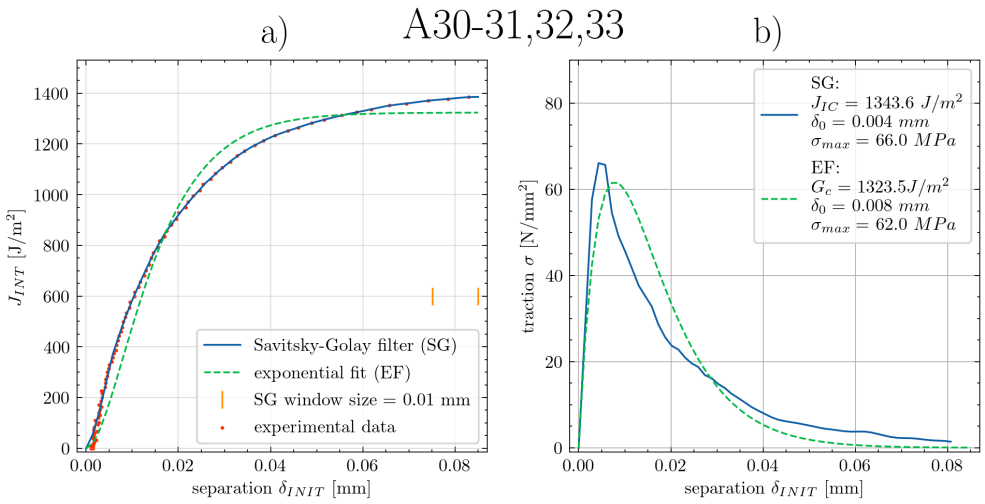

Figure 6.4: Direct identification of loading pins TSLs with Savitsky-Golay and exponential best fit approach, note that the average values of specimens P1-P3 are used

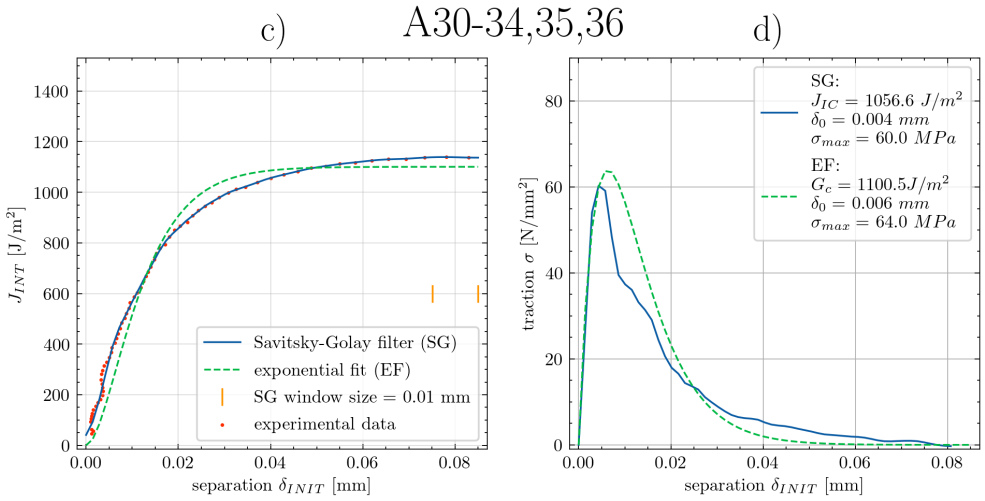

Figure 6.5: Direct identification of loading blocks TSLs with Savitsky-Golay and exponential best fit approach, note that the average values of specimens B1-B3 are used

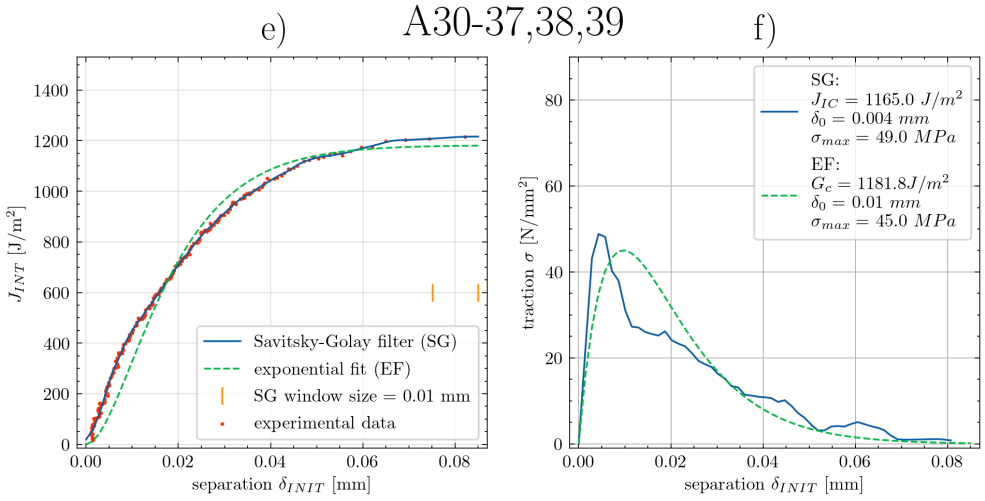

Figure 6.6: Direct identification of loading hinges TSLs with Savitsky-Golay and exponential best fit approach, note that the average values of specimens H1-H3 are used

Appendix C: Plate Theories

The plate theories [47] can be based on the same assumptions as the beam theories in a sense that the transverse shear deformation is either accounted for or neglected in assumed plate section kinematic and constitutive equations. If neglected, the governing theory is the Kirchhoff plate theory. The plate is assumed to be of a uniform thickness h with a mid-surface lying in the horizontal coordinate plane and a distributed load field acting on the plate mid-surface in the perpendicular direction. The displacement field is assumed to be linear across the cross-section

$$u(x, y, z) = -z\frac{dw_0}{dx} \tag{6.1}$$

$$v(x, y, z) = -z\frac{dw_0}{dy} \tag{6.2}$$

$$w(x, y, z) = w_0(x, y) \tag{6.3}$$

where (u, v, w) are the displacement components along the (x, y, z) coordinate directions, respectively, and w_0 is the transverse deflection of a point on the mid-surface (i.e. $z = 0$). Same as for the beam theory, the displacement field [114] implies that material fibres normal to the xy-plane before deformation remain straight and normal to the mid-surface after deformation. This assumption neglects both the transverse shear and in-plane effects and deformation is solely caused by the in-plane stretching or shrinking due to bending.

There are several shear deformation plate theories [115]. The simplest is the first-order shear deformation plate theory also known as the Mindlin plate theory, which is closely related to the Timoshenko beam theory and may be regarded as its generalisation to two-dimensional problems. The displacement field is expressed as

$$u(x, y, z) = z\theta_y(x, y) \tag{6.4}$$

$$v(x, y, z) = -z\theta_x(x, y) \tag{6.5}$$

$$w(x, y, z) = w_0(x, y) \tag{6.6}$$

where θ_x and θ_y denote cross-sectional rotations about x and y axes, as depicted in Figure 4.1. The difference between the normal and the actual rotations are the shear angles. The change of angles that the initially vertical fibres close with the mid-surface are the cross-section rotations around the global coordinate axes angles and are not necessarily perpendicular to the deformed

plate plane

$$\boldsymbol{\Gamma} = \begin{Bmatrix} \gamma_{xz} \\ \gamma_{yz} \end{Bmatrix} = \begin{Bmatrix} \theta_y + \frac{\partial w}{\partial x} \\ -\theta_x + \frac{\partial w}{\partial y} \end{Bmatrix} = \begin{bmatrix} 0 & 1 \\ -1 & 0 \end{bmatrix} \begin{Bmatrix} \theta_x \\ \theta_y \end{Bmatrix} + \begin{Bmatrix} \frac{\partial}{\partial x} \\ \frac{\partial}{\partial y} \end{Bmatrix} w = \boldsymbol{e\theta} + \nabla w \tag{6.7}$$

while the curvatures of the deformed plate plane, i.e. the fibers change of rotation are

$$\boldsymbol{\kappa} = \begin{Bmatrix} \kappa_x \\ \kappa_y \\ \kappa_{xy} \end{Bmatrix} = \begin{Bmatrix} \frac{\partial \theta_y}{\partial x} \\ -\frac{\partial \theta_x}{\partial y} \\ \frac{\partial \theta_y}{\partial y} - \frac{\partial \theta_x}{\partial x} \end{Bmatrix} = \begin{bmatrix} 0 & \frac{\partial}{\partial x} \\ -\frac{\partial}{\partial_y} & 0 \\ -\frac{\partial}{\partial x} & \frac{\partial}{\partial y} \end{bmatrix} \begin{Bmatrix} \theta_x \\ \theta_y \end{Bmatrix} = \boldsymbol{L\theta} \tag{6.8}$$

where $\boldsymbol{\theta}$ is the rotation vector with components θ_x and θ_y rotating around the respective in-plane axes x, y, w is the transverse displacement field, $\boldsymbol{\Gamma}$ is the shear strain vector and $\boldsymbol{\kappa}$ is the curvature vector. Gradient of the displacement field is denoted as ∇w while the differential operator on the rotation field is denoted as $\boldsymbol{L}$. A following linear elastic constitutive law is considered

$$\boldsymbol{M} = \begin{bmatrix} M_x \\ M_y \\ M_{xy} \end{bmatrix} = \frac{Eh^3}{12(1-\nu^2)} \begin{bmatrix} 1 & \nu & 0 \\ \nu & 1 & 0 \\ 0 & 0 & \frac{1-\nu}{2} \end{bmatrix} \begin{bmatrix} \frac{\partial \theta_y}{\partial x} \\ -\frac{\partial \theta_x}{\partial y} \\ \frac{\partial \theta_y}{\partial y} - \frac{\partial \theta_x}{\partial x} \end{bmatrix} = \boldsymbol{D_b \kappa} = \boldsymbol{D_b L \theta} \tag{6.9}$$

$$\boldsymbol{S} = \begin{Bmatrix} S_x \\ S_y \end{Bmatrix} = kGh \begin{bmatrix} 1 & 0 \\ 0 & 1 \end{bmatrix} \begin{Bmatrix} \gamma_{xz} \\ \gamma_{yz} \end{Bmatrix} = \boldsymbol{D_S \Gamma} = \boldsymbol{D_S(e\theta + \nabla w)} \tag{6.10}$$

where M_x, M_y, M_{xy} are the bending and twisting moments around the respective co-ordinate axes, while S_x and S_y are the shear stress resultants. Young and shear moduli are denoted as E and G, respectively, while ν and k are the Poisson's coefficient and the shear correction factor that is usually taken as 5/6 for rectangular sections and plates.

The Kirchhoff theory is basically a limiting case of the Mindlin theory when Γ approaches zero which is valid for very thin plates and is called a 'thin limit'. In case of Mindlin theory, the functional of the total potential energy reads

$$\Pi(w, \theta_x, \theta_y) = \frac{1}{2} \int (\boldsymbol{\kappa^T D_b \kappa}) dA + \frac{1}{2} \int (\boldsymbol{\Gamma^T D_S \Gamma}) dA + \Pi_{EXT} \tag{6.11}$$

By minimization procedures of this functional the equilibrium conditions can be achieved if sufficient boundary conditions are defined.

Appendix D: Simple Identification Verification

An additional validity check of proposed method of identification (see section 4.2.4) is performed using data from the literature [108], which is depicted in Figure 6.7. The authors studied the effect of adhesive thickness on the parameters of the traction-separation law by testing adhesive LOCTITE Hysol 9460 with six different thicknesses ranging from 0.09 mm to 1.00 mm. They found that the increase in the thickness leads to a higher critical opening δ_C at the crack tip and an increase in the fracture energy. The former is the important part to consider since it suggests that the elastic properties of thin layer are valid regardless of layer thickness.

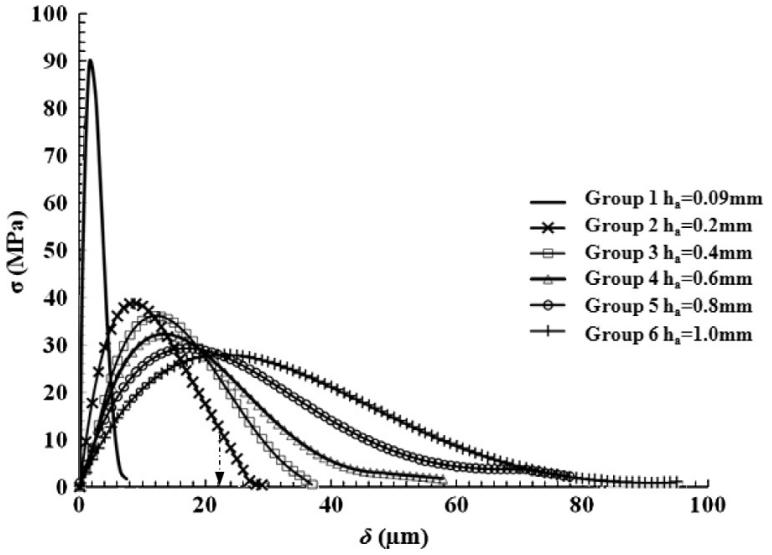

Figure 6.7: TSL Data from G. Ji et al (2010) [108]

In addition, the higher thickness was reported in [108] to decrease peak traction as is in fact expected from expression (4.36). As might be expected, smallest thickness had the highest recorded peak traction and they concluded this trend would continue for smaller thickness, although this is not in line with earlier research [58].

In any case, the fracture toughness they calculated from the DCB test along with Poisson's ratio and modulus of elasticity from the data sheet are the inputs used for the prediction of peak traction by Equation (4.36). Detailed comparison of prediction by Eq. (4.36) versus experimental data from [108] is given in Figure 6.8. The prediction of second parameter (σ_{MAX}) is excellent if the fracture toughness is calculated by a LEFM method from a DCB test, i.e. prediction underestimates the peak traction by 3 %, with discrepancies mostly at very thin layers 0.09 and 0.20 mm. On the other hand, if fracture toughness is calculated by a EPFM method, namely the J-integral, agreement is not as good since in this case, the prediction overestimates peak traction

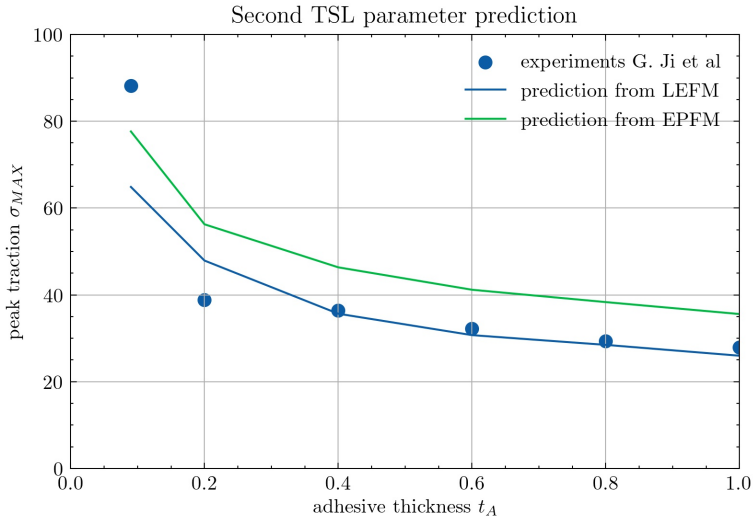

Figure 6.8: Additional validity test of simple identification by comparison with data presented in G. Ji et al (2010) [108] (abbreviations: LEFM- linear elastic fracture mechanics, EPFM- elasto-plastic fracture mechanics)

by about 24 %.

Appendix E: Virtual Experiments with Variable Plate Width

In order to test the influence of external constraint [58] of the variable substrate width, the virtual experiments were performed for variable widths using the constant interface material parameters δ_0 =0.0075 mm and G_C = 1.66 N/mm. It is evident from Figures 6.9, 6.10, 6.11 and 6.12 that influence of variable substrate width does not account for a significant change in the fracture toughness of the variable width specimens. Therefore, the anticlastic bending can not be an (only) explanation for the results presented in section 5.3.

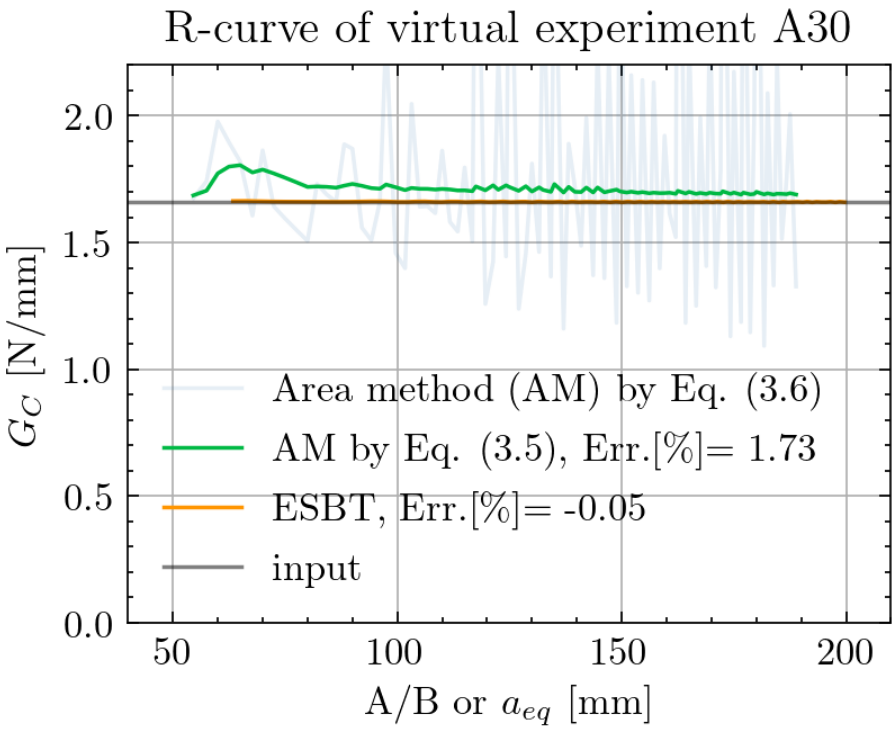

Figure 6.9: R-curve for A30 virtual experiment. Note that the errors (Err.) are calculated for last considered point in the R-curve

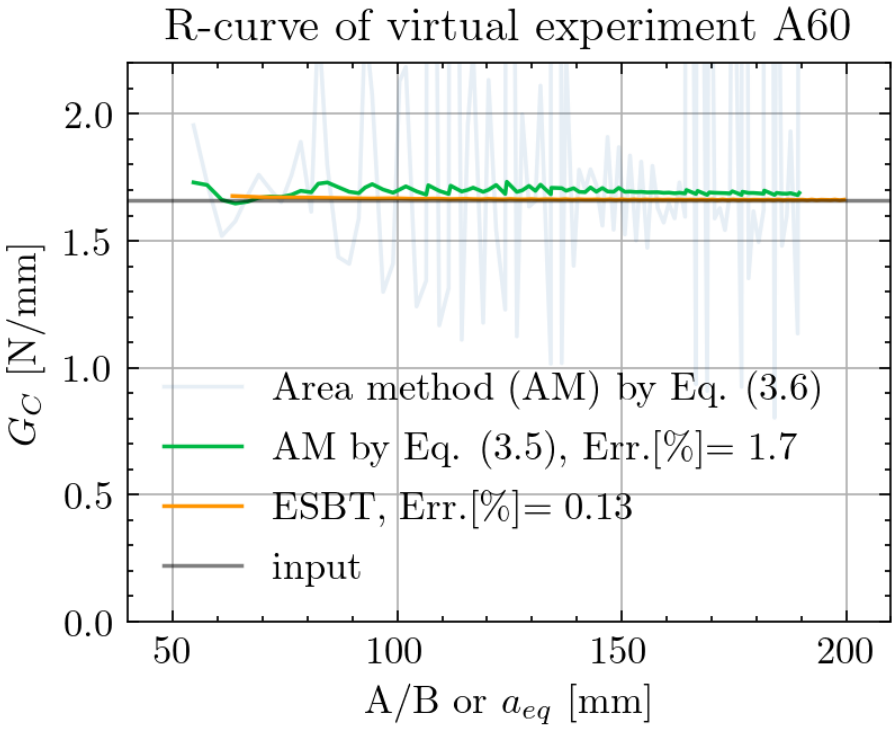

Figure 6.10: R-curve for A60 virtual experiment. Note that the errors (Err.) are calculated for last considered point in the R-curve

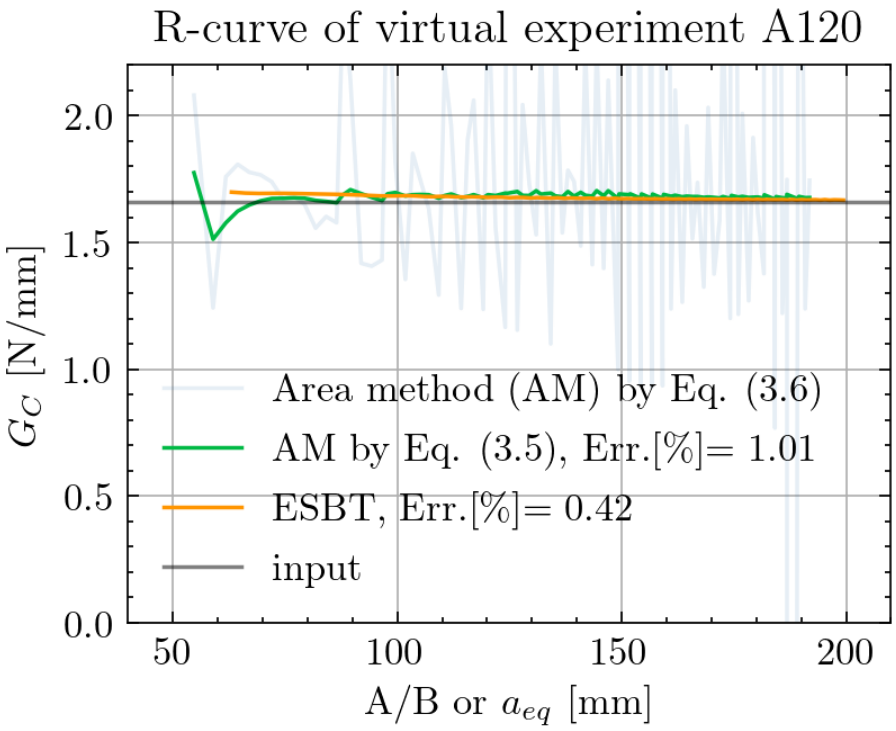

Figure 6.11: R-curve for A120 virtual experiment. Note that the errors (Err.) are calculated for last considered point in the R-curve

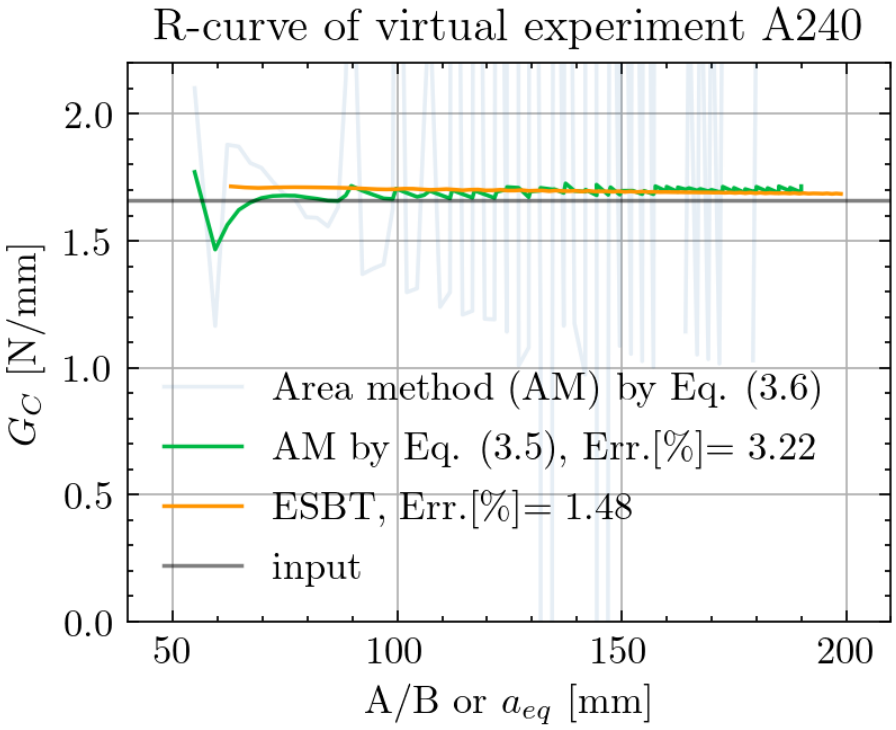

Figure 6.12: R-curve for A240 virtual experiment. Note that the errors (Err.) are calculated for last considered point in the R-curve

Appendix F: Comparison of Load-Displacement Curves with fracture toughness calculated also by ESBT

The analysis of load-displacement responses in Section 5.1 revealed slight inaccuracy in modelling of specimen A30-3. As an additional check, first the ESBT data-reduction scheme is used to compute the fracture toughness which is then used as an alternative numerical model input. This method was considered because virtual experiments presented in Section 4.4.1 showed that it can be used with a high accuracy even on plate-like specimens. Values computed by the ESBT method are presented in Table 5.2 side by side with the values computed by the Area method and the corresponding adhesive layer thickness. Comparison of experimental and numerical load-displacement response presented in Figures 6.13-6.15 displays two numerical curves made with data from Table 5.2.

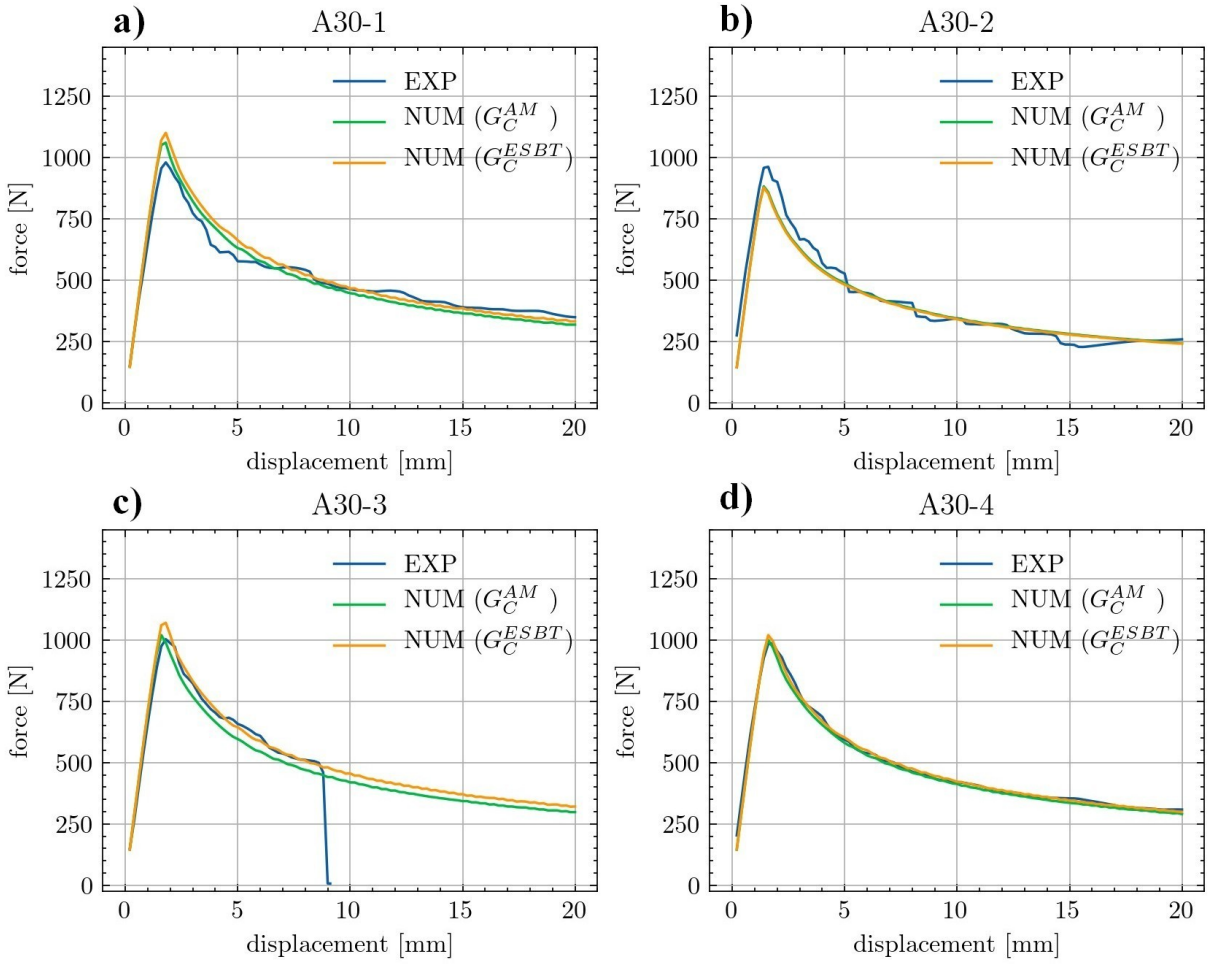

Figure 6.13: Comparison of experimental and numerical load-displacement response for specimens A30. Note that the fracture toughness is computed either by Area Method (AM) or ESBT data-reduction scheme (abbreviations: EXP-experimental results, NUM-numerical results, RSD-relative standard deviation)

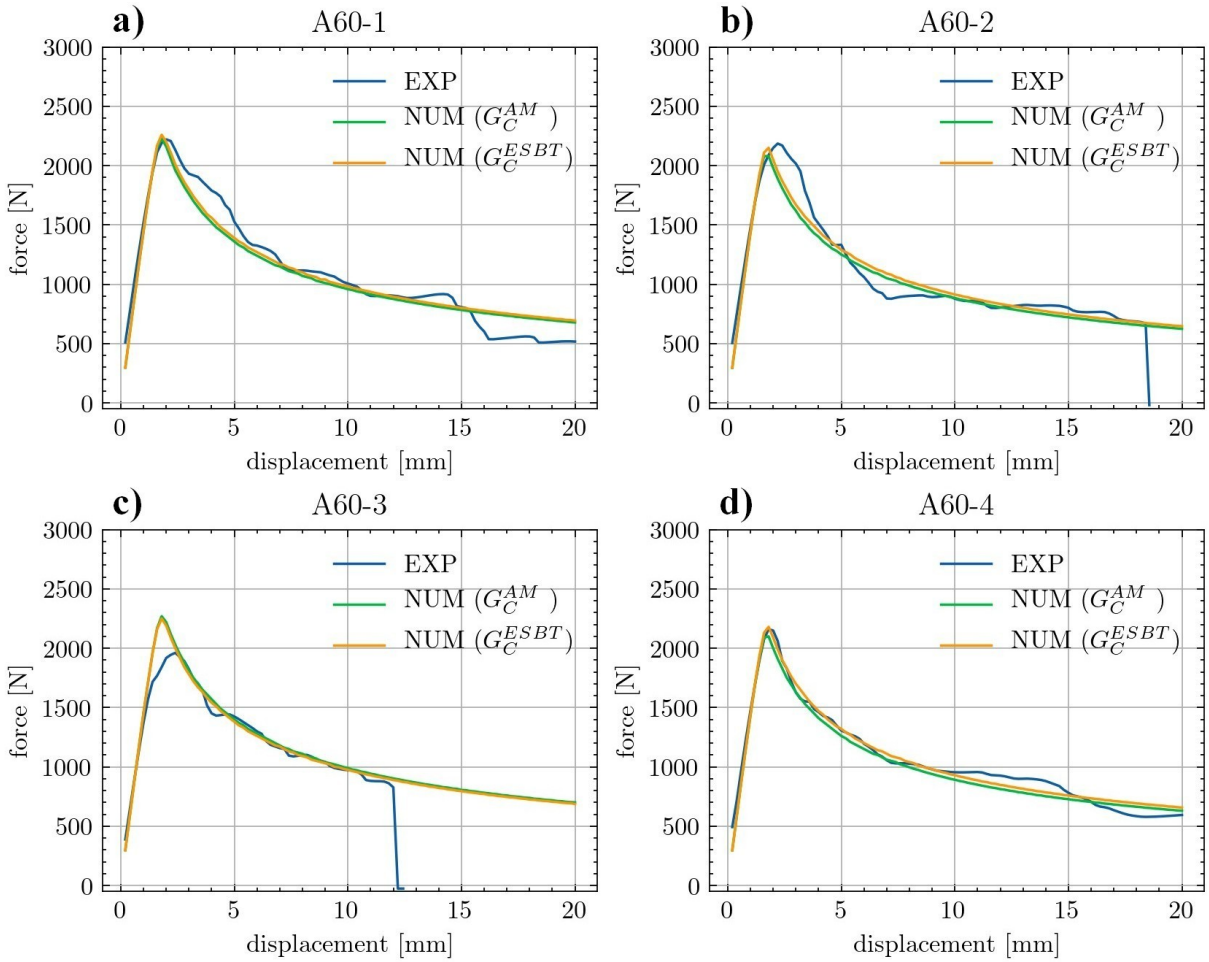

Figure 6.14: Comparison of experimental and numerical load-displacement response for specimens A60. Note that the fracture toughness is computed either by Area Method (AM) or ESBT data-reduction scheme (abbreviations: EXP-experimental results, NUM-numerical results, RSD-relative standard deviation)

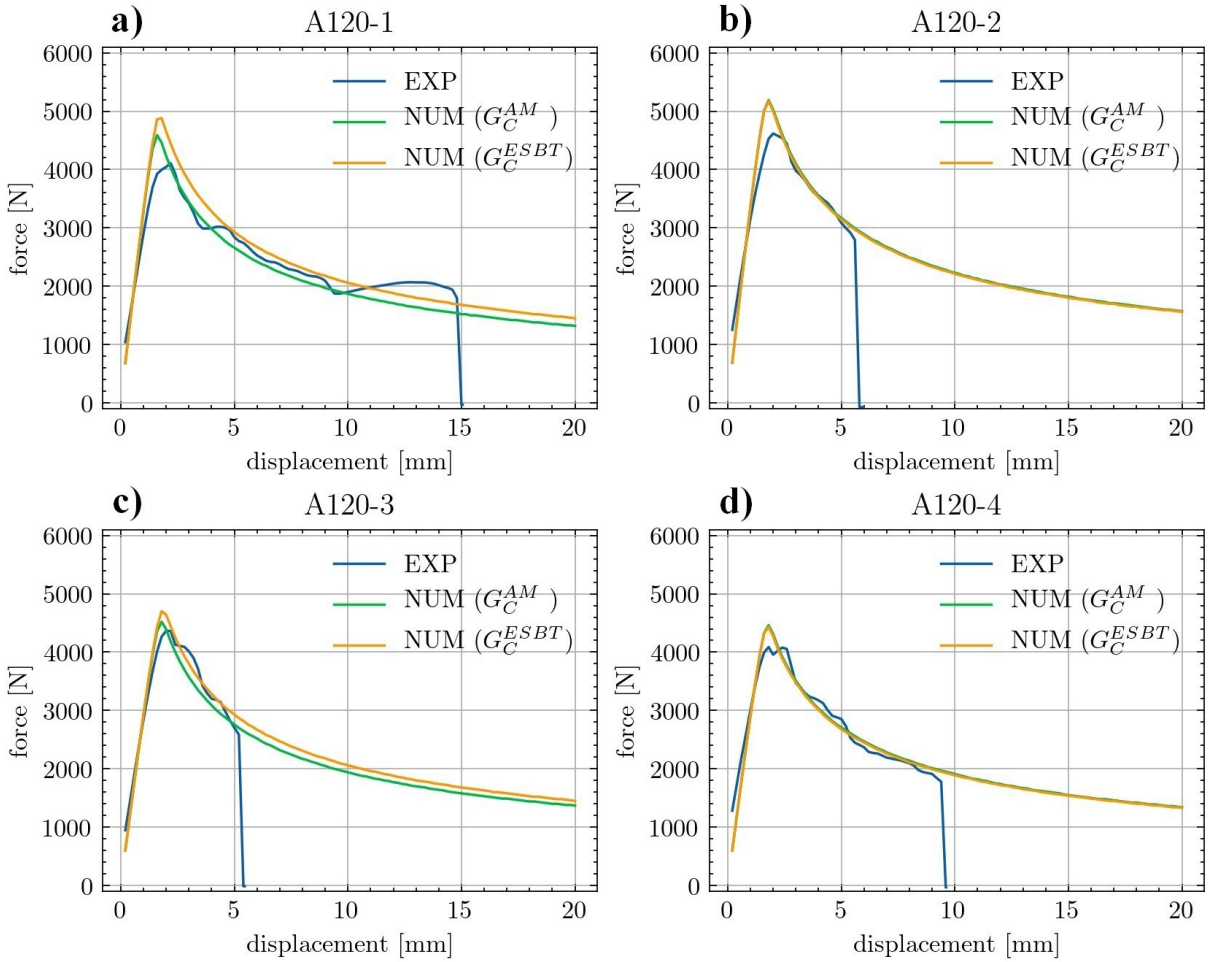

Figure 6.15: Comparison of experimental and numerical load-displacement response for specimens A120. Note that the fracture toughness is computed either by Area Method (AM) or ESBT data-reduction scheme (abbreviations: EXP-experimental results, NUM-numerical results, RSD-relative standard deviation)

Bibliography

[1] M. K. Budzik, M. Wolfahrt, P. Reis, M. Kozłowski, J. Sena-Cruz, L. Papadakis, M. Nasr Saleh, K. V. Machalicka, S. Teixeira De Freitas, and A. P. Vassilopoulos, "Testing mechanical performance of adhesively bonded composite joints in engineering applications: an overview," *The Journal of Adhesion*, vol. 98, pp. 2133–2209, Oct. 2022.

[2] P. Bidaud, *Analysis of the cyclic behavior of an adhesive in an assembly for offshore windmills applications.* PhD Thesis, Université Bretagne Occidentale, 2014.

[3] V. K. Khanna, "Adhesion–delamination phenomena at the surfaces and interfaces in microelectronics and MEMS structures and packaged devices," *Journal of Physics D: Applied Physics*, vol. 44, p. 034004, Jan. 2011.

[4] M. Goroll and R. Pufall, "Determination of adhesion and delamination prediction for semiconductor packages by using Grey Scale Correlation and Cohesive Zone Modelling," *Microelectronics Reliability*, vol. 52, pp. 2289–2293, Sept. 2012.

[5] Z. Liu and F. Yan, "Switchable Adhesion: On-Demand Bonding and Debonding," *Advanced Science*, vol. 9, no. 12, p. 2200264, 2022.

[6] M. D. Carnes and P. V. Mtenga, "The effect of materials and surface preparation on joining methods: A review," *Journal of Reinforced Plastics and Composites*, vol. 34, pp. 1167–1178, July 2015.

[7] T. Anderson, *Fracture Mechanics: Fundamentals and Applications.* CRC Press, 3 ed., Mar. 2017.

[8] B. ISO, "25217: 2009, Adhesives–Determination of the Mode I Adhesive Fracture Energy of Structural Adhesive Joints Using Double Cantilever Beam and Tapered Double Cantilever Beam Specimens," *British Standard*, 2009.

[9] A. Standard, "D3433-99: Standard Test Method for Fracture Strength in Cleavage of Adhesives in Bonded Metal Joints, ASTM International, West Conshohocken, PA," 2012.

[10] A. Standard, "D5528/D5528M-13, Standard Test Method for Mode I Interlaminar Fracture Toughness of Unidirectional Fiber-Reinforced Polymer Matrix Composites," 2013.

[11] L. Škec, G. Alfano, and G. Jelenić, "On Gc, Jc and the characterisation of the mode-I fracture resistance in delamination or adhesive debonding," *International Journal of Solids and Structures*, vol. 144-145, pp. 100–122, July 2018.

[12] F. Brandt, "New Load Introduction Concept for Improved and Simplified Delamination Beam Testing," *Experimental Techniques*, vol. 22, pp. 17–20, Jan. 1998.

[13] N. Blanco, E. Gamstedt, and J. Costa, "Mechanical hinge system for delamination tests in beam-type composite specimens," *Composites Science and Technology*, vol. 68, pp. 1837–1842, June 2008.

[14] W. H. Peters, W. F. Ranson, M. A. Sutton, T. C. Chu, and J. Anderson, "Application Of Digital Correlation Methods To Rigid Body Mechanics," *Optical Engineering*, vol. 22, Dec. 1983.

[15] J. Gorman and M. Thouless, "The use of digital-image correlation to investigate the cohesive zone in a double-cantilever beam, with comparisons to numerical and analytical models," *Journal of the Mechanics and Physics of Solids*, vol. 123, pp. 315–331, Feb. 2019.

[16] A. Mohan and S. Poobal, "Crack detection using image processing: A critical review and analysis," *Alexandria Engineering Journal*, vol. 57, pp. 787–798, June 2018.

[17] N. Gehri, J. Mata-Falcón, and W. Kaufmann, "Automated crack detection and measurement based on digital image correlation," *Construction and Building Materials*, vol. 256, p. 119383, Sept. 2020.

[18] A. Khudiakova, V. Grasser, C. Blumenthal, M. Wolfahrt, and G. Pinter, "Automated monitoring of the crack propagation in mode I testing of thermoplastic composites by means of digital image correlation," *Polymer Testing*, vol. 82, p. 106304, Feb. 2020.

[19] F. Sun and B. Blackman, "A DIC method to determine the Mode I energy release rate G, the J-integral and the traction-separation law simultaneously for adhesive joints," *Engineering Fracture Mechanics*, vol. 234, p. 107097, July 2020.

[20] L. Škec, G. Alfano, and G. Jelenić, "Enhanced simple beam theory for characterising mode-I fracture resistance via a double cantilever beam test," *Composites Part B: Engineering*, vol. 167, pp. 250–262, June 2019.

[21] I. Hlača, M. Grbac, and L. Škec, "Određivanje lomne žilavosti konstrukcijskih ljepila prilikom odljepljivanja u modu-I pomoću testa dvostruke konzole," *Zbornik radova (Građevinski fakultet Sveučilišta u Rijeci)*, vol. XXII, pp. 59–74, Dec. 2019.

[22] J. P. Berry, "Determination of Fracture Surface Energies by the Cleavage Technique," *Journal of Applied Physics*, vol. 34, pp. 62–68, Jan. 1963.

[23] E. J. Ripling, S. Mostovoy, and H. T. Corten, "Fracture Mechanics: A Tool for Evaluating Structural Adhesives," *The Journal of Adhesion*, vol. 3, pp. 107–123, Nov. 1971.

[24] S. Hashemi, A. Kinloch, and J. Williams, "The analysis of interlaminar fracture in uniaxial fibre-polymer composites," *Proceedings of the Royal Society of London. A. Mathematical and Physical Sciences*, vol. 427, pp. 173–199, Jan. 1990.

[25] J. Williams, "Large Displacement and End Block Effects in the 'DCB' Interlaminar Test in Modes I and II," *Journal of Composite Materials*, vol. 21, pp. 330–347, Apr. 1987.

[26] T. Andersson and U. Stigh, "The stress–elongation relation for an adhesive layer loaded in peel using equilibrium of energetic forces," *International Journal of Solids and Structures*, vol. 41, pp. 413–434, Jan. 2004.

[27] J. R. Rice, "A Path Independent Integral and the Approximate Analysis of Strain Concentration by Notches and Cracks," *Journal of Applied Mechanics*, vol. 35, pp. 379–386, June 1968.

[28] D. Dugdale, "Yielding of steel sheets containing slits," *Journal of the Mechanics and Physics of Solids*, vol. 8, pp. 100–104, May 1960.

[29] G. Barenblatt, "The Mathematical Theory of Equilibrium Cracks in Brittle Fracture," in *Advances in Applied Mechanics*, vol. 7, pp. 55–129, Elsevier, 1962.

[30] G. Alfano and M. A. Crisfield, "Finite element interface models for the delamination analysis of laminated composites: mechanical and computational issues," *International Journal for Numerical Methods in Engineering*, vol. 50, pp. 1701–1736, Mar. 2001.

[31] X. P. Xu and A. Needleman, "Continuum Modelling of Interfacial Decohesion," *Solid State Phenomena*, vol. 35-36, pp. 287–302, Sept. 1993.

[32] M. Van Den Bosch, P. Schreurs, and M. Geers, "An improved description of the exponential Xu and Needleman cohesive zone law for mixed-mode decohesion," *Engineering Fracture Mechanics*, vol. 73, pp. 1220–1234, June 2006.

[33] P. Olsson and U. Stigh, "On the determination of the constitutive properties of thin interphase layers—an exact inverse solution," *International Journal of Fracture*, vol. 41, pp. R71–R76, 1989. Publisher: Kluwer Academic Publishers.

[34] B. F. Sørensen and T. K. Jacobsen, "Determination of cohesive laws by the J integral approach," *Engineering Fracture Mechanics*, vol. 70, pp. 1841–1858, Sept. 2003.

[35] G. Catalanotti, P. Camanho, J. Xavier, C. Dávila, and A. Marques, "Measurement of resistance curves in the longitudinal failure of composites using digital image correlation," *Composites Science and Technology*, vol. 70, pp. 1986–1993, Nov. 2010.

[36] G. P. Cherepanov, "Crack propagation in continuous media. USSR," *J. Appl. Math. Mech. Translation*, vol. 31, p. 504, 1967.

[37] B. Shen and G. H. Paulino, "Direct Extraction of Cohesive Fracture Properties from Digital Image Correlation: A Hybrid Inverse Technique," *Experimental Mechanics*, vol. 51, pp. 143–163, Feb. 2011.

[38] C. Sarrado, A. Turon, J. Costa, and J. Renart, "An experimental analysis of the fracture behavior of composite bonded joints in terms of cohesive laws," *Composites Part A: Applied Science and Manufacturing*, vol. 90, pp. 234–242, Nov. 2016.

[39] R. Joki, F. Grytten, B. Hayman, and B. Sørensen, "Determination of a cohesive law for delamination modelling – Accounting for variation in crack opening and stress state across the test specimen width," *Composites Science and Technology*, vol. 128, pp. 49–57, May 2016.

[40] M. Heshmati, R. Haghani, and M. Al-Emrani, "Dependency of cohesive laws of a structural adhesive in Mode-I and Mode-II loading on moisture, freeze-thaw cycling, and their synergy," *Materials & Design*, vol. 122, pp. 433–447, May 2017.

[41] L. Škec, "Identification of parameters of a bi-linear cohesive-zone model using analytical solutions for mode-I delamination," *Engineering Fracture Mechanics*, vol. 214, pp. 558–577, June 2019.

[42] S. Abdel Monsef, A. Ortega, A. Turon, P. Maimí, and J. Renart, "An efficient method to extract a mode I cohesive law for bonded joints using the double cantilever beam test," *Composites Part B: Engineering*, vol. 178, p. 107424, Dec. 2019.

[43] X. Huo, Q. Luo, Q. Li, G. Zheng, and G. Sun, "On characterization of cohesive zone model (CZM) based upon digital image correlation (DIC) method," *International Journal of Mechanical Sciences*, vol. 215, p. 106921, Feb. 2022.

[44] R. D. Adams, R. W. Atkins, J. A. Harris, and A. J. Kinloch, "Stress Analysis and Failure Properties of Carbon-Fibre-Reinforced-Plastic/Steel Double-Lap Joints," *The Journal of Adhesion*, vol. 20, pp. 29–53, July 1986.

[45] L. Lilleheden, "Mechanical properties of adhesives in situ and in bulk," *International Journal of Adhesion and Adhesives*, vol. 14, pp. 31–37, Jan. 1994.

[46] O. C. Zienkiewicz and R. L. Taylor, *Finite Element Method: Volume 1, Fifth Edition*. Oxford: Butterworth-Heinemann, 5th edition ed., Sept. 2000.

[47] O. C. Zienkiewicz and R. L. Taylor, *The finite element method: solid mechanics*, vol. 2. Butterworth-heinemann, 2000.

[48] D. Ribarić, *Higher-order linked interpolation in moderately thick plate and facet shell finite elements*. PhD Thesis, PhD thesis. Civil Engineering Faculty of Rijeka University, Rijeka, Croatia, 2012.

[49] G. Alfano, "On the influence of the shape of the interface law on the application of cohesive-zone models," *Composites Science and Technology*, vol. 66, pp. 723–730, May 2006.

[50] A. Needleman, "An analysis of tensile decohesion along an interface," *Journal of the Mechanics and Physics of Solids*, vol. 38, pp. 289–324, Jan. 1990.

[51] J. H. Rose, J. Ferrante, and J. R. Smith, "Universal Binding Energy Curves for Metals and Bimetallic Interfaces," *Physical Review Letters*, vol. 47, pp. 675–678, Aug. 1981.

[52] E. D. Reedy, F. J. Mello, and T. R. Guess, "Modeling the Initiation and Growth of Delaminations in Composite Structures," *Journal of Composite Materials*, vol. 31, pp. 812–831, Apr. 1997.

[53] C. Dávila, P. Camanho, and A. Turon, "Effective Simulation of Delamination in Aeronautical Structures Using Shells and Cohesive Elements," *Journal of Aircraft*, vol. 45, Mar. 2008.

[54] R. Russo and B. Chen, "Overcoming the cohesive zone limit in composites delamination: modeling with slender structural elements and higher-order adaptive integration," *International Journal for Numerical Methods in Engineering*, vol. 121, no. 24, pp. 5511–5545, 2020. Publisher: Wiley Online Library.

[55] A. Turon, C. Dávila, P. Camanho, and J. Costa, "An engineering solution for mesh size effects in the simulation of delamination using cohesive zone models," *Engineering Fracture Mechanics*, vol. 74, pp. 1665–1682, July 2007.

[56] P. Robinson, T. Besant, and D. Hitchings, "Delamination growth prediction using a finite element approach," in *European Structural Integrity Society* (J. G. Williams and A. Pavan, eds.), vol. 27 of *Fracture of Polymers, Composites and Adhesives*, pp. 135–147, Elsevier, Jan. 2000.

[57] A. J. Kinloch and S. J. Shaw, "The Fracture Resistance of a Toughened Epoxy Adhesive," *The Journal of Adhesion*, vol. 12, pp. 59–77, May 1981.

[58] T. Pardoen, T. Ferracin, C. M. Landis, and F. Delannay, "Constraint effects in adhesive joint fracture," *Journal of the Mechanics and Physics of Solids*, vol. 53, pp. 1951–1983, Sept. 2005.

[59] R. Campilho, D. Moura, M. Banea, and L. Da Silva, "Adherend thickness effect on the tensile fracture toughness of a structural adhesive using an optical data acquisition method," *International Journal of Adhesion and Adhesives*, vol. 53, pp. 15–22, Sept. 2014.

[60] M. Janssen, J. Zuidema, and R. Wanhill, *Fracture mechanics: fundamentals and applications*. CRC Press, 2004.

[61] M. Gupta, R. Alderliesten, and R. Benedictus, "A review of T-stress and its effects in fracture mechanics," *Engineering Fracture Mechanics*, vol. 134, pp. 218–241, Jan. 2015.

[62] M. Imanaka, X. Liu, and M. Kimoto, "Comparison of fracture behavior between acrylic and epoxy adhesives," *International Journal of Adhesion and Adhesives*, vol. 75, pp. 31–39, June 2017.

[63] B. Davidson and R. Schapery, "Effect of Finite Width on Deflection and Energy Release Rate of an Orthotropic Double Cantilever Specimen," *Journal of Composite Materials*, vol. 22, pp. 640–656, July 1988.

[64] J. Jumel, M. K. Budzik, and M. E. Shanahan, "Beam on elastic foundation with anticlastic curvature: Application to analysis of mode I fracture tests," *Engineering Fracture Mechanics*, vol. 78, pp. 3253–3269, Dec. 2011.

[65] B. D. Davidson, L. Yu, and H. Hu, "Determination of energy release rate and mode mix in three-dimensional layered structures using plate theory," *International Journal of Fracture*, vol. 105, pp. 81–105, 2000. Publisher: Springer.

[66] M. Budzik, J. Jumel, and M. Shanahan, "On the crack front curvature in bonded joints," *Theoretical and Applied Fracture Mechanics*, vol. 59, pp. 8–20, June 2012.

[67] O. Hesebeck, "Consideration of the restriction of lateral contraction in the elastic behaviour of cohesive zone models," *International Journal of Adhesion and Adhesives*, vol. 62, pp. 165–171, Oct. 2015.

[68] H.-C. Tsai, "Compression analysis of rectangular elastic layers bonded between rigid plates," *International Journal of Solids and Structures*, vol. 42, pp. 3395–3410, June 2005.

[69] M. Cabello, J. Zurbitu, J. Renart, A. Turon, and F. Martínez, "A general analytical model based on elastic foundation beam theory for adhesively bonded DCB joints either with flexible or rigid adhesives," *International Journal of Solids and Structures*, vol. 94-95, pp. 21–34, Sept. 2016.

[70] S. Krenk, "Energy release rate of symmetric adhesive joints," *Engineering Fracture Mechanics*, vol. 43, pp. 549–559, Nov. 1992.

[71] J. Manterola, M. Cabello, J. Zurbitu, J. Renart, A. Turon, J. Jumel, and I. Urresti, "Effect of the width-to-thickness ratio on the mode I fracture toughness of flexible bonded joints," *Engineering Fracture Mechanics*, vol. 218, p. 106584, Sept. 2019.

[72] A. A. Griffith, "The phenomena of rupture and flow in solids (Philosophical transactions/Royal Society of London ser. A, v. 221)," in *Royal Soc*, 1920.

[73] C. E. Inglis, "Stresses in a plate due to the presence of cracks and sharp corners," *Trans Inst Naval Archit*, vol. 55, pp. 219–241, 1913.

[74] G. R. Irwin, "Onset of fast crack propagation in high strength steel and aluminum alloys," 1956. Publisher: Naval Research Laboratory Washington, DC, USA.

[75] G. R. Irwin, "Plastic zone near a crack and fracture toughness," 1961.

[76] G. R. Irwin and J. A. Kies, "Critical energy rate analysis of fracture strength," *Welding Journal*, vol. 31, no. 2, pp. 95–100, 1952.

[77] J. M. Krafft, A. M. Sullivan, and R. W. Boyle, "Effect of dimensions on fast fracture instability of notched sheets," in *Proceedings of the crack propagation symposium*, vol. 1, pp. 8–26, sn, 1961.

[78] J. Williams, "End corrections for orthotropic DCB specimens," *Composites Science and Technology*, vol. 35, pp. 367–376, Jan. 1989.

[79] I. Hlača, L. Škec, D. Ribarić, and M. Grbac, "Investigation of the influence of the loading arrangement on the measured mode-I fracture resistance," *Journal of Adhesion Science and Technology*, vol. 38, pp. 397–424, Feb. 2024. Publisher: Taylor & Francis _eprint: https://doi.org/10.1080/01694243.2023.2230654.

[80] B. Blackman, A. Kinloch, M. Paraschi, and W. Teo, "Measuring the mode I adhesive fracture energy, GIC, of structural adhesive joints: the results of an international round-robin," *International Journal of Adhesion and Adhesives*, vol. 23, pp. 293–305, Jan. 2003.

[81] R. Lopes Fernandes, S. Teixeira De Freitas, M. K. Budzik, J. A. Poulis, and R. Benedictus, "From thin to extra-thick adhesive layer thicknesses: Fracture of bonded joints under mode I loading conditions," *Engineering Fracture Mechanics*, vol. 218, p. 106607, Sept. 2019.

[82] E. Jones, M. Iadicola, R. Bigger, B. Blaysat, C. Boo, M. Grewer, J. Hu, A. Jones, M. Klein, K. Raghavan, P. Reu, T. Schmidt, T. Siebert, M. Simenson, D. Turner, A. Vieira, and T. Weikert, "A Good Practices Guide for Digital Image Correlation," tech. rep., International Digital Image Correlation Society, Oct. 2018. Edition: 1.

[83] H. Schreier, J.-J. Orteu, and M. A. Sutton, *Image Correlation for Shape, Motion and Deformation Measurements: Basic Concepts,Theory and Applications*. Boston, MA: Springer US, 2009.

[84] S. H. Tung and M. H. Shih, "Precision verification of a simplified three-dimensional DIC method," *Optics and Lasers in Engineering*, vol. 49, pp. 937–945, July 2011.

[85] L. Škec, G. Alfano, and G. Jelenić, "Complete analytical solutions for double cantilever beam specimens with bi-linear quasi-brittle and brittle interfaces," *International Journal of Fracture*, vol. 215, pp. 1–37, Jan. 2019.

[86] L. Škec and G. Alfano, "Experimental and numerical study of rate-dependent mode-I failure of a structural adhesive," *The Journal of Adhesion*, vol. 99, pp. 1323–1355, June 2023.

[87] J. Viña, A. Argüelles, A. López, V. Mollón, and J. Bonhomme, "Influence of the Loading System on Mode I Delamination Results in Carbon-Epoxy Composites," *Experimental Techniques*, vol. 38, pp. 53–58, Jan. 2014.

[88] M. Aalami and T. Chakherlou, "Investigating the effects of loading system on the fracture behavior of DCB specimens considering T -stress," *Proceedings of the Institution of Mechanical Engineers, Part L: Journal of Materials: Design and Applications*, vol. 235, pp. 2654–2665, Dec. 2021.

[89] M. R. Gude, S. G. Prolongo, and A. Ureña, "Toughening effect of carbon nanotubes and carbon nanofibres in epoxy adhesives for joining carbon fibre laminates," *International Journal of Adhesion and Adhesives*, vol. 62, pp. 139–145, Oct. 2015.

[90] S. R. Kalidindi, A. Abusafieh, and E. El-Danaf, "Accurate characterization of machine compliance for simple compression testing," *Experimental Mechanics*, vol. 37, pp. 210–215, June 1997.

[91] A. Biel and U. Stigh, "An analysis of the evaluation of the fracture energy using the DCB-specimen," *Archives of Mechanics*, vol. 59, no. 4-5, pp. 311–327, 2007.

[92] S. Zhang, R. Panat, and K. J. Hsia, "Influence of surface morphology on the adhesion strength of epoxy–aluminum interfaces," *Journal of Adhesion Science and Technology*, vol. 17, pp. 1685–1711, Jan. 2003.

[93] K. Shahin and F. Taheri, "Fracture Behaviour of Adhesively Bonded Joints in Sandwich Composite Beams," *Journal of Adhesion Science and Technology*, vol. 23, pp. 1531–1546, Jan. 2009.

[94] D. M. Gleich, M. J. L. Van Tooren, and A. Beukers, "Analysis and evaluation of bondline thickness effects on failure load in adhesively bonded structures," *Journal of Adhesion Science and Technology*, vol. 15, pp. 1091–1101, Jan. 2001.

[95] J. P. R. Monteiro, R. D. S. G. Campilho, E. A. S. Marques, and L. F. M. Da Silva, "Experimental estimation of the mechanical and fracture properties of a new epoxy adhesive," *Applied Adhesion Science*, vol. 3, p. 25, Dec. 2015.

[96] A. Savitzky and M. J. E. Golay, "Smoothing and Differentiation of Data by Simplified Least Squares Procedures.," *Analytical Chemistry*, vol. 36, pp. 1627–1639, July 1964.

[97] J. Reiner, J. P. Torres, and M. Veidt, "A novel top surface analysis method for mode I interface characterisation using digital image correlation," *Engineering Fracture Mechanics*, vol. 173, pp. 107–117, 2017.

[98] K. S. Arun, T. S. Huang, and S. D. Blostein, "Least-Squares Fitting of Two 3-D Point Sets," *IEEE Transactions on Pattern Analysis and Machine Intelligence*, vol. PAMI-9, pp. 698–700, Sept. 1987.

[99] E. Standards, "BS EN 6033:2015 Aerospace series. Carbon fibre reinforced plastics. Test method. Determination of interlaminar fracture toughness energy. Mode I. GIC."

[100] M. M. Shokrieh, M. Heidari-Rarani, and S. Rahimi, "Influence of curved delamination front on toughness of multidirectional DCB specimens," *Composite Structures*, vol. 94, no. 4, pp. 1359–1365, 2012.

[101] M. J. Laffan, S. T. Pinho, P. Robinson, and L. Iannucci, "Measurement of the in situ ply fracture toughness associated with mode I fibre tensile failure in FRP. Part I: Data reduction," *Composites science and technology*, vol. 70, no. 4, pp. 606–613, 2010.

[102] Q. Yang and B. Cox, "Cohesive models for damage evolution in laminated composites," *International Journal of Fracture*, vol. 133, pp. 107–137, May 2005.

[103] R. Taylor, "{FEAP} - Finite Element Analysis Program," 2014.

[104] M. Ranjbar, L. Škec, G. Jelenić, and D. Ribarić, "Mixed-mode delamination of layered structures modeled as Timoshenko beams with linked interpolation," *International Journal for Numerical Methods in Engineering*, vol. 124, no. 8, pp. 1773–1797, 2023.

[105] D. Ribarić, "Problem-dependent cubic linked interpolation for Mindlin plate four-node quadrilateral finite elements," *Structural engineering and mechanics: An international journal*, vol. 59, no. 6, pp. 1071–1094, 2016.

[106] P. W. Harper and S. R. Hallett, "Cohesive zone length in numerical simulations of composite delamination," *Engineering Fracture Mechanics*, vol. 75, pp. 4774–4792, Nov. 2008.

[107] L. M. Vogl, P. Schweizer, G. Richter, and E. Spiecker, "Effect of size and shape on the elastic modulus of metal nanowires," *MRS Advances*, vol. 6, pp. 665–673, Sept. 2021.

[108] G. Ji, Z. Ouyang, G. Li, S. Ibekwe, and S.-S. Pang, "Effects of adhesive thickness on global and local Mode-I interfacial fracture of bonded joints," *International Journal of Solids and Structures*, vol. 47, pp. 2445–2458, Sept. 2010.

[109] F. Auricchio and R. L. Taylor, "A shear deformable plate element with an exact thin limit," *Computer Methods in Applied Mechanics and Engineering*, vol. 118, pp. 393–412, Oct. 1994.

[110] I. Hlača, D. Ribarić, L. Škec, and M. Ranjbar Zefreh, "Modelling delamination of a DCB test by using non-linear truss interface elements and plate elements with assumed shear strain," in *Proceedings of the YIC 2021 - VI ECCOMAS Young Investigators Conference*, pp. 16–23, Editorial Universitat Politècnica de València, May 2022.

[111] P. Davies, L. Sohier, J. Y. Cognard, A. Bourmaud, D. Choqueuse, E. Rinnert, and R. Créac'hcadec, "Influence of adhesive bond line thickness on joint strength," *International Journal of Adhesion and Adhesives*, vol. 29, pp. 724–736, Oct. 2009.

[112] X. Han, Y. Jin, L. F. M. da Silva, M. Costa, and C. Wu, "On the effect of adhesive thickness on mode I fracture energy - an experimental and modelling study using a trapezoidal cohesive zone model," *The Journal of Adhesion*, vol. 96, pp. 490–514, Apr. 2020.

[113] M. D. Banea, L. F. M. da Silva, and R. D. S. G. Campilho, "The Effect of Adhesive Thickness on the Mechanical Behavior of a Structural Polyurethane Adhesive," *The Journal of Adhesion*, vol. 91, pp. 331–346, Jan. 2015.

[114] Y. J. Liu and H. R. Riggs, "The MIN-N family of pure-displacement, triangular, Mindlin plate elements," *Structural engineering and mechanics: An international journal*, vol. 19, no. 3, pp. 297–320, 2005.

[115] C. M. Wang, J. N. Reddy, and K. H. Lee, *Shear deformable beams and plates: Relationships with classical solutions.* Elsevier, 2000.

List of Figures

List of Tables